

THE ELECTRONIC STRUCTURE AND FIELD EFFECTS OF AN ORGANIC-  
BASED ROOM TEMPERATURE MAGNETIC SEMICONDUCTOR

DISSERTATION

Presented in Partial Fulfillment of the Requirements for  
the Degree Doctor of Philosophy in the Graduate  
School of The Ohio State University

By

Derek M. Lincoln, B.S., M.S.

\*\*\*\*\*

The Ohio State University  
2007

Dissertation Committee:

Prof. Arthur J. Epstein, Advisor

Prof. Anne B. McCoy

Prof. Bern Kohler

Approved by

---

Advisor  
Graduate Program in Chemistry

Report Documentation Page				Form Approved OMB No. 0704-0188	
Public reporting burden for the collection of information is estimated to average 1 hour per response, including the time for reviewing instructions, searching existing data sources, gathering and maintaining the data needed, and completing and reviewing the collection of information. Send comments regarding this burden estimate or any other aspect of this collection of information, including suggestions for reducing this burden, to Washington Headquarters Services, Directorate for Information Operations and Reports, 1215 Jefferson Davis Highway, Suite 1204, Arlington VA 22202-4302. Respondents should be aware that notwithstanding any other provision of law, no person shall be subject to a penalty for failing to comply with a collection of information if it does not display a currently valid OMB control number.					
1. REPORT DATE <b>01 NOV 2007</b>		2. REPORT TYPE <b>N/A</b>		3. DATES COVERED <b>-</b>	
4. TITLE AND SUBTITLE <b>The Electronic Structure And Field Effects Of An Organic-Based Room Temperature Magnetic Semiconductor</b>				5a. CONTRACT NUMBER	
				5b. GRANT NUMBER	
				5c. PROGRAM ELEMENT NUMBER	
6. AUTHOR(S)				5d. PROJECT NUMBER	
				5e. TASK NUMBER	
				5f. WORK UNIT NUMBER	
7. PERFORMING ORGANIZATION NAME(S) AND ADDRESS(ES) <b>The Ohio State University</b>				8. PERFORMING ORGANIZATION REPORT NUMBER	
9. SPONSORING/MONITORING AGENCY NAME(S) AND ADDRESS(ES) <b>AFIT/ENEL Wright-Patterson AFB OH 45433-7765</b>				10. SPONSOR/MONITOR'S ACRONYM(S)	
				11. SPONSOR/MONITOR'S REPORT NUMBER(S) <b>C109-0001</b>	
12. DISTRIBUTION/AVAILABILITY STATEMENT <b>Approved for public release, distribution unlimited</b>					
13. SUPPLEMENTARY NOTES					
14. ABSTRACT					
15. SUBJECT TERMS					
16. SECURITY CLASSIFICATION OF:			17. LIMITATION OF ABSTRACT <b>UU</b>	18. NUMBER OF PAGES <b>148</b>	19a. NAME OF RESPONSIBLE PERSON
a. REPORT <b>unclassified</b>	b. ABSTRACT <b>unclassified</b>	c. THIS PAGE <b>unclassified</b>			

## ABSTRACT

The future of spin-electronics or “spintronics” lies in the development of viable magnetic semiconductors that can effectively operate at room temperature. Vanadium tetracyanoethylene ( $\text{V}[\text{TCNE}]_{\sim 2}$ ) is a magnetic semiconductor with an ordering temperature well above that of room temperature. Its highly disordered structure has hampered a comprehensive description of the interactions between the V and TCNE sublattices that give rise to its magnetic and electrical properties. We report the results of high-resolution x-ray absorption (XAS) and magnetic circular dichroism (MCD) studies probing the electronic structure of  $\text{V}[\text{TCNE}]_{\sim 2}$  in an effort to elucidate the nature of these interactions. Included in this study are the first reports of gas phase neutral TCNE XAS spectra as well as the first reports of MCD spectra of the carbon and nitrogen absorption edges for the  $\text{V}[\text{TCNE}]_{\sim 2}$  system. The vanadium spectrum reveals a spin split  $L_3$  and  $L_2$  spectrum that is qualitatively modeled for V(II) using crystal field multiplet (CFM) theory calculations except for a region of excess intensity on the high energy side of both the  $L_3$  and  $L_2$  absorption edges. We speculate that the origin of this excess intensity is vanadium present in valence states higher than V(II) and antibonding states from the hybridization of the V centers and TCNE. Despite the localized nature of the x-ray absorption process the C and N spectra of the TCNE suggest that we are probing molecular final states of TCNE from different sites rather than atomically isolated states. In

addition, the carbon and nitrogen absorption spectra reveal that this molecular orbital structure remains largely intact in going from the gas phase to the condensed phase in  $V[TCNE]_{\sim 2}$ . The value in the high-resolution experimental data is exposed as new features are detected unveiling the effects of magnetic exchange in the system leading to spin splitting of the singly occupied molecular orbital of  $[TCNE]^{\bullet-}$  as revealed by the carbon and nitrogen XAS and MCD spectra. Remarkable alignment of low photon energy features in the vanadium, carbon, and nitrogen spectra reveal a strong hybridized structure between the valence molecular orbitals of TCNE and the vanadium  $3d$  orbitals. Associated MCD spectra elucidate the polarization associated with the particular XAS features and we speculate on the mechanism of magnetic interaction between the V and TCNE sub-lattices. We also report for the first time the electric field effects of  $V[TCNE]_{\sim 2}$ . We construct field-effect devices and demonstrate the field effect and measure the current-voltage characteristics of these devices under varying applied gate voltages.

The views expressed in this article are those of the author and do not reflect the official policy or position of the United States Air Force, Department of Defense, or the U.S. Government.

Dedicated to Larry, Steve, Sophie, Donkey, Boudreaux, Cotton,  
and of course, Holly.

## ACKNOWLEDGMENTS

I first need to thank my advisor, Dr. Arthur Epstein. He accepted my program constraints when no one else would and kept me motivated and on track. His seemingly endless knowledge of physics and chemistry made for smooth ride over a bumpy road and helped me learn things I never thought possible. Thanks.

I also need to thank my mentor and friend, Dr. Ruthie Shima Edelstein. She taught me just about every skill I needed in the lab and provided insightful discussions not only about science but life in general. I've missed having you around. Dr. Chuanjun Xia, probably one of the most talented chemists I have ever met, you were an inspiration and a great help to my learning experience. And what is a graduate school experience without your fellow grad students helping you along the way: June Hyoung Park, Jung-Woo Yoo, Nan-Rong Chiou, Deniz Duman, Timi Adetunji, and Jesse Martin. Thanks also to Drs. Raju Nandyala and Vladimir Prigodin for help with the hard stuff. Chia-Yi Chen, the best lab partner ever. Dr. Jeremy Bergeson: I probably learned more from you than any book, any article, or Wikipedia. Hands down the most talented and helpful young scientist I know.

Erin Sharp, Sara Ray, and Nicole Trease – I couldn't have been luckier with a better trio of absolutely competent TA's helping me through my coursework. Special thanks to Mike Mrozik and Sam Horvath for breaking up the monotony.

What is any education or job without the people that keep the wheels of the world turning? Thanks to Jenny, Tom, Jen, Kent, John, John, Pete, and Tim for always having solutions to all my problems and for always being willing to help me out.

I'd like to offer special thanks Dr. Jeff Kortright. I certainly wouldn't have reached this point without you. I learned more from you than I ever thought possible. I enjoyed our numerous discussions and am very grateful for your hard work, willingness and patience in putting this puzzle together.

My parents, thanks for your encouragement and support. You never lost faith and always believed in me.

I dedicate these years and this work especially to my wife as you have had to work just as hard as I have. I couldn't have done it without you. I love you!

## VITA

1974. .... Born – Denver, CO
1996. .... B.S. Chemistry,  
United States Air Force Academy,  
Colorado Springs, CO
1998. .... M.S. Materials Science and Engineering,  
University of Florida,  
Gainesville, FL
- 1998-2001. .... Materials Scientist and Advanced Rocket Propulsion  
Materials Program Manager,  
Wright-Patterson AFB,  
Wright-Patterson AFB, OH
- 2001-2004. .... Instructor/Assistant Professor of Chemistry  
United States Air Force Academy  
Colorado Springs, CO
- 2004-Present. .... Graduate Student,  
The Ohio State University,  
Columbus, OH

## PUBLICATIONS

### Research Publications

J.-W. Yoo, R. Shima Edelstein, D.M. Lincoln, N.P. Raju, C.Xia, K.I. Pokhodnya, J.S. Miller, and A.J. Epstein *Multiple Photonic Responses in Films of Organic-Based Magnetic Semiconductor  $V[TCNE]_x$ ,  $x \sim 2$* , Phys. Rev. Lett. **97**, 247205 (2006)

V.N. Prigodin, J.D. Bergeson, D.M. Lincoln and A.J. Epstein *Anomalous Room Temperature Magnetoresistance in Organic Semiconductors*, Synth. Met. **156**, 757 (2006)



## FIELDS OF STUDY

Major Field: Chemistry

Studies in:

Organic-based magnetic materials  
Organic field-effect transistors

# TABLE OF CONTENTS

	<b>Page</b>
Abstract.....	ii
Dedication.....	iv
Acknowledgments.....	v
Vita.....	vii
List of Tables .....	xi
List of Figures .....	xii
1. Introduction .....	1
2. Background.....	5
2.1 Organic-Based Magnets and Magnetism.....	5
2.2.1 The Organic-Based Magnetic Semiconductor V[TCNE] <sub>2</sub> .....	13
2.3 X-ray Absorption Spectroscopy (XAS) & Magnetic Circular Dichroism (MCD). ..	20
2.4 Atomic, Crystal Field, and Charge Transfer Multiplet Theories.....	25
2.5 Organic Field-Effect Transistors (OFET).....	34
3. Experimental.....	41
3.1 Materials .....	41
3.2 Thin Film Deposition via Chemical Vapor Deposition.....	43
3.3 X-ray Absorption Spectroscopy Measurements .....	45
3.4 Organic Field Effect Transistor Fabrication and Testing .....	48

4. The Electronic Structure of V[TCNE] <sub>~2</sub> .....	57
4.1 XAS and MCD Results .....	57
4.1.1 The Vanadium L-edge .....	57
4.1.1.1 Crystal Field Multiplet Calculations.....	61
4.1.1.2 Charge Transfer Multiplet Calculations.....	67
4.1.1.3 Origin of the Excess Intensity in the Experimental XAS Spectrum.....	72
4.1.2 The Carbon and Nitrogen K-Edges.....	83
4.1.2.1 Gas Phase TCNE <sup>0</sup> .....	84
4.1.2.2 V[TCNE] <sub>~2</sub> Films .....	87
4.2 Putting it All Together.....	94
5. Field Effects in V[TCNE] <sub>~2</sub> .....	103
5.1 Field Effects in V[TCNE] <sub>~2</sub> .....	103
6. Conclusions .....	111
6.1 Summary and Conclusions .....	111
6.1.1 Electronic Structure of V[TCNE] <sub>~2</sub> .....	111
6.1.2 Field Effects in V[TCNE] <sub>~2</sub> .....	113
6.1.3 Outlook and Further Research .....	113
Appendix A.....	116
Bibliography .....	125

## LIST OF TABLES

<b>Table</b>	<b>Page</b>
5.1 The estimated percent change in current for given applied gate voltages.....	106
A.1 Assignments for the various combinations of $m_l$ and $m_s$ . The first column gives an arbitrary assignment number for keeping track of the different $m_l$ and $m_s$ only and has no other meaning. ....	118
A.2 The 120 different possible combinations for three electrons distributed in 10 spin orbitals. ....	119
A.3 The possible $M_L - M_S$ combinations possible for the three d electrons. The third column lists the total number of combinations that yield the given $M_L - M_S$ combination. ....	120
A.4 A convenient way to put the results of Table A.3 in order and to keep track of the different combinations of $M_L$ and $M_S$ for the purpose of determining the term symbols. ....	121
A.5 Table A.4 after removing the 22 microstates associated with $M_L = 5$ leaving the largest $M_L = 4$ . ....	122

## LIST OF FIGURES

Figure	Page
1.1 Publications per year on the subject of organic magnetic materials since 1991. Last year saw a nearly six-fold increase in the number of publications over 1991 – the year of the introduction of $V[TCNE]_{-2}$ . ....	2
2.1 Various electron spin interaction in magnetic materials. Top left panel – paramagnetic materials have electrons spins that do not interact and continually change direction and would have different orientations at time $t_0$ and $t_1$ and thus do not possess a bulk magnetic moment. Top right panel – ferromagnetic materials have electron spins that align parallel to each other which gives rise to a net magnetic moment. Bottom left panel – antiferromagnetic materials have electron spins that align antiparallel to each other so that no net bulk magnetic moment is realized. Bottom right panel – ferrimagnetic materials have unequal numbers of electron spins that are aligned antiparallel to each other so that a net magnetic moment is present.....	7
2.2 The unpaired electron spin in a carbon atom polarizing the electrons in the orthogonal bond adjacent to it as described by a CI admixture model.....	10
2.3 Proposed high-spin carbene sheet.....	10
2.4 Stabilization of adjacent $A^+D^-$ units in (a) antiferromagnetic or (b) ferromagnetic coupling via configuration interaction .....	12
2.5 The first wholly organic ferromagnet p-nitrophenyl nitronyl nitroxide with an ordering temperature of 0.6 K. ....	13
2.6 Magnetization as a function of temperature for vanadium tetracyanoethylene prepared via solvent methods in the form of $V[TCNE]_{-2} \cdot y(\text{solvent})$ .....	15
2.7 Magnetization of CVD films of $V[TCNE]_{-2}$ . The nearly constant magnetization as a function of temperature indicates an ordered film.....	15

2.8	Magnetoresistance measurement results for V[TCNE] <sub>~2</sub> ( $T_c > 300\text{K}$ ) recorded at 260 K (top) and 300 K (bottom). Below $T_c$ the magnetoresistance (MR) is linear with temperature but above $T_c$ the MR displays a quadratic behavior.....	17
2.9	1-D spatial distribution and relative energy alignment of the $V^{2+}$ 3 <i>d</i> and [TCNE] <sup>•-</sup> $\pi^*$ levels in V[TCNE] <sub>~2</sub> . Each [TCNE] <sup>•-</sup> $\pi^*$ orbital can accommodate two electrons with antiparallel spins, but the addition of an electron to the singly occupied molecular orbital carries with it an additional Coulomb repulsion energy, $U_c$ . The $\pi^* + U_c$ , a separate sub-band as viewed in this model, level is involved in hopping charge transport along with the V 3 <i>d</i> level. ....	18
2.10	Schematic representation of the x-ray absorption process. X-rays in the energy range of ~100-1000 eV in resonance with core level electrons are absorbed exciting the electrons to unoccupied orbitals above the Fermi energy level. ....	21
2.11	Top – A schematic representation of the MCD process for, e.g., L-edge absorption. Circularly polarized x-ray radiation excites electrons whose spin polarization depends on the edge from which it is excited, $L_2$ or $L_3$ . These spin polarized electrons are then injected into unoccupied 3 <i>d</i> orbitals. In a magnetic material there exists an unbalance in the number of available empty spin up and spin down states causing the absorption of the polarized radiation to be different. Bottom – an example of the dipole allowed transitions for a typical transition metal, given as $2p^6 3d^N \rightarrow 2p^5 3d^{N+1}$ , where $\Delta M$ indicates the polarization of the incident photons. ....	24
2.12	Typical OFET architectures: (a) is known as a bottom-contact, bottom-gate architecture because the source/drain contacts and the gate dielectric are both between the semiconducting layer and the substrate (this architecture is used in this work); (b) is then top-contact, bottom gate; and (c) is bottom-contact, top gate. Each color represents the same layer in all the figures.....	35
2.13	Operating regimes of field-effect transistors: (a) linear regime, (b) beginning of saturation regime, and (c) saturation regime.....	37
2.14	Typical current-voltage characteristics of OFETs showing the linear and saturation regimes and the effect of increasing the gate voltage. The approximate location of the pinch-off point is also indicated. ....	39
3.1	The tetracyanoethylene precursor used in depositing films of V[TCNE] <sub>~2</sub> . TCNE is a fine white powder in its pure form but reaction with water gives it a distinct off-white to yellow color, which offers a good indicator of the purity of the material. Once purified and stored in a very dry (< 1 ppm H <sub>2</sub> O) atmosphere TCNE will maintain its purity for prolonged periods of time	

(months). Neutral TCNE and singly reduced [TCNE] <sup>•-</sup> have a planar $D_{2h}$ symmetry structure, but the dianion can adopt a twisted $D_{2d}$ structure. ....	42
3.2 Laboratory apparatus for preparing $V(CO)_6$ for use in synthesizing $V[TCNE]_{-2}$ . The $[Et_4N][V(CO)_6]/H_3PO_4$ mixture is heated gently to ~45 °C with stirring. The blue-black product ( $V(CO)_6$ ) collects on the cold finger cooled with a liquid nitrogen/methanol bath. The reaction is carried out under vacuum ( $\sim 10^{-4} - 10^{-5}$ torr). ....	42
3.3 Chemical Vapor Deposition (CVD) apparatus for thin-film deposition of $V[TCNE]_{-2}$ . The TCNE side of the reactor is heated to ~60 °C and the $V(CO)_6$ side is cooled to 10°C in a silicon oil bath. The Ar carrier gas is pulled from the controlled atmosphere glove box in which the synthesis takes place with an environment of < 1 ppm $O_2$ and < 1 ppm $H_2O$ . ....	44
3.4 Silicon nitride membranes and specially designed holder used in the x-ray absorption experiments. $V[TCNE]_{-2}$ films were deposited with the top removed from the holder bottom. Al protecting layers were deposited with the top in place. ....	46
3.5 Typical OFET configuration: top view (left) and side view (right). Each substrate has up to four devices. Typical active channel lengths are 25 to 40 $\mu$ m, with channel widths of 760 $\mu$ m and channel depths of 30 nm. Al gate electrodes are 100 nm thick, gate dielectric thicknesses ranged from 300 – 500 nm, Au contacts are 30 nm thick, and the $V[TCNE]_{-2}$ layers ranged in thickness from 200 – 500 nm. ....	51
3.6 A typical OFET device wired to a PPMS puck. The substrate is outlined in the box. ....	52
3.7 Wiring schematic for testing the $V[TCNE]_{-2}$ field-effect transistors. The Keithley picoammeter triaxial cable shields are grounded through the PPMS cable shield ground. The difference in the line types is not to indicate differences in the wire types used but only to indicate the connectivity of the setup. ....	53
3.8 Example raw $I_{sd}$ versus $V_{sd}$ (top) and $I_{sd}$ versus time (bottom) data. In the bottom plot $V_{sd}$ was held constant at 5 V while the gate voltage was varied from 5 – 40 V at varying intervals which accounts for the observed drop in $I_{sd}$ . ....	54
3.9 The change in source-drain current, $\Delta I_{sd}$ , plotted as a function of time. The gate voltage is applied at different time intervals as indicated. Note the leakage current between the drain and gate electrodes is far less than the observed change in $I_{sd}$ indicating $\Delta I_{sd}$ is due largely to the field-effect. ....	56

4.1	Vanadium $L_3$ and $L_2$ absorption edges. The spectrum was normalized between 0 intensity at the pre-edge and 1 far beyond the absorption edge. The baseline is drawn as shown using two arctan functions (one for each edge – $L_3$ and $L_2$ ) as described in the text. The inset shows an oxidized sample with the O 1s absorption peak labeled. ....	59
4.2	Experimental magnetic circular dichroism (MCD) signal with associated XAS for the vanadium L-edge in $V[TCNE]_{-2}$ . The XAS spectrum has been normalized to between 0 (pre-edge) to 1 (well above absorption edge). The MCD spectra is as recorded with no normalization, background subtraction, or scaling. ....	61
4.3	The crystal field splitting of the five $d$ -orbitals under the influence of an octahedral crystal field. Left – the five degenerate $d$ -orbitals in a spherical field. Right – the five orbitals split in energy due to the interaction with an octahedral field where the interaction is greater with the $e_g$ orbitals, hence the higher energy. Note: the average energy of the orbitals does not change upon application of the crystal field. ....	63
4.4	Calculated vanadium XAS spectra including the $L_3$ and $L_2$ edges from crystal field multiplet theory. The crystal field splitting strength, $10Dq$ , is varied from $-3.0$ eV to $3.0$ eV as shown on the right. In each case the calculations are done with a pure $d^3$ configuration ( $V^{2+}$ ). The $0.0$ eV case corresponds to the pure atomic multiplet case with no applied crystal field but still takes into account the $2p$ - $3d$ core-hole potential and $3d$ - $3d$ electron repulsion interactions. ....	64
4.5	Comparison of the vanadium XAS (top) and MCD (bottom) experimental spectra and calculated spectra from crystal field multiplet (CFM) theory. The energy scales of the calculated spectra were adjusted by $0.45$ eV and the intensity multiplied by a factor of 33 for comparison to the experimental data. The continuum step has been removed from the experimental XAS spectrum as described in the text. The MCD spectrum is plotted as recorded. ....	66
4.6	Comparison of the experimental XAS (top) and MCD (bottom) spectra with that calculated from charge transfer multiplet (CTM) theory. The continuum step has been removed from the experimental spectrum as described in the text. The energy scale of the calculated spectrum was adjusted by $-1.8$ eV and intensity scaled by 28 for comparison to the experimental data. ....	70
4.7	The experimental V L-edge spectrum with its associated CFM calculated spectrum and its three resolved symmetry states contributing intensity. $A_1$ , $A_2$ , and $T_1$ are symmetry representations in $O_h$ . ....	73



4.8	Crystal field multiplet calculations in $D_{4h}$ symmetry compared to $O_h$ symmetry and experiment. The three values in parentheses are the three crystal field operators in $D_{4h}$ 10Dq, Ds, and Dt. ....	74
4.9	Charge transfer multiplet calculated spectra calculated using the three ground state configurations $3d^3$ , $3d^4L$ and $3d^5L^2$ (spectrum labeled $V^{2+}$ ) and the three ground state configurations $3d^2$ , $3d^3L$ and $3d^4L^2$ (spectrum labeled $V^{3+}$ ). The experimental spectrum is normalized between 0 (pre-edge) and 1 (well above the absorption edge). The intensities of the calculated charge transfer spectra have been scaled by a factor of 14.3 and the energy scales shifted by -1.5 for comparison to the experimental spectrum. ....	76
4.10	CFM calculated XAS (top panel) and MCD (bottom panel) spectra using the pure $d^2$ , $d^3$ , and $d^4$ configurations. Each calculation was accomplished with a crystal field splitting strength $10Dq = 2.4$ eV. ....	78
4.11	The experimental XAS spectrum fitted with the CFM theory calculated spectrum plus two Gaussian peaks located in the energy region of the excess intensity from the experimental spectrum. ....	79
4.12	Carbon (top) and nitrogen (bottom) K-edge x-ray absorption results. Both spectra are presented as-recorded, i.e. no normalization or background subtractions have been accomplished. ....	85
4.13	Comparison of the $V[TCNE]_{-2}$ condensed films carbon (top) and nitrogen (bottom) K-edge x-ray absorption spectra with the $TCNE^0$ spectra. The $V[TCNE]_{-2}$ spectra have both been normalized to between 0 (pre-edge) and 1 (well above absorption edge). The $TCNE^0$ spectra are as-recorded, i.e. no normalization or background subtractions have been conducted. ....	88
4.14	The LUMO (left) and $LUMO^{+1}$ (right) electronic density contours for TCNE. Spin density calculations for $[TCNE]^{\bullet-}$ indicate the partially occupied orbital (former LUMO) retains much of the general shape and electron density distribution as the LUMO shown here. Figure reprinted with permission. ....	90
4.15	Magnetic circular dichroism (MCD) spectra for carbon (left) and nitrogen (right) collected from $V[TCNE]_{-2}$ condensed phase CVD films. Both spectra have been normalized to between 0 (pre-edge) and 1 (well above absorption edge). ....	93
4.16	Valence band photoemission spectra of condensed phase TCNE, Rb-doped TCNE, and $V[TCNE]_{-2}$ films. Panel A – spectra with incident $h\nu = 21.2$ eV, Panel B – incident $h\nu = 40.8$ eV, and Panel C – low binding energy spectra of $V[TCNE]_{-2}$ recorded at various incident radiation energies. ....	96

4.17	The three absorption edges studied in this work. The energy scales have been adjusted so the lowest two features in each edge are aligned. The nitrogen plot (bottom plot) shows the results of peak fitting the nitrogen spectrum (only the two lowest energy fitting peaks are shown for clarity) indicating the new low energy feature is actually two new features; the energy scale is then adjusted so these two features align with the two lowest energy features in vanadium and carbon.....	97
4.18	Schematic depiction of the proposed spin polarization interaction in V[TCNE] <sub>~2</sub> between the central lobe of the $\pi^*_{C=C}$ orbital, the outer lobe over the N and V atoms. The two central $sp^2$ C atoms both display negative polarizations while the hybridized N and V atoms display a positive polarization. The uncoordinated N atoms display positive polarization. C – gray, N – blue, and V – green.....	102
5.1	The percent change in $I_{sd}$ as a function of the applied gate voltage, $V_g$ . In this case the source-drain voltage, $V_{sd}$ , was held constant at 5V and the gate voltage was returned to 0V between each measurement. ....	105
5.2	IV traces for a typical V[TCNE] <sub>~2</sub> OFET device over a –125V to +125V range with different gate voltages. ....	108

## CHAPTER 1

### INTRODUCTION

In the July 1, 2005 issue of *Science* 125 questions were posed to which we don't currently know the answers but should be solvable within the next 25 years.<sup>1</sup> One of the 125 questions posed deals with the possibility of developing a magnetic semiconductor that operates at room temperature. The answer to that question is it has already been done – in 1991 the first room temperature magnetic semiconductor was introduced,  $V[TCNE]_{0.2}$ .<sup>2</sup> The future of spin-electronics or “spintronics” is in the hands of magnetic semiconductors and the commercial viability relies on magnetic semiconducting materials that operate at room temperature. The spintronics area is based on the ability of devices to control not only the charge conduction not just through the traditional p- or n-type control but also through control of the charge's quantum spin state. Spin-valve devices are a very good example of how the spin state of electrons is manipulated to control charge conduction.<sup>3</sup> The typical magnets used in spin valve devices (Fe, Co, etc.) provide only the order of 50% spin polarization making them effective but relatively inefficient devices; whereas, magnetic semiconductors could potentially provide near total spin polarization leading to far more efficient devices. In addition, magnetic

semiconductors may reduce the need for complex layered devices to get the same effect magnetic semiconductors can provide alone.

If  $V[TCNE]_{-2}$  has existed for well over a decade, why then was this question in a list of things yet unanswered? The answer to that question may lie in the fact that the materials itself poses some very challenging questions that remain partially or altogether unanswered. However, new organic magnetic materials and in depth studies of organic magnetic materials are making their way into the literature, and thus, scientists are learning more and more about what makes them tick (see Fig 1.1).

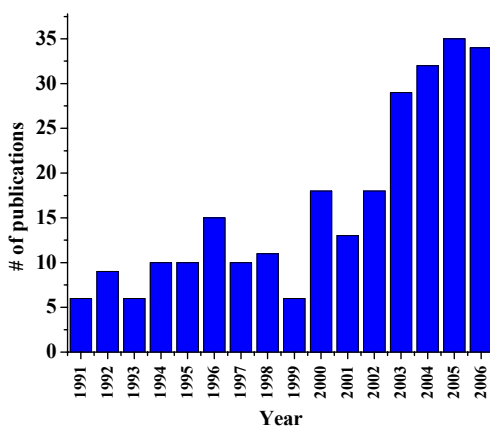


Figure 1.1. Publications per year on the subject of organic magnetic materials since 1991. Last year saw a nearly six-fold increase in the number of publications over 1991 – the year of the introduction of  $V[TCNE]_{-2}$ .<sup>4</sup>

The biggest challenge lies in developing more and better organic magnetic materials with truly tailorable properties. The idea of tailorable properties is not unique to organic magnets but it is a trait commonly cited as an advantage for organic-based materials over their inorganic counterparts. The key lies in fully understanding the mechanism behind

the magnetic interactions in organic-based magnets down to the microscopic interactions between atoms and molecules or atomic and molecular orbitals. This first part of this work is dedicated to furthering the understanding of these interactions in  $V[TCNE]_{-2}$  with an eye to supplying general knowledge of these interactions to those who follow to design next generation organic-based magnetic semiconductor materials.

The second challenge lies in demonstrating the application of these materials in ways that push the envelope of modern electronics rather than offer only a replacement of current technologies with modest increases in performance. The second portion of this work is dedicated to demonstrating for the first time the application of  $V[TCNE]_{-2}$  in an organic field-effect transistor. Organic field-effect transistors (OFET) have themselves been receiving and continue to receive a great deal of attention since the first demonstration of such devices in the mid-1980's.<sup>5</sup> In many ways OFETs are similar to their ubiquitous inorganic silicon-based counterparts and in many ways they are different. It is these differences that offer the possibility of inexpensive, flexible electronic circuits in devices such as radio-frequency identification tags<sup>6</sup> and flexible displays.<sup>7</sup> OFETs based on magnetic semiconductors offer an additional interesting ability in the possibility in being able to control the spin quantum state of the charge carriers. On the other hand, the OFET architecture offers the interesting possibility of electric field controlled magnetism akin to the recently demonstrated photo control of magnetism in  $V[TCNE]_{-2}$ .<sup>8</sup>

This work is organized in the following manner: a general background will be provided on organic magnetism with an introduction and history of  $V[TCNE]_{-2}$  along with a background of the x-ray techniques and theoretical models used in this study in the first part of Chap. 2. Chap. 2 will then continue with an introduction to the fundamentals

of field-effects transistors. Chap. 3 will detail the experimental techniques used in carrying out these studies to include x-ray absorption (XAS) and magnetic circular dichroism (MCD) spectroscopies as well as atomic multiplet theory calculations to model the experimental spectra. Chap. 4 details the results of the XAS and the MCD studies showing possible hybridization between the vanadium and TCNE sub-lattices and indication of spin polarized sub-bands as a mechanism for magnetism in the system. Chap. 5 discusses the results and implications of the studies of the electric field effects on  $V[TCNE]_{\sim 2}$  which reveal unusual n-channel behavior of the material. Chap. 6 will provide concluding remarks and future outlook.

## **CHAPTER 2**

### **BACKGROUND**

#### **2.1 Organic-Based Magnets and Magnetism**

The magnetic phenomena typically associated with the common, everyday inorganic magnetic materials, transition metal and rare earth magnets, can also be applied to organic-based magnetic materials. The major difference is that organic-based magnetic materials carry with them the advantages commonly cited for organic material versus inorganic materials. These advantages range from low density, low temperature processing, and solubility to biocompatibility, transparency, and chemical tailorability. It is this last attribute, chemical tailorability, which has led to a rather rapid development in the wide ranging properties of organic-based magnetic materials to include very high (27 kOe) and very low (few Oe) coercivities as well as high and low remanent and saturation magnetizations.<sup>9</sup>

Classically, Lenz's law dictates that under the application of a magnetic field electrons will change their orbital velocity to oppose the applied field. This opposition of the applied magnetic field leads to a diamagnetic response. Every material has a diamagnetic response, that is, a tendency to oppose an applied magnetic field with an associated orbital magnetic moment aligned opposite to the field. In addition to the

orbital magnetic moment electrons also have an intrinsic angular momentum known as electron spin, which takes on one of two values,  $+\frac{1}{2}$  (spin-up) or  $-\frac{1}{2}$  (spin-down). Electrons then also possess a spin magnetic moment. In purely diamagnetic materials all the electron orbitals are completely full or completely empty which means that all the electrons are paired and there is no net spin magnetic moment as the paired electrons are aligned antiparallel to each other via the Pauli exclusion principle. Materials with unpaired electrons, such as radicals, can possess an intrinsic magnetic moment. The application of a magnetic field tends to align the magnetic moments of these unpaired electrons parallel to the field thus attracting the material into the applied field. This is known as the paramagnetic response of a material. In addition to a response to an applied magnetic field, unpaired electron spins interact with each other within the material which leads to the different spin arrangements as shown in Fig. 2.1.

At this point it is prudent to point out that mere ferromagnetic, antiferromagnetic or ferrimagnetic coupling of spins is not enough for materials to exhibit magnetic behavior as magnetism is not simply a quantum mechanical property but rather a cooperative bulk solid-state phenomenon. To put it simply it takes not just one pair of electrons coupling magnetically but many, many pairs of electrons coupling magnetically and cooperatively throughout the bulk of the material in order for a material to behave magnetically. Henceforth, the term “magnetic coupling” will refer to adjacent spins aligning ferro-, antiferro- or ferrimagnetically and the term “magnetic ordering” will refer to the cooperative alignment of many coupled pairs of spins that gives rise to bulk magnetic behavior.



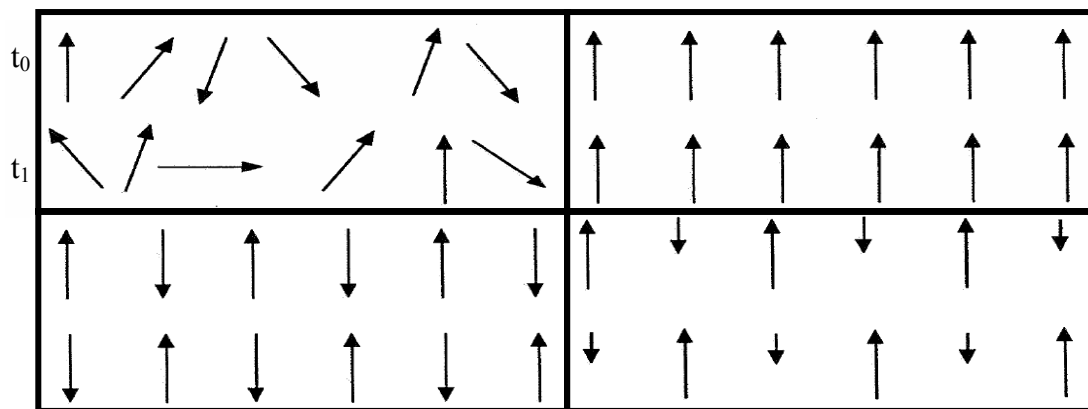


Figure 2.1. Various electron spin interaction in magnetic materials. Top left panel – paramagnetic materials have electrons spins that do not interact and continually change direction and would have different orientations at time  $t_0$  and  $t_1$  and thus do not possess a bulk magnetic moment. Top right panel – ferromagnetic materials have electron spins that align parallel to each other which gives rise to a net magnetic moment. Bottom left panel – antiferromagnetic materials have electron spins that align antiparallel to each other so that no net bulk magnetic moment is realized. Bottom right panel – ferrimagnetic materials have unequal numbers of electron spins that are aligned antiparallel to each other so that a net magnetic moment is present.

Magnetism in conventional magnets arises from coupling of intrinsic spins on adjacent atoms or atomic ions. In order to discuss organic-based magnetic materials it will be necessary to discuss them from the point of view of individual molecules or molecular ions and the electronic orbitals therein where unpaired electron spins reside. Each orbital in a molecule or molecular ion may contain two electrons, and due to the Pauli principle one of these electrons must be spin-up ( $\uparrow$ ) and the other spin-down ( $\downarrow$ ) which leads to spin cancelling and no net magnetic moment. In molecular radicals at least one orbital has only one electron either spin-up or spin-down. If, by chance, these unpaired electrons interact in such a manner that they “feel” each others presence they

can align parallel ( $\uparrow\uparrow$  or  $\downarrow\downarrow$ ) or antiparallel ( $\downarrow\uparrow$  or  $\uparrow\downarrow$ ) giving rise to ferromagnetic coupling and antiferromagnetic coupling, respectively.

Unlike conventional metal or ceramic magnets, organic-based magnetic materials introduce new mechanisms or theories for inducing stabilized ferromagnetic coupling. The spin Hamiltonian,  $\mathcal{H} = -2JS_i \cdot S_j$ , describes the spin interaction between spin with the exchange constant  $J$  describing the degree of alignment between these spins.  $J > 0$  indicates ferromagnetic coupling while  $J < 0$  indicates antiferromagnetic coupling. As mentioned previously, simple magnetic coupling of adjacent electrons does not lead to bulk magnetic behavior but requires cooperative arrangements of many spins throughout the bulk of the material. The point at which a material crosses over from nonmagnetic to magnetic is reached as a function of decreasing temperature and is called its ordering temperature  $T_c$ . The  $T_c$  of a material is directly measurable in an instrument such as a SQUID magnetometer. The value of  $J$  is not measurable but is extracted from other measurable data that is fit to a model describing the coupling mechanism between spins. There are three prevailing spin coupling mechanisms that have been formulated that are known to lead to finite values of  $J$ .

The first mechanism, the Hund's rule mechanism, involves ferromagnetic exchange between spins in orthogonal orbitals (zero overlap) in the same spatial region. As the description of the mechanism suggests, this mechanism leads only to ferromagnetic coupling. Due to Hund's rule for spin multiplicity when spins in orthogonal orbitals near each other they will align parallel to each other resulting in  $J > 0$  or ferromagnetic coupling. The closer the spins approach one another the higher the value of  $J$ . An example of this mechanism, which is limited to intramolecular interactions, is found in

diatomic oxygen,  $O_2$ , where a pair of degenerate  $\pi_g$  orbitals have one electron each aligned parallel to each other. If this mechanism is extended to large numbers of spins in larger molecules in two- or three-dimensional systems then bulk ferromagnetic behavior can be observed. Examples of this type of coupling are found in single-molecule “magnets” such as  $Mn_{12}$ .<sup>10</sup>

The second of these mechanisms is the configuration interaction (CI) mechanism for spatially distant spin systems unlike the previous case example of  $O_2$ .<sup>11</sup> This mechanism requires intense calculations that include the total wave function of the system to be evaluated. Simply put this mechanism evaluates an admixture of the excited state into the ground state to approximate the system. This mechanism is used to describe either inter- or intramolecular interactions and includes mechanisms such as superexchange and double exchange. If the excited state is in a high-spin state leaving a high-spin ground state then the admixture leads to stabilized ferromagnetic or antiferromagnetic coupling. Assessment of this (CI) admixture mechanism is complex with a great deal of calculations involved and is, of course, very dependent upon the initial description of the excited and ground states or the wave functions chosen to represent them. The simplest approach involves including only those spin-carrying orbitals that couple leading to ferromagnetic interactions; however, more complex descriptions can be formulated which involve more initial information but which also lead to a better approximation of the ground state of these species.

One example of a more complex formulation of the configuration interaction is shown in Figure 2.2. Here the spin in the partially occupied molecular orbital (POMO) of the carbon atom polarizes the spin in the orthogonal bond adjacent to it. While a

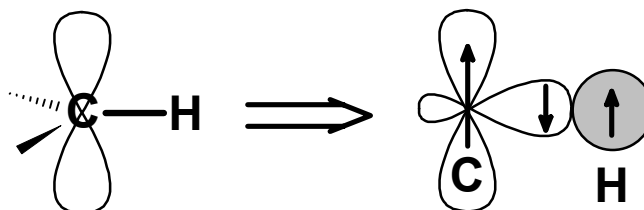


Figure 2.2. The unpaired electron spin in a carbon atom polarizing the electrons in the orthogonal bond adjacent to it as described by a CI admixture model. (After Ref. 11)

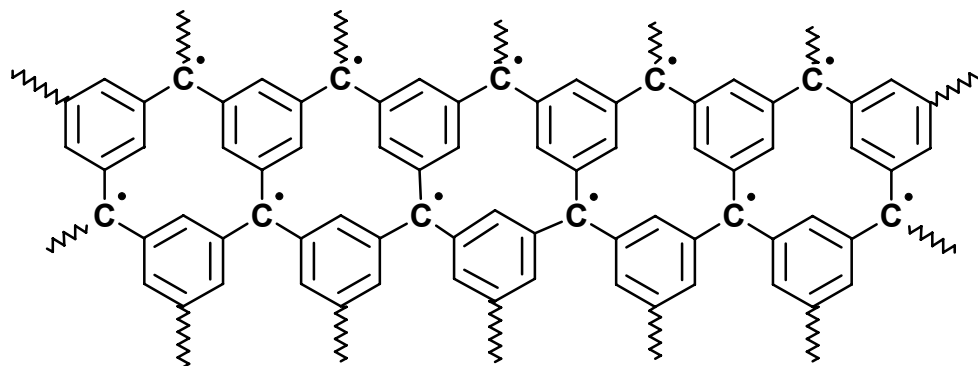


Figure 2.3. Proposed high-spin carbene sheet. (After ref. 11)

valence bond model is typical, more detailed calculations reveal that the true nature of the interaction has a small amount of antibonding character from the excited state mixed into the ground state, so the CI admixture approach is a more appropriate model for describing such interactions. A proposed example of this mechanism is a high-spin planar carbene sheet in which each of the benzene rings are *meta*-coupled diphenylcarbene moieties that have alternating hydrocarbons ferromagnetically coupling as shown in Figure 2.3.

Another example of the implementation of the CI admixture model is for alternating donor (D)-acceptor (A) charge transfer chains ( $\cdots \bar{A} \bullet^+ D \bullet^- A \bullet^+ D \bullet^- A \cdots$ ) as was described by McConnell and laid out in Ref. 12. In this case, even though spins on adjacent sites may be separated in space and energy by large amounts and frontier orbitals overlap only minimally, spins can still couple ferromagnetically or antiferromagnetically. Antiferromagnetic coupling requires that the orbitals of both the D and A are half-filled and nondegenerate. Taking ( $\bar{A} \bullet^+ D$ ) as the repeat unit then the  $D \leftarrow A$  or  $A \leftarrow D$  charge transfer results in stable antiferromagnetic coupling which lowers the total energy as depicted in Figure 2.4a. If the spins are ferromagnetically coupled the total energy of the system is not reduced. On the other hand, ferromagnetic coupling requires that the orbitals on either A or D be partially filled (not half-filled) and degenerate, A as shown in Figure 2.4b. Charge transfer  $D \leftarrow A$  stabilizes ferromagnetic coupling as shown in Figure 2.4b. Alternatively  $A \leftarrow D$  charge transfer stabilizes antiferromagnetic coupling (not shown).

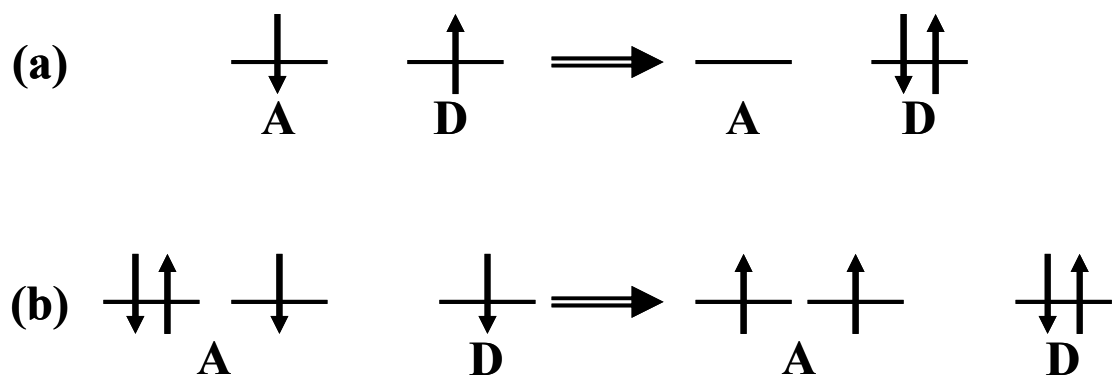


Figure 2.4. Stabilization of adjacent  $\bar{A}\bullet^+D$  units in (a) antiferromagnetic or (b) ferromagnetic coupling via configuration interaction. (After ref. 11)

The third mechanism is the dipole-dipole coupling or through-space mechanism which is also inter- or intramolecular and leads to ferro- or antiferromagnetic coupling of spins. This is the weakest of the magnetic coupling schemes, especially when it does not involve overlap of electronic orbitals. Since the magnetic interactions in this case are so weak they typically only lead to bulk magnetic behavior at very low temperatures,  $< \sim 2$  K. These interactions arise from the generation of the small magnetic fields from the electron spins. In its simplest form one can think of each electron spin as a tiny magnet, and when these tiny magnets are close to one another they can influence the direction of the magnetic moment of each other just as large macroscopic magnets do when held in the hands. Such a mechanism might explain the ferromagnetic ordering obtained in the wholly organic ferromagnet 4-nitrophenyl nitronyl nitroxide, Figure 2.5.<sup>13</sup>

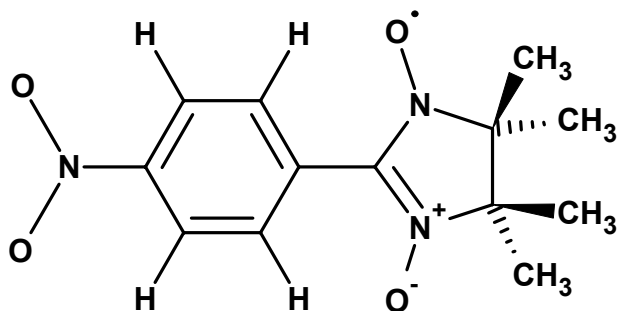


Figure 2.5. The first wholly organic ferromagnet p-nitrophenyl nitronyl nitroxide with an ordering temperature of 0.6 K.

Once again these mechanisms are used only to describe coupling between spins, magnetic ordering is a bulk solid state cooperative process. A net magnetic moment in the material will manifest itself only if there are many of these couplings working in concert throughout the bulk. For example, the CI coupling mechanism is used to explain the magnetic coupling in  $V[TCNE]_{-2}$ . This is an example of a system of alternating donors ( $V \rightarrow V^{2+}$ ) and acceptors ( $TCNE \rightarrow [TCNE]^{-}$ ) that is proposed to ferrimagnetically couple with the  $V$   $3d$  ( $S = 3/2$ ) orbitals polarizing oppositely to those of the two  $[TCNE]^{-}$   $\pi^*$  ( $S = 1/2$ ) leaving a net spin  $S = 1/2$ . The collection of many repeat units throughout the bulk of the material leads to ferrimagnetic ordering and a net magnetic moment.  $V[TCNE]_{-2}$  will now be discussed in more detail.

### 2.2.1 The Organic-Based Magnetic Semiconductor $V[TCNE]_{-2}$

Vanadium tetracyanoethylene ( $V[TCNE]_{-2}$ ) is the first reported molecule-based organic magnetic material to have a  $T_c$  above room temperature. Early versions of this material were synthesized via solution chemistry resulting in a powder. The structure was reported as a 3-D network of vanadium cations linked together via bridging from the

$[\text{TCNE}]^{\bullet-}$  ligands with solvent molecules also left incorporated into the final structure. The nature of the coordination between the vanadium centers and the solvent can have a profound effect on the magnetization versus temperature characteristics of the material as shown in Fig 2.6. As the strength of coordination of the solvent to the V increases ( $\text{CH}_2\text{Cl}_2 < \text{THF} < \text{acetonitrile}$ ) the magnitude of the magnetization decreases.<sup>14</sup> The coordinating solvent molecules replace the N atoms from the  $[\text{TCNE}]^{\bullet-}$  effectively reducing the magnetization. Immediately the mediation of the magnetic properties via these bridging  $[\text{TCNE}]^{\bullet-}$  molecules is evident.

Later on, it was discovered that thin films of  $\text{V}[\text{TCNE}]_{\sim 2}$  can be synthesized via chemical vapor deposition (CVD) techniques leaving solventless films – the form studied in this work.<sup>15</sup> Instead of the linear, nearly monotonic decrease in magnetization as shown in Fig. 2.6 for the solution prepared samples the CVD films displayed the behavior of more ordered films as shown in Fig. 2.7 where the magnetization is nearly constant through the temperature range below  $T_c$ . The sudden drop in magnetization at  $\sim 370$  K is due not to the material reaching its ordering temperature but to degradation of the material.

Magnetotransport measurements of  $\text{V}[\text{TCNE}]_{\sim 2}$  films revealed that the material has an unusually large positive magnetoresistance (MR) response that increases linearly with applied magnetic field and displays a maximum at its ordering temperature.<sup>16</sup> Fig. 2.8 shows a typical high field MR curve for  $\text{V}[\text{TCNE}]_{\sim 2}$  illustrating the unusually large MR



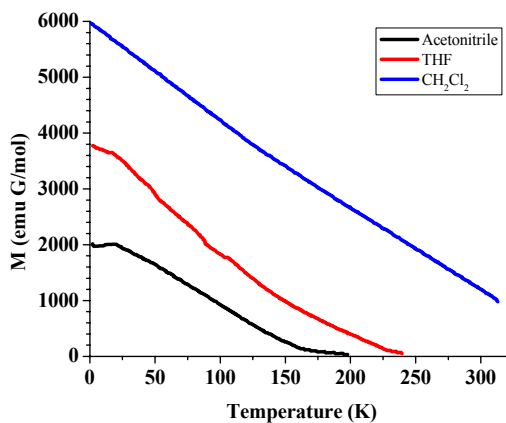


Figure 2.6. Magnetization as a function of temperature for vanadium tetracyanoethylene prepared via solvent methods in the form of  $V[TCNE]_{\sim 2} \cdot y(\text{solvent})$ . (Redrawn from Ref. 14)

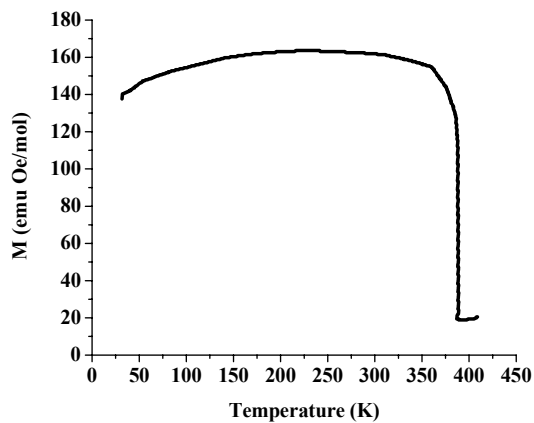


Figure 2.7. Magnetization of CVD films of  $V[TCNE]_{\sim 2}$ . The nearly constant magnetization as a function of temperature indicates an ordered film. (Redrawn from Ref. 15)

response as well as an anomalous behavior in relation to the material's ordering temperature. This curve was generated from a  $V[TCNE]_{\sim 2}$  sample with a  $T_c \sim 300K$  and as can be observed from the figure measurements taken at temperature below the  $T_c$  yield a linear MR response but those taken above the  $T_c$  yield a quadratic behavior in the MR response.

To explain this anomalous behavior Prigodin, et al. took the average stoichiometry of  $V[TCNE]_2$  per repeat unit and assumed the vanadium(II) centers have their unpaired electrons in  $3d$  orbitals yielding  $S = 3/2$  and the  $[TCNE]^{\bullet -}$  moieties have their unpaired electrons in  $\pi^*$  orbitals yielding  $S = 1/2$  each or  $S = 1$  total for the two  $[TCNE]^{\bullet -}$  per repeat. Fig. 2.9 shows the assumed spatial distribution and relative energy of these levels.

The theory developed for weak field magnetoresistance for conventional semiconductors that follow resistivity versus temperature profiles according to

$$\rho(T) = \rho_0 \exp\left[\frac{T_0}{T}\right]^{1/4} \quad (2.1)$$

yields

$$\ln\left[\frac{\rho(H,T)}{\rho(0,T)}\right] = A\left(\frac{\xi}{\lambda}\right)^4\left(\frac{T_o}{T}\right)^{3/4} \quad (2.2)$$

to model the MR response (see Ref. 17 and refs. therein). Attempts at applying this theory with the appropriate parameters for  $V[TCNE]_{\sim 2}$  predict an MR response three orders of magnitude lower than what is observed for  $V[TCNE]_{\sim 2}$ .

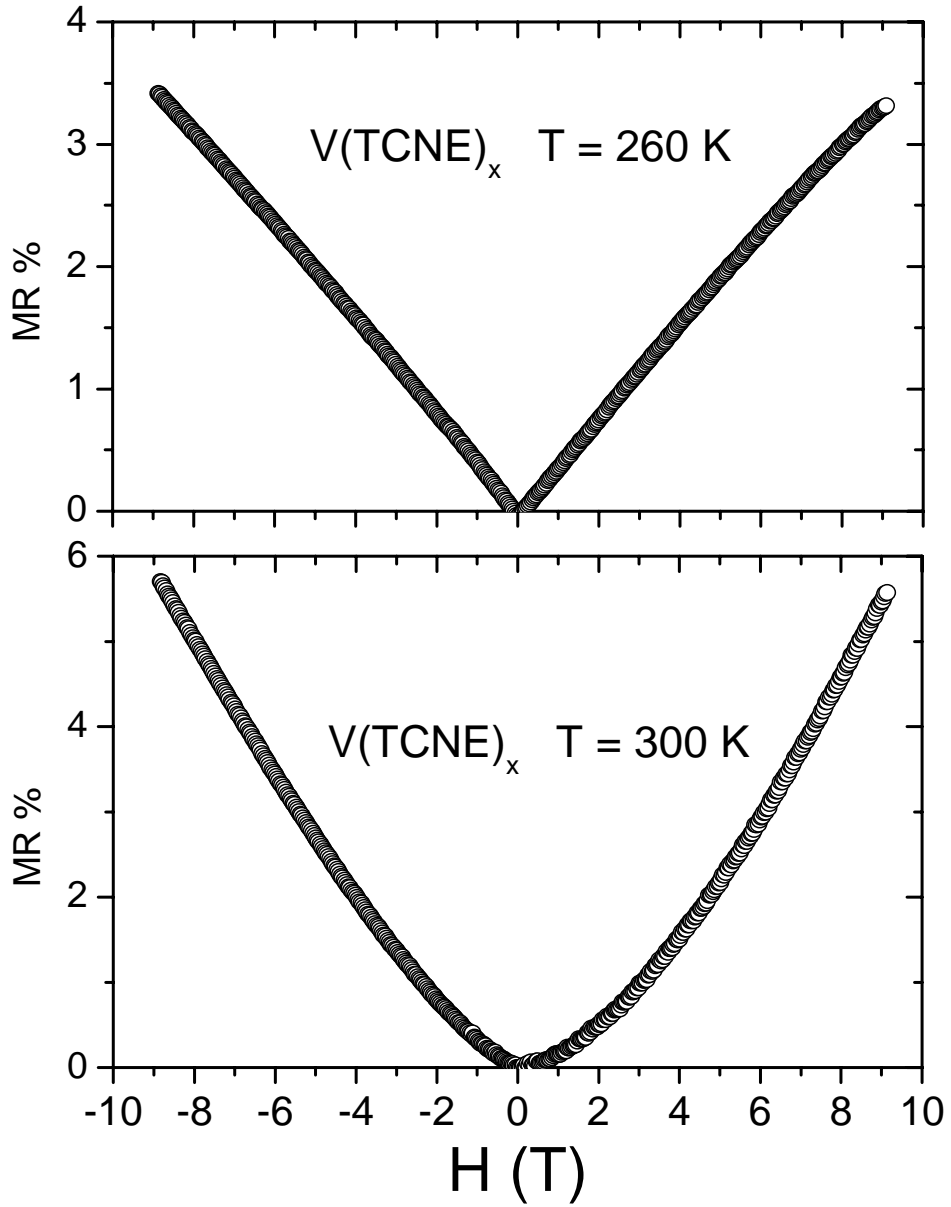


Figure 2.8. Magnetoresistance measurement results for  $V[TCNE]_{-2}$  ( $T_c > 300\text{ K}$ ) recorded at 260 K (top) and 300 K (bottom). Below  $T_c$  the magnetoresistance (MR) is linear with temperature but above  $T_c$  the MR displays a quadratic behavior.<sup>18</sup>

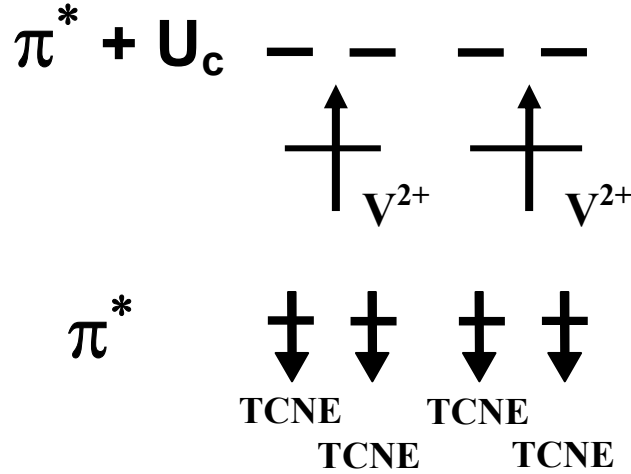


Figure 2.9. 1-D spatial distribution and relative energy alignment of the  $V^{2+}$   $3d$  and  $[TCNE]^{-}$   $\pi^*$  levels in  $V[TCNE]_2$ . Each  $[TCNE]^{-}$   $\pi^*$  orbital can accommodate two electrons with antiparallel spins, but the addition of an electron to the singly occupied molecular orbital carries with it an additional Coulomb repulsion energy,  $U_c$ . The  $\pi^* + U_c$ , a separate sub-band as viewed in this model, level is involved in hopping charge transport along with the V  $3d$  level.

Each  $V^{2+}$  is paired with two  $[TCNE]^{-}$  and the spins in the  $[TCNE]^{-}$  are aligned opposite that of the  $V^{2+}$  which gives a net magnetic spin of the  $V[TCNE]_2$  repeat of  $S_{tot} = (S = 3/2) - 2(S = 1/2) = 1/2$ , which is consistent with the saturation magnetization of  $\sim 5400$  emu Oe/mol reported for  $V[TCNE]_2$  films. Charge transport through the materials is suggested to occur via an electron hopping mechanism involving the TCNE  $\pi^* + U_c$  and V  $3d$  levels. The  $\pi^* + U_c$  level, viewed as separate sub-band in this model, arises from the Coulomb repulsion energy,  $U_c$ , from placing a second electron in the already singly occupied  $\pi^*$  orbital in accordance with the Hubbard model.<sup>19</sup>

Following this model (see Refs. 16, 17, and 20) of oppositely polarized sub-bands the energy gap of the system is approximated as  $\Delta E = U_c - 4J\langle S \rangle \langle \sigma \rangle$ , where  $U_c$  is the

aforementioned coulomb repulsion energy of the  $\pi^*$  orbital,  $J$  is the magnetic exchange constant,  $\langle S \rangle$  is the spin = 3/2 polarization of the V 3d sub-band, and  $\langle \sigma \rangle$  is the spin = 1/2 polarization of the  $\pi^*$  sub-band. The application of a magnetic field to V[TCNE]<sub>~2</sub> polarizes the electrons spins, i.e. induces paramagnetic behavior, which increases on nearing the ordering temperature,  $T_c$ . Above  $T_c$  within the mean field approximation  $\langle S \rangle \sim -\langle \sigma \rangle \sim \chi h$ , where  $\chi$  is the Curie-Weiss susceptibility per spin,  $\chi = 1/\delta$  ( $\delta = (T-T_c)/T_c$ , the "distance" from  $T_c$ ) and  $h = \mu_B H / (k_B T_c)$ , where  $H$  is the applied field,  $h^{2/3} \ll \delta \ll 1$ , where  $h^{2/3}$  defines some critical region around  $T_c$ . The model reproduces the quadratic dependence of the MR on field as seen in Fig. 2.8, the  $MR \sim (h/\delta)^2$ . In some critical region around  $T_c$  where  $|\delta| \ll h^{2/3}$ , the induced polarization obeys the scaling law  $\langle S \rangle \sim -\langle \sigma \rangle \sim h^{1/3}$  and the  $MR \sim h^{2/3}$ . Below  $T_c$   $|\delta| \gg h^{2/3}$  spontaneous spin polarization occurs and  $\langle S \rangle \sim -\langle \sigma \rangle \sim |\delta|^{1/2}$   $MR \sim h/|\delta|^{1/2}$ , reproducing the linear behavior of the magnetoresistance shown in Fig. 2.8. In addition, the MR as a function of temperature has its maximum near the  $T_c$  of the V[TCNE]<sub>~2</sub> sample and the maximum MR value predicted by the model is on the order of the observed value.

The observed experimental data is thus consistent with the picture of fully spin-polarized sub-bands in V[TCNE]<sub>~2</sub> in which the valence and conduction bands are described to be oppositely polarized to each other. This has been termed a half-semiconducting state – a very desirable situation for applications such as spin-valve devices. However, there remains to date no experimental evidence of this spin-polarized sub-band model in V[TCNE]<sub>~2</sub>, which is the focus of this work.

## **2.3 X-ray Absorption Spectroscopy (XAS) & Magnetic Circular Dichroism (MCD)**

X-ray absorption spectroscopy (XAS) is a broad term that encompasses a number of techniques that have become standard techniques for probing the electronic and atomic structure surrounding a specific element, and with the synchrotron radiation facilities available today XAS techniques are among the most powerful experimental techniques available to probe local structure in and surrounding atoms. XAS is typically broken down in to two categories – near-edge x-ray fine structure (NEXAFS, also know as x-ray absorption near edge structure or XANES) and extended x-ray absorption fine structure (EXAFS). The latter is a technique that examines x-ray absorption far above the absorption edge ( $>30$  eV) by analyzing oscillations in absorption spectra to determine bonding and the coordination environment. NEXAFS is the primary experimental technique used in this work and will be detailed more below and in following sections.

For the sake for brevity, NEXAFS will be referred to by its broader term XAS throughout the remainder of this work. Briefly, the XAS technique functions by irradiating a sample with x-rays in the energy range of  $\sim 100$ - $1000$  eV. X-rays in resonance with core level electrons are absorbed causing the core electron to be excited, see Fig. 2.10. Unlike photoelectron emission spectroscopies in which electrons are excited into the continuum the electrons in XAS are captured in unoccupied orbitals above the Fermi energy level. In this respect XAS is a probe of the electronic structure of the unoccupied states of an atom. Since the core electron binding energies of different atoms vary in energy, XAS is an element specific probe of the unoccupied electronic structure.

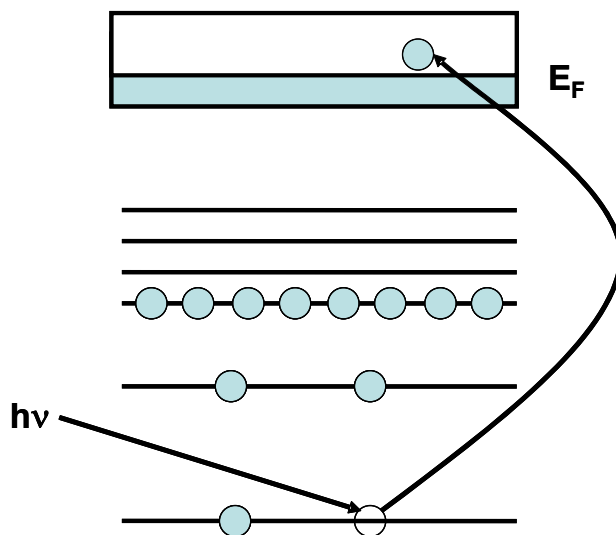


Figure 2.10. Schematic representation of the x-ray absorption process. X-rays in the energy range of  $\sim 100\text{-}1000$  eV in resonance with core level electrons are absorbed exciting the electrons to unoccupied orbitals above the Fermi energy level.

XAS involves the use of high-intensity synchrotron radiation that can be scanned through the available energy range. This being the case, a number of transitions (binding energies) can be accessed for different elements. As the radiation energy is scanned sharp rises in the absorption will be observed as the material absorbs incoming photons according to the Beer-Lambert law,  $I(\omega) = I_0(\omega)e^{-\mu(\omega)x}$ , where  $I$  is the transmitted intensity,  $I_0$  is the incident intensity,  $\mu$  is the absorption cross-section and  $x$  is the sample thickness. These sharp rises are known as absorption edges. The leading edge of the absorption is determined by the binding energy of the core electrons being excited to the lowest energy unoccupied state. Higher energies indicate excitation of the core electrons into higher energy empty states. In principle, all core electrons can be excited into empty states; however, the dipole selection rules drastically curtail the probability of some

transitions and quadrupole transitions are typically markedly less intense. The spectral shape of the absorption edge is determined by electron correlation effects and the density of empty states or multiple scattering effects.<sup>21</sup> Commonly dipole allowed transitions are those at the K-edge which indicates a transition from the  $1s$  core level,  $L_1$ -edge from the  $2s$ ,  $M_1$  from the  $3s$ , and  $N_1$  from the  $4s$ .  $L_2$ - and  $L_3$ -edge absorptions occur from the  $2p$  with the difference being due to spin orbit coupling of the  $2p$  level.  $M_2$ - $M_3$  and  $N_2$ - $N_3$  absorptions come from the  $3p$  and  $4p$  levels with their associated spin orbit splittings. Similarly,  $M_4$ - $M_5$  and  $N_4$ - $N_5$  absorption occur originate from the  $3d$  and  $4d$  levels, respectively. K-edge and L-edge absorptions are the only ones discussed in this work and will be detailed later on.

Magnetic circular dichroism (MCD), or more specifically x-ray MCD (XMCD), is a measure of the difference between the absorption of left- and right-circularly polarized x-rays by a ferro- or ferrimagnetic material. In using circularly polarized x-ray radiation one measures the magnetic absorption cross-section of the material which is directly proportional to the mean value of its magnetization,  $\langle \mathbf{M} \rangle$ . Thus, MCD via XAS is an element specific probe of the magnetization of a material that allows one to quantify the contributions of both the spin and orbital angular momenta through the use of powerful sum rules.<sup>22,23</sup> In addition, spin orientations can be determined from the sign of the MCD curves and magnetic and non-magnetic entities can be separated in heterogeneous magnetic systems.

The MCD effect is a result of polarization-dependent selection rules, or rather there is a difference in the transition probabilities for left- and right-circularly polarized x-rays based not only on the initial state but the available final states as well as shown in Fig.



2.11. If we take + as left and – as right circular polarization then the polarization dependent absorption cross-sections are given as

$$\begin{aligned}\sigma_+ &\propto \alpha^+_{\uparrow}\rho_{\uparrow} + \alpha^+_{\downarrow}\rho_{\downarrow} \\ \sigma_- &\propto \alpha^-_{\uparrow}\rho_{\uparrow} + \alpha^-_{\downarrow}\rho_{\downarrow}\end{aligned}$$

where  $\alpha^+_{\uparrow}$  and  $\alpha^+_{\downarrow}$  are the electron photoexcitation rates for up and down spin, respectively, for left circular polarization; similar for  $\alpha^-_{\uparrow}$  and  $\alpha^-_{\downarrow}$  for right circular polarization. As it turns out the probability of exciting spin-up and spin-down electrons from the  $L_2$  edge is 25% and 75% with left circularly polarized light, respectively, while the probability of exciting spin-up and spin-down electrons with right circularly polarized light is 75% and 25% , respectively. For the  $L_3$  edge the probabilities are 62.5% (spin-up) and 37.5% (spin-down) with left and 37.5% (spin-up) and 62.5% (spin-down) with right circularly polarized light.<sup>24</sup> It is these differences in transition probabilities that give rise to the MCD signal in magnetic materials.

It should be noted that the absence of spin orbit coupling in both the initial and final states gives rise to equal probabilities of exciting spin-up and spin-down electrons and, thus, no MCD signal will be produced. Spin orbit coupling in only the final state, such as is the case with K-edge absorption, will produce an MCD signal, but because the angular parts of the dipole transition matrix are the same for both left and right circular polarizations the MCD signal produced contains information only about the orbital moment and not the spin moment, which is the case in  $1s - 2p$  transitions. Spin orbit coupling in both the initial and final states leads to an MCD signal containing information about *both* the orbital and spin moments such as is the case in  $2p - 3d$  transitions. Both of these types of transitions and subsequent MCD signals are measured in this work.

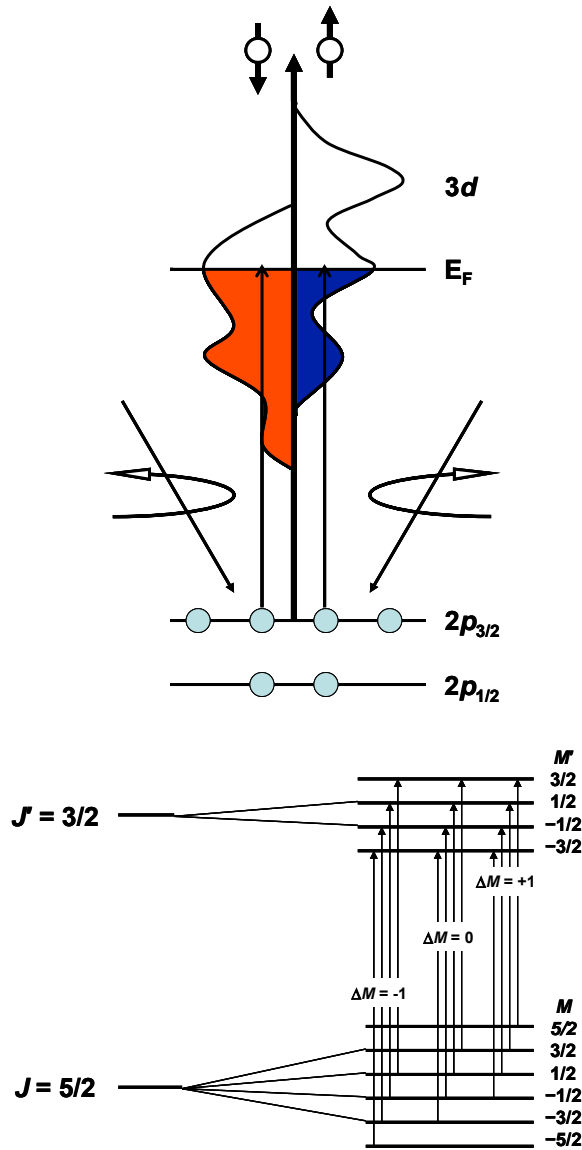


Figure 2.11. Top – A schematic representation of the MCD process for, e.g., L-edge absorption. Circularly polarized x-ray radiation excites electrons whose spin polarization depends on the edge from which it is excited,  $L_2$  or  $L_3$ . These spin polarized electrons are then injected into unoccupied  $3d$  orbitals. In a magnetic material there exists an unbalance in the number of available empty spin-up and spin-down states causing the absorption of the polarized radiation to be different. Bottom – an example of the dipole allowed transitions for a typical transition metal, given as  $2p^6 3d^N \rightarrow 2p^5 3d^{N+1}$ , where  $\Delta M$  indicates the polarization of the incident photons. (Adapted from Ref. 24 and 25)

The discussion will now turn to the theoretical treatment employed to model the experimental XAS and MCD spectra collected in this work in an attempt to determine the electronic structure of V[TCNE]<sub>2</sub> and the origin of the magnetic interaction between the V and TCNE sub-lattices.

## 2.4 Atomic, Crystal Field, and Charge Transfer Multiplet Theories

There are a number of theoretical treatments that have been developed over the years for studying both XAS and MCD spectra.<sup>26</sup> The following gives a brief overview of the fundamental basis of the theory employed in this work for modeling the experimental XAS and MCD spectra collected.

The spectral intensity of an XAS absorption edge is described beginning with the Fermi Golden Rule:

$$I_{XAS} \sim \left| \langle \Phi_f | \hat{\mathbf{e}} \cdot \mathbf{r} | \Phi_i \rangle \right|^2 \delta_{E_f - E_i - \hbar\omega} \quad (2.3)$$

Here,  $\Phi_f$  and  $\Phi_i$  are the final and initial states, respectively;  $\hat{\mathbf{e}} \cdot \mathbf{r}$  is the dipole matrix element and  $\delta_{E_f - E_i - \hbar\omega}$  accounts for the conservation of energy. In the fast approximation regime we approximate the final state as a core excited state, i.e. a core electron removed and a continuum electron added. Using this approximation we can rewrite the matrix elements ignoring all other electrons that are not involved in the transition. All other electron rearrangements are ignored as well. The absorption intensity is then given by

$$I_{XAS} \sim \left| \langle c | \hat{\mathbf{e}} \cdot \mathbf{r} | \varepsilon \rangle \right|^2 \cdot \rho \quad (2.4)$$

where  $\varepsilon$  is the continuum electron,  $c$  is the core-hole, and  $\rho$  is the density of states. The above equation then suggests that the orbital moment may only differ from the core state

by one ( $\Delta L = \pm 1$ ) as well as spin is conserved ( $\Delta S = 0$ ). Generally speaking the quadrupole transitions are ca. 100 times weaker than the dipole transitions and can be neglected. For tetrahedrally coordinated ions the quadrupole contribution is large in the pre-edge region of the absorption; however, in this case, the vanadium metals centers are octahedrally coordinated and the quadrupole transition can be ignored.

In general, for  $1s$  K-edge XAS of metal centers, as well as ligands, these one-electron approximations are suitable and give very good agreement to experimental data. In  $2p$  edge XAS, however, the single-particle approximation breaks down because of the strong overlap between the core-hole wave function and the  $3d$  valence wave functions. This overlap of these wave functions must be considered in order to obtain a good approximation of the spectral absorption edge.

$$I_{XAS} \sim \left| \left\langle 3d^N \left| \hat{e} \cdot \mathbf{r} \right| 2p^5 3d^{N+1} \right\rangle \right|^2 \delta_{E_f - E_i - \hbar\omega} \quad (2.5)$$

The model used here begins with atomic multiplet theory. The first problem encountered in utilizing atomic multiplet theory in the case of XAS of V[TCNE]<sub>2</sub> films is that it is a condensed solid possessing an extended valence structure but core-holes localized on specific atomic positions. A solution to this predicament is to treat the core-hole using a localized approach such as atomic multiplet theory and a more itinerant approach (band theory) for the ground state.

We begin by attacking the core-hole issue starting with the atomic Hamiltonian:

$$H = \left( \sum_N \frac{p_i^2}{2m} + \sum_N \frac{-Ze^2}{r_i} \right) + \sum_{i \neq j} \frac{e^2}{r_{ij}} + \sum_N \zeta(r_i) l_i \cdot s_i \quad (2.6)$$

The first term in parentheses,  $H_{ave}$ , contains the kinetic energy term and the interaction with the nucleus and is the same for all electrons in a given configuration, e.g.  $3d^3$  for

$V[\text{TCNE}]_{\sim 2}$ . This term determines the average energy for a given state. The next term represents the electron-electron repulsion,  $H_{ee}$ . The last term,  $H_{ls}$ , represents the spin-orbit coupling.  $H_{ee}$  is too large to be solved using perturbation techniques and is instead addressed using the central field approximation in which the spherical average of the electron-electron interaction is separated from the non-spherical part as shown below

$$H'_{ee} = H_{ee} - \langle H_{ee} \rangle = \sum_{i \neq j} \frac{e^2}{r_{ij}} - \left\langle \sum_{i \neq j} \frac{e^2}{r_{ij}} \right\rangle \quad (2.7)$$

The non-spherical part,  $H'_{ee}$ , is left having had the spherical part,  $\langle H_{ee} \rangle$  subtracted.  $\langle H_{ee} \rangle$  is then added into  $H_{ave}$  to make up the average energy of the configuration. We are now left with two terms required to calculate the energy of the configurations,  $H'_{ee}$  and  $H_{ls}$ .

In order to proceed with the next step of determining the matrix elements, we must first determine the term symbols of the various configurations involved in the transitions. This includes the initial and final states as well as any mixed states that may be used as will be discussed later. Details of the procedure for finding these term symbols are given in Appendix A.

After determining the number and symmetries associated with each specific configuration, the matrix elements of these states are found using the atomic Hamiltonian described above

$$H_{atom} = \sum_{i \neq j} \frac{e^2}{r_{ij}} + \sum_N \zeta(r_i) l_i \cdot s_i \quad (2.8)$$

where the first term is now the non-spherical portion of the electron-electron repulsion

term. Since the electron-electron repulsion term commutes with  $L^2$ ,  $S^2$ ,  $L_z$ , and  $S_z$ , all of the off-diagonal elements are zero. The general formula for the matrix elements is

$$\left\langle {}^{2S+1}L_J \left| \frac{e^2}{r_{12}} \right| {}^{2S+1}L_J \right\rangle = \sum_k f_k F^k + \sum_k g_k G^k \quad (2.9)$$

where  $F^k$  and  $G^k$  are the Slater-Condon parameters for the radial part of the direct Coulomb repulsion and the Coulomb exchange interaction, respectively, and  $f_k$  and  $g_k$  are the angular parts of the same. The angular parts are determined based on the values of  $l$  and are nonzero only for certain values of  $k$ . Specifics on the calculation of  $f_k$  and  $g_k$  using angular momentum coupling can be found in Ref. 27. Briefly, for  $k = 0$  the direct Coulomb repulsion term,  $f_0$ , is always present. The maximum value of  $k$  for this term is twice the lowest value of  $l$ ; for example, in a  $3d^N$  system  $k_{max} = 4$  for a  $2p^5 3d^{N+1}$  system  $k_{max} = 2$ . Thus, we would have  $f_0, f_2$ , and  $f_4$  for  $3d^N$  and  $f_0$  and  $f_2$  for  $2p^5 3d^{N+1}$ . The Coulomb exchange interaction term,  $g_k$ , will only be present for electrons in different shells and  $k$  will be even if  $l_1 + l_2$  is even and odd if  $l_1 + l_2$  is odd with a maximum value of  $l_1 + l_2$ . For the  $2p^5 3d^{N+1}$  system we have  $g_1$  and  $g_3$ .

Once the matrix elements are determined the term with the lowest energy can be identified or one can use Hund's rules. Hund's rules are used to determine the lowest energy state given a set of term symbols for a given electron configuration. The three Hund's rules state that 1) the term symbol with the maximum spin moment,  $S$ , has the lowest energy; 2) the term symbol with the maximum orbital moment,  $L$ , has the lowest energy; and 3) the term symbol with the maximum total moment,  $J = L + S$ , has the lowest energy if the shell is more than half full or the term symbol with the minimum total moment,  $J = L - S$ , has the lowest energy if the shell is less than half full. In the case of

the  $3d^3$  configuration for  $V^{2+}$  where the shell is less than half full the lowest energy term symbol from those determined in Appendix A is  $^4F_{3/2}$ . It is from this term that all the allowed transitions are calculated. The x-ray absorption transitions from this ground state are governed by the dipole selection rule in which  $\Delta J = 0, \pm 1$ . In the case of the  $3d^3 \rightarrow 2p^5 3d^4$  transition for  $V^{2+}$  there are 19 term symbols in the ground state and 180 term symbols in the final state with 95 allowed transitions allowed between them or 95 atomic multiplets (see Appendix A). The XAS transition matrix elements are calculated according to

$$I_{XAS} \propto \langle 3d^3 | p | 2p^5 3d^4 \rangle \quad (2.10)$$

and using the symmetries of the initial and final states as well as the dipole transition,  $^1P_1$

$$I_{XAS} \propto \left\langle \left[ ^4F_{\frac{3}{2}} \right] \left[ ^1P_1 \right] \left[ \text{Final Terms} \right] \right\rangle \quad (2.11)$$

where the final terms are

$$\begin{aligned} &^2S_{\frac{1}{2}}, ^4S_{\frac{3}{2}}, ^2P_{\frac{1}{2}, \frac{3}{2}}, ^4P_{\frac{1}{2}, \frac{3}{2}, \frac{5}{2}}, ^6P_{\frac{3}{2}, \frac{5}{2}, \frac{7}{2}}, ^2D_{\frac{3}{2}, \frac{5}{2}}, ^4D_{\frac{1}{2}, \frac{3}{2}, \frac{5}{2}, \frac{7}{2}}, ^6D_{\frac{1}{2}, \frac{3}{2}, \frac{5}{2}, \frac{7}{2}, \frac{9}{2}}, ^2F_{\frac{3}{2}, \frac{7}{2}}, ^4F_{\frac{3}{2}, \frac{5}{2}, \frac{7}{2}, \frac{9}{2}}, \\ &^6F_{\frac{1}{2}, \frac{3}{2}, \frac{5}{2}, \frac{7}{2}, \frac{9}{2}, \frac{11}{2}}, ^2G_{\frac{7}{2}, \frac{9}{2}}, ^4G_{\frac{5}{2}, \frac{7}{2}, \frac{9}{2}, \frac{11}{2}}, ^2H_{\frac{9}{2}, \frac{11}{2}}, ^4H_{\frac{7}{2}, \frac{9}{2}, \frac{11}{2}, \frac{13}{2}}, ^2I_{\frac{11}{2}, \frac{13}{2}}, ^4I_{\frac{9}{2}, \frac{11}{2}, \frac{13}{2}, \frac{15}{2}}, ^2J_{\frac{13}{2}, \frac{15}{2}} \end{aligned}$$

with 2 terms for each of the  $^2S$ ,  $^4S$ ,  $^4H$ ,  $^2I$ ; 4 terms for each of the  $^4P$ ,  $^4G$ ; 5 terms for each of the  $^4F$ ,  $^2H$ ; 6 terms for each of the  $^4D$ ; 7 terms for each of the  $^2P$ ,  $^2G$ ; 8 terms for each of the  $^2D$ ; and 9 terms for each of the  $^2F$ . However, according to the dipole selection rule only those terms where  $\Delta J = 1/2$  (21 terms),  $3/2$  (35 terms), or  $5/2$  (39 terms) are allowed leaving only

$$^2S_{\frac{1}{2}}, ^4S_{\frac{3}{2}}, ^2P_{\frac{1}{2}, \frac{3}{2}}, ^4P_{\frac{1}{2}, \frac{3}{2}, \frac{5}{2}}, ^6P_{\frac{3}{2}, \frac{5}{2}}, ^2D_{\frac{3}{2}, \frac{5}{2}}, ^4D_{\frac{1}{2}, \frac{3}{2}, \frac{5}{2}}, ^6D_{\frac{1}{2}, \frac{3}{2}, \frac{5}{2}}, ^2F_{\frac{3}{2}}, ^4F_{\frac{3}{2}, \frac{5}{2}}, ^6F_{\frac{1}{2}, \frac{3}{2}, \frac{5}{2}}, ^4G_{\frac{5}{2}}$$

with 2 terms for each of the  $^2S$ ,  $^4S$ ; 4 terms for each of the  $^4P$ ,  $^4G$ ; 5 terms for each of the  $^4F$ ; 6 terms for each of the  $^4D$ ; 7 terms for each of the  $^2P$ ; 8 terms for each of the  $^2D$ ; and 9 terms for each of the  $^2F$ . This constitutes 95 allowed transitions from the initial  $3d^3$  state to the  $2p^53d^4$  final state.

Despite the careful treatment using atomic multiplet theory in the case of condensed solids containing  $3d$  metal centers, the XAS spectra still cannot be accurately described because of the influence of neighboring atoms. To address this shortcoming of the atomic multiplet theory the symmetry effects and configuration interaction or charge transfer effects must be included explicitly. The first of these effects, symmetry, is modeled using crystal field multiplet (CFM) theory. The CFM model approximates the metal center as an isolated ion surrounded by some distribution of charge that appropriately mimics the surrounding environment of other ions, atoms or molecules. It has its roots in the symmetry surrounding the isolated ion and, as such, relies heavily on group theory, which generally speaking is what CFM theory does – translates results from spherical symmetry (atomic theory) to lower symmetries such as octahedral, tetrahedral, and so on. To begin the discussion of CFM theory, the Hamiltonian consists of the atomic Hamiltonian as described by Eq. 2.6 plus an electrostatic term  $H_{FIELD} = -e\phi(\mathbf{r})$  where  $e$  is the electronic charge and  $\phi(r)$  is the potential that describes the surroundings. This electrostatic term is simply viewed as a perturbation to the atomic Hamiltonian and the matrix elements need to be determined in a similar manner with this added perturbation.

For  $3d$  transition metal compounds the most common symmetry encountered is the cubic symmetry,  $O_h$ , where 6 ligands are octahedrally coordinated around the metal ion



center, or quite simply, located on the faces of a cube with the metal atom at the center. The cubic symmetry of these compounds has the effect of lifting the degeneracy of the 5  $d$ -orbitals into sets of 2-fold degenerate and 3-fold degenerate orbitals. The magnitude of the splitting of these two sets of orbitals is known as the crystal field splitting strength,  $10Dq$ . The 2-fold degenerate orbitals have  $E_g$  symmetry in which the  $d_{z^2}$  or  $d_{2z^2-x^2-y^2}$  and  $d_{x^2-y^2}$  that lie along the bonding axes between the metal centers and the ligands are repelled more strongly than the  $d_{xy}$ ,  $d_{xz}$ , and  $d_{yz}$  ( $T_{2g}$ ) orbitals that lie between the axes, and thus, possess a higher energy. It is this concept that is the link between the atomic multiplet calculations described above and the extension to crystal field theory. The atomic multiplet calculations are accomplished under spherical symmetry,  $SO_3$ ; whereas, crystal field calculations are accomplished under a somewhat lower symmetry such as  $O_h$ . Under octahedral symmetry a D state branches to the aforementioned  $E_g$  and  $T_{2g}$  symmetries,  $A_1 + B_1$  and  $E + B_2$  for tetragonal symmetry and so on for even lower symmetries. Likewise, dipole operator with P symmetry is transformed to  $T_{1u}$  symmetry.

Once the matrix elements are determined for the initial state, final state, and transition operator Hamiltonians the energies can be calculated for the various transitions. Certain considerations must be taken for the Slater-Condon parameters which are sometimes reduced to account for atomic interactions.<sup>28</sup> The value of  $10Dq$  also must be considered carefully as it determines the spin state (high or low) for  $3d^4$  to  $3d^7$  configurations. Further, the decision of whether or not to include the 3d spin orbit coupling parameter must be considered depending on the system as quenching of the coupling sometimes occurs. Finally, additional parameters for lower symmetries need to be included to

adequately model the experimental spectrum; for example,  $D_s$  and  $D_t$  are additional parameters in  $D_{4h}$  symmetry which are akin to  $10Dq$  in  $O_h$  symmetry.

If CFM theory fails to provide an adequate model of the experimental data, then including charge transfer effects may provide a better fit. Charge transfer multiplet theory (CTM) differs from CFM theory in that more than one configuration is used to model charge fluctuation effects in the initial and final states, or rather it is an extension of CFM to include additional configurations.

The CTM model is based upon the Anderson impurity model which describes the interaction of a localized state with delocalized electrons in bands.<sup>29</sup> The Anderson impurity Hamiltonian is described by four terms: 1) the localized state, e.g. a  $3d$  state; 2) the correlation within that state to include the electron-electron correlation energy,  $U_{dd}$ ; 3) the valence band; and 4) coupling of the localized state with the valence band to include a hopping or transfer integral between the two,  $t$ . Inclusion of the multiplet model alters the Hamiltonian by replacing the single localized state by all of the states that are part of the crystal field multiplet Hamiltonian for the configuration of interest. Several new parameters are also introduced: a term that describes all the two-electron integrals, the Hubbard potential  $U$ , and the Slater-Condon parameters. In addition, new terms describing the  $3d$  spin orbit coupling and the crystal field potential are added. In effect the single localized state has now become a multiplet of localized states and the band has become a delocalized density of empty states.

If an electron is relocated from the valence band to the  $3d$  state the configuration of the  $3d$  band changes from  $3d^N$  to  $3d^{N+1}$ . The occupation of the valence band also decreases by one or now contains a hole which is denoted  $\underline{L}$ . Since the CTM model is

commonly used for transition metal compounds the valence band largely has ligand character, e.g. in the case of transition metal oxides the valence band has O  $2p$  character. Considering this charge transfer effect, the effect on the initial state wave function prior to absorption of x-rays becomes  $3d^N + 3d^{N+1}\underline{L}$ , where  $\underline{L}$  simulates the ligand hole.

The intensity of the XAS absorption spectrum then becomes Eq. 2.5 plus a second initial and final state dipole transition represented by

$$I_{XAS} \sim \left| \langle 3d^{N+1}\underline{L} | \hat{e} \cdot \mathbf{r} | 2p^5 3d^{N+2}\underline{L} \rangle \right|^2 \delta_{E_f - E_i - \hbar\omega} \quad (2.12)$$

where the two initial states and the two final states are coupled by monopole transitions given by

$$H_{mono,init} = \langle 3d^N | t / \Delta | 3d^{N+1}\underline{L} \rangle \quad (2.13)$$

and

$$H_{mono,final} = \langle 2p^5 3d^{N+1} | t / \Delta | 2p^5 3d^{N+2}\underline{L} \rangle \quad (2.14)$$

where  $t$  is the mixing parameter and  $\Delta$  is the energy difference between the two configurations. The x-ray absorption spectrum is then calculated by solving equations 2.5 and 2.12 through 2.14.

In order to obtain a spectrum for comparison to experiment once the energy and intensity of the various multiplet states have been calculated, the calculated line spectrum must be broadened. Lorentzian broadening is used to simulate finite lifetime effects of the core-hole essentially indicating the uncertainty in the peak energy due to the Heisenberg uncertainty principle. Gaussian broadening is used to simulate the resolution function of the specific experiment. The Lorentzian broadening will of course differ depending upon the metal center of interest but will also differ within the same spectrum

due to various effects. Comparison of calculated and experimental spectra have shown that the broadening of the  $L_3$  and  $L_2$  lines is different by up to as much as 0.5 eV at half-width half-maximum because of an additional Auger decay process in the  $L_2$  line.<sup>30</sup> In addition, differences in vibrational effects on the  $t_{2g}$  versus  $e_g$  orbitals or differences in hybridization effects can lead to different broadenings in peaks ascribed to those two states.

## 2.5 Organic Field-Effect Transistors (OFET)

The basic architecture of organic field effect transistors (OFET) is shown in Fig. 2.12. This is the same basic architecture for both organic and inorganic FETs. The main architecture involves a thin, semiconducting organic layer that is separated from a gate electrode by an insulating or dielectric material. The semiconducting layer is vacuum deposited, spin coated, or otherwise grown between source and drain electrodes a distance  $l$  apart, known as the channel length, and of width  $w$ . Source-drain electrodes are typically fabricated out of inert/noble metals such as gold<sup>31</sup> or platinum<sup>32</sup>, but conducting polymers have also been used.<sup>33</sup> The gate electrode is typically a metal or inorganic semiconductor such as highly doped silicon, but conducting polymers have also been used.<sup>34</sup> The gate dielectric material ranges widely from insulating oxides and nitrides to polymeric materials such as poly (methylmethacrylate) (PMMA)<sup>35</sup> or carbon nanotubes.<sup>36</sup>

A separate bias is applied to the drain contact and the gate contact and the source contact is typically grounded. The potential difference between the drain and gate contacts is known as the gate voltage,  $V_g$ , and the potential difference between the source and drain contacts is known as the source-drain voltage,  $V_{sd}$ . When a positive gate

voltage is applied electrons injected from the source electrode are accumulated in the channel, and when a negative gate voltage is applied holes are injected from the source electrode and accumulated in the channel. The number of charges that is accumulated in the channel is proportional to the applied gate voltage and the capacitance of the dielectric material. From this it can easily be seen that the choice of gate dielectric material is nearly as important as the organic semiconducting channel material.

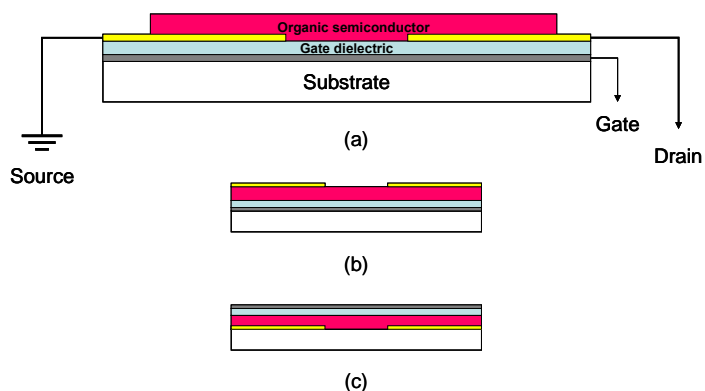


Figure 2.12. Typical OFET architectures: (a) is known as a bottom-contact, bottom-gate architecture because the source/drain contacts and the gate dielectric are both between the semiconducting layer and the substrate (this architecture is used in this work); (b) is then top-contact, bottom gate; and (c) is bottom-contact, top gate. Each color represents the same layer in all the figures.

Charges that are accumulated in the channel are not all necessarily mobile, i.e. participate in charge conduction through the channel. Especially in the case of organic semiconducting materials, charge traps must be filled first before additional charges injected may take place in channel conduction. The gate voltage then must be greater

than some threshold voltage before enough charges are injected to fill charge traps sufficiently so that charge conduction may occur. This leads to an effective gate voltage given by  $V_g - V_{th}$ , where  $V_{th}$  is the threshold voltage. Threshold voltages arise from the aforementioned charge traps as well as other sources such as impurities, interface states, and built-in dipoles.<sup>37</sup> In cases where a dark current is present, i.e. charges are accumulated in the channel with  $V_g = 0$ , a gate voltage is often applied to stop the flow of current in the channel rather than induce it. This is commonly the case with doped organic semiconductors where donor (n-channel) or acceptor (p-channel) states are present that induce an internal potential, and thus, lead to the accumulation of charge carriers in the channel.

The three operating regimes of field-effect transistors are shown in Fig. 2.13. When the source-drain voltage is zero there is a uniform concentration of charge carriers across the channel length. Small voltages, ( $V_{sd} \ll V_g - V_{th}$ ), lead to a linear charge density gradient from the source electrode to the drain electrode. In this linear regime source-drain current,  $I_{sd}$ , is directly proportional to  $V_{sd}$  (Fig. 2.13a). As  $V_{sd}$  is increased to  $V_{sd} = V_g - V_{th}$  a depletion region forms within the channel creating a pinch-off point in the charge carrier concentration (Fig. 2.13b). The local potential created by the source-drain voltage minus the gate voltage drops below the threshold voltage; however, current can still flow through the depletion regions due to the high electric field created in the depletion region.  $I_{sd}$  is severely curtailed at this point and is no longer directly proportional to  $V_{sd}$ ; this is the beginning of the saturation region. Finally, when  $V_{sd}$  is further increased to where it is much larger than  $V_g - V_{th}$ , the depletion region is

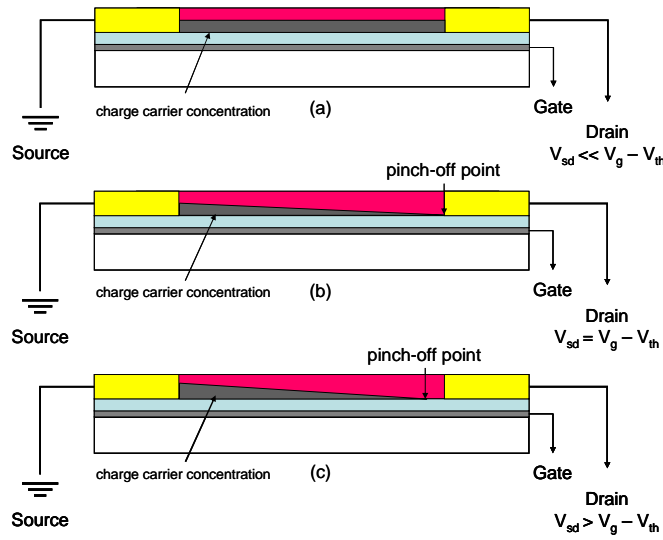


Figure 2.13. Operating regimes of field-effect transistors: (a) linear regime, (b) beginning of saturation regime, and (c) saturation regime. (After Ref. 38)

expanded leading to an effective shortening of the channel length and  $I_{sd}$  is not significantly increased by increasing  $V_{sd}$  further. The potential at the pinch-off point remains the same ( $V_g - V_{th}$ ), thus keeping the potential between the source and pinch-off point roughly the same so the current through the channel will not increase and saturates at some level (Fig. 2.13c) making this the saturation regime. The current-voltage characteristics of these different regimes are plotted in Fig. 2.14.

The typical approach to describing the current-voltage characteristic in OFETs is known as the gradual channel approximation or the Shockley model.<sup>39</sup> In the Shockley model the source-drain current,  $I_{sd}$ , depends upon the device structure as well as the source-drain and gate voltages given by Eq. 2.15. It is assumed in this model that the field perpendicular to the current flow, where current flows between the source and drain electrodes, is much larger than the field parallel to it. With this in mind one can see that

channel length is a very important parameter in the device architecture because short channel lengths can generate high electric fields.

$$I_{sd} = \frac{w}{l} \mu C_i \left[ (V_g - V_{th}) V_{sd} - \frac{1}{2} V_{sd}^2 \right] \quad (2.15)$$

where  $w$ ,  $l$ , and  $\mu$  are the channel width and length and field effect mobility, respectively.  $C_i$  is the capacitance of the gate dielectric material per unit area. It is also assumed that the mobility is independent of charge carrier density, and hence, gate voltage independent which is typically not the case. In the linear regime ( $V_{sd} \ll V_g - V_{th}$ , Fig. 2.14) this expression simplifies to

$$I_{sd,lin} = \frac{w}{l} \mu_{lin} C_i (V_g - V_{th}) V_{sd} \quad (2.16)$$

This expression allows one to then determine the field effect mobility in the linear regime via the expression

$$\mu_{lin} = \frac{\partial I_{sd}}{\partial V_g} \frac{l}{w C_i V_{sd}} \quad (2.17)$$

However, as the current is increased further the channel becomes pinched-off and Eq. 2.16 is no longer applicable as the current saturates. Eq. 2.16 then becomes

$$I_{sd,sat} = \frac{w}{l} \mu_{sat} C_i \frac{1}{2} (V_g - V_{th})^2 \quad (2.18)$$

with the substitution of  $V_g - V_{th}$  for  $V_{sd}$  in the saturation regime, Fig. 2.14. Now the field-effect mobility can also be determined for the saturation regime using the expression



$$\mu_{sat} = \frac{\partial I_{sd,sat}}{\partial V_g} \frac{l}{wC_i} \frac{1}{V_g - V_{th}} \quad (2.19)$$

Armed with this model, the basic characteristics of an OFET can be analyzed; although, there are reports of more complex models that account for, for example, the specific type of device, e.g. ambipolar,<sup>40</sup> or which include field-dependent mobilities.<sup>41</sup>

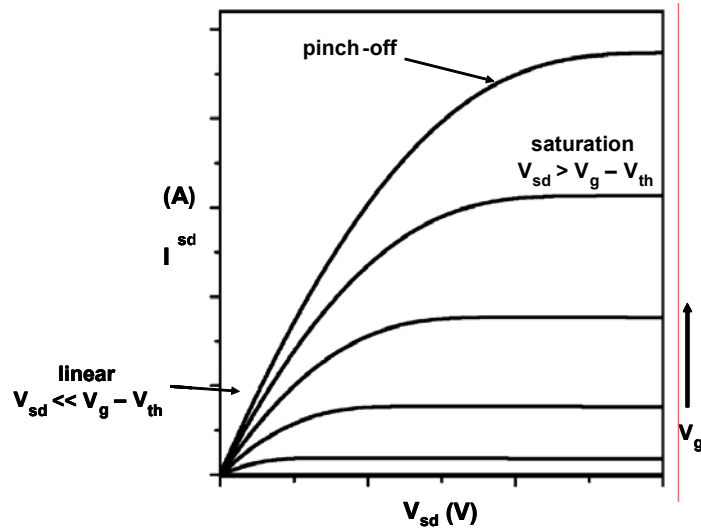


Figure 2.14. Typical current-voltage characteristics of OFETs showing the linear and saturation regimes and the effect of increasing the gate voltage. The approximate location of the pinch-off point is also indicated. (After Ref. 38)

Until recently, OFETs were generally observed to exhibit p-channel behavior, where p-channel indicates the accumulation of holes for negative applied gate voltages. This is due to the overwhelming tendency of organic semiconductors to trap electrons but not holes making hole conduction far better than electron conduction. However, recent work has shown that the gate dielectric material plays a large role in charge trapping in these

types of devices and n-channel behavior is quite attainable.<sup>42</sup> Nonetheless, motivation remains high to develop organic semiconductors that display intrinsic n-channel behavior.<sup>43</sup>

As just mentioned, the gate dielectric material plays a pivotal role in the operation of OFETs, which can also be seen by reviewing Eqs. 2.15 – 2.19. Accordingly, there is a substantial amount of work directed at improving gate dielectrics specifically for incorporation into OFETs.<sup>44</sup> Gate dielectrics must meet several stringent demands placed upon them for favorable OFET operation: 1) they must resist dielectric breakdown; 2) they must be able to generate high densities of charge carriers at low applied voltages; and 3) they must be defect free. The second requirement above is a function of the dielectric constant which is a measure of the extent to which a material concentrates the electric field lines of flux. The capacitance is a measure of the amount of electric charge stored in a material given by  $C = A\epsilon_r\epsilon_0/d$  where  $A$  is the area of the capacitor,  $\epsilon_0$  is the permittivity of free space,  $\epsilon_r$  is the dielectric constant, and  $d$  is the thickness of the capacitor. It can easily be seen that high dielectric constants will increase the capacitance and hence the charge carrier density in the conducting channel in an OFET. Thinner capacitors will have a similar effect to increase the capacitance but then the third requirement becomes an issue. Dielectrics that are too thin can lead to shorting of the device which renders it useless. Failure to meet the first requirement leads to what is known as leakage current. Leakage current is the current that flows between the drain and gate electrodes. This also effectively shorts the device and can lead to false positives for the transistoring effect because one is measuring leakage current rather than field-effect induced current changes.

## CHAPTER 3

### EXPERIMENTAL

#### 3.1 Materials

The tetracyanoethylene (TCNE) precursor used in this study, Fig 3.1, has a very rich chemistry even in ambient conditions (room temperature, humid air) owing to its ability to easily undergo both oxidation and reduction.<sup>45</sup> As such, special precautions are required in handling the material to prevent these additional chemistries from occurring during synthesis. The TCNE, 99 %, was purchased from Sigma-Aldrich and sealed and stored in a refrigerator at  $\sim 4^{\circ}\text{C}$  prior to sublimation purification. Sublimation purification was accomplished by mixing TCNE with activated carbon in a 10:1 (TCNE:C) ratio and heating to  $\sim 90^{\circ}\text{C}$  in a typical sublimation purification apparatus. After recovery the purified material was stored in a glove box argon atmosphere with  $< 1.0$  ppm  $\text{O}_2$  and  $< 1$  ppm  $\text{H}_2\text{O}$  at  $-35^{\circ}\text{C}$  until ready for use.

Vanadium hexacarbonyl ( $\text{V}(\text{CO})_6$ ) was synthesized according to published reports.<sup>46</sup> Briefly, approximately 1.5 g phosphoric acid ( $\text{H}_3\text{PO}_4$ , Sigma-Aldrich,  $\geq 98\%$ ) and 0.2 g tetraethylammonium vanadium hexacarbonyl,  $[\text{Et}_4\text{N}][\text{V}(\text{CO})_6]$  (also synthesized according to published reports,<sup>47</sup> were placed in an apparatus as shown in Fig. 3.2. Upon

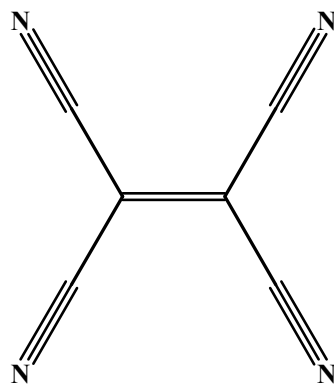


Figure 3.1. The tetracyanoethylene precursor used in depositing films of  $\text{V}[\text{TCNE}]_{\sim 2}$ . TCNE is a fine white powder in its pure form but reaction with water gives it a distinct off-white to yellow color, which offers a good indicator of the purity of the material. Once purified and stored in a very dry ( $< 1$  ppm  $\text{H}_2\text{O}$ ) atmosphere TCNE will maintain its purity for prolonged periods of time (months). Neutral TCNE and singly reduced  $[\text{TCNE}]^{\bullet -}$  have a planar  $D_{2h}$  symmetry structure, but the dianion can adopt a twisted  $D_{2d}$  structure.

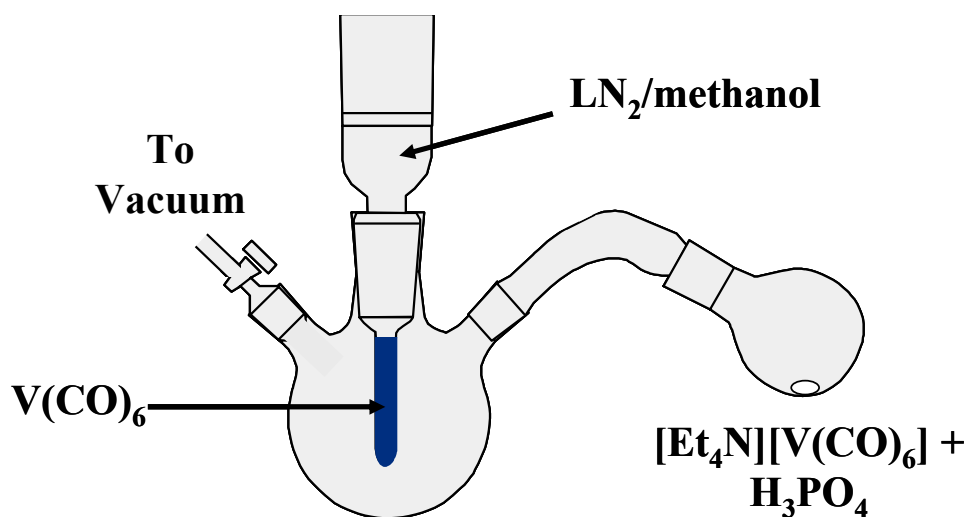


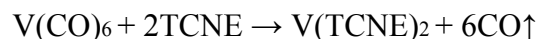
Figure 3.2. Laboratory apparatus for preparing  $\text{V}(\text{CO})_6$  for use in synthesizing  $\text{V}[\text{TCNE}]_{\sim 2}$ . The  $[\text{Et}_4\text{N}][\text{V}(\text{CO})_6]/\text{H}_3\text{PO}_4$  mixture is heated gently to  $\sim 45^\circ\text{C}$  with stirring. The blue-black product ( $\text{V}(\text{CO})_6$ ) collects on the cold finger cooled with a liquid nitrogen/methanol bath. The reaction is carried out under vacuum ( $\sim 10^{-4} - 10^{-5}$  Torr).

gentle heating to about 45 °C, blue-black V(CO)<sub>6</sub> is evolved and condenses on the cold-finger. To prevent oxidation of the newly synthesized material the entire apparatus is introduced into the glove box and the material is collected. Due to the low sublimation temperature of V(CO)<sub>6</sub> the material is stored in the glove box atmosphere at -35° C until used. Other materials used in this study include: microscope slide glass for transistor substrates (Gold Seal), silicon nitride, Si<sub>3</sub>N<sub>4</sub>, sputtering target (Feldco International, 99.9%) and poly(methylmethacrylate) (PMMA) (Sigma-Aldrich, M<sub>w</sub> = 996,000) for bilayer gate dielectric, gold evaporation pellets (Super Conductor Materials, Inc., 99.9%) for source/drain contacts, aluminum evaporation clips (Kurt J. Lesker, Co., 99.99%) for gate and source/drain contacts, and silicon nitride membrane windows for x-ray absorption studies (Silson, Ltd.).

### 3.2 Thin Film Deposition via Chemical Vapor Deposition

Thin films of vanadium tetracyanoethylene, or more formally tetracyanoethenide, (V[TCNE]<sub>x</sub>, x~2) were synthesized via chemical vapor deposition (CVD) methods.<sup>15,48</sup> The CVD apparatus as shown in Fig. 3.3 was located inside a Vacuum Atmospheres Co. glove box system under argon with < 1.0 ppm O<sub>2</sub> and < 1.0 ppm H<sub>2</sub>O where all syntheses were accomplished.

The nominal solventless stoichiometric chemistry for the reaction of TCNE with V(CO)<sub>6</sub> is



The as deposited V[TCNE]<sub>~2</sub> films are dark, bluish in appearance with a mirror like surface unless deposited on a very rough surface. X-ray photoelectron spectroscopy (XPS) studies indicate the deposited material is slightly TCNE rich with a nitrogen to

vanadium ratio (N:V) of 8.77:1, which is higher than the expected 8:1 ratio given the  $\text{V}[\text{TCNE}]_2$  stoichiometry. It should be noted that XPS is a surface sensitive technique and probes only the top 1-10 nm of material.

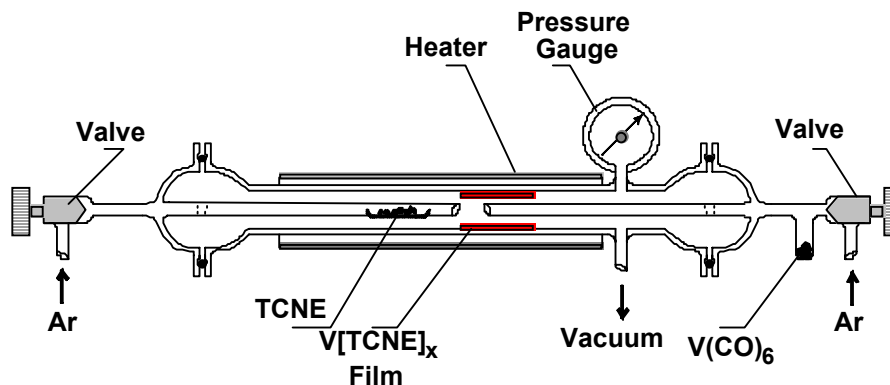


Figure 3.3. Chemical Vapor Deposition (CVD) apparatus for thin-film deposition of  $\text{V}[\text{TCNE}]_{\sim 2}$ . The TCNE side of the reactor is heated to  $\sim 60^\circ\text{C}$  and the  $\text{V}(\text{CO})_6$  side is cooled to  $10^\circ\text{C}$  in a silicon oil bath. The Ar carrier gas is pulled from the controlled atmosphere glove box in which the synthesis takes place with an environment of  $< 1$  ppm  $\text{O}_2$  and  $< 1$  ppm  $\text{H}_2\text{O}$ .

Depending on the desired duration (film thickness) of the synthesis, 50 – 100 mg of TCNE were placed in a small quartz boat in the tube as indicated in Fig. 3.3 and 5 – 10 mg of  $\text{V}(\text{CO})_6$  in the t-boat as indicated in the figure. The TCNE side of the reactor is heated to  $60^\circ\text{C}$  while the  $\text{V}(\text{CO})_6$  side is cooled to  $10^\circ\text{C}$  as it sublims too quickly at room temperature and needs to be cooled to control the rate of sublimation. The deposition zone of the reactor is also heated to  $\sim 45^\circ\text{C}$ . The entire system is pumped down to 35 Torr and argon from the glove box atmosphere is bled into the system through a  $0.5\ \mu\text{m}$  filter. The flow rate through the TCNE side of the reactor is 150 standard cubic

centimeters per minute (sccm) and the rate through the  $\text{V}(\text{CO})_6$  side is 100 sccm. Typical film deposition rates are  $\sim 150\text{-}200$  nm/hr. Upon completion of the deposition, the films are immediately sealed in vials and stored at  $-35$  °C or the devices are wired and tested with only a few hours of deposition.

The changing of the film color from the as-deposited blue-black to greenish color indicates oxidation of the film most likely forming vanadium(II) oxide which can have a greenish appearance. Prolonged exposure of the films to an oxygen atmosphere leads to complete transparency. Another indicator of degradation/oxidation of the films is an increase in resistivity most likely due to the formation of any number of the possible vanadium oxides which are not conductive at room temperature.

### **3.3 X-ray Absorption Spectroscopy Measurements**

$\text{TCNE}^0$  samples were first purified and then pressed into pellet form and placed into a quartz tube and vacuum sealed at a base pressure of  $10^{-5}$  Torr (although the pressure probably rose during shipping) all at The Ohio State university then shipped to Lawrence Berkeley National Laboratory (LBNL) for XAS measurements.

$\text{V}[\text{TCNE}]_{\sim 2}$  XAS samples were also prepared at OSU by first depositing CVD films onto silicon nitride membrane windows designed for x-ray absorption experiments as shown in Fig. 3.4. Optimal  $\text{V}[\text{TCNE}]_{\sim 2}$  film thicknesses varied from 200 – 300 nm. The CVD deposited films were immediately coated with an aluminum film  $\sim 30$  nm thick to protect the film and prevent oxidation. The entire holder was then placed in a quartz tube and vacuum sealed for shipping to LBNL for the XAS measurements.

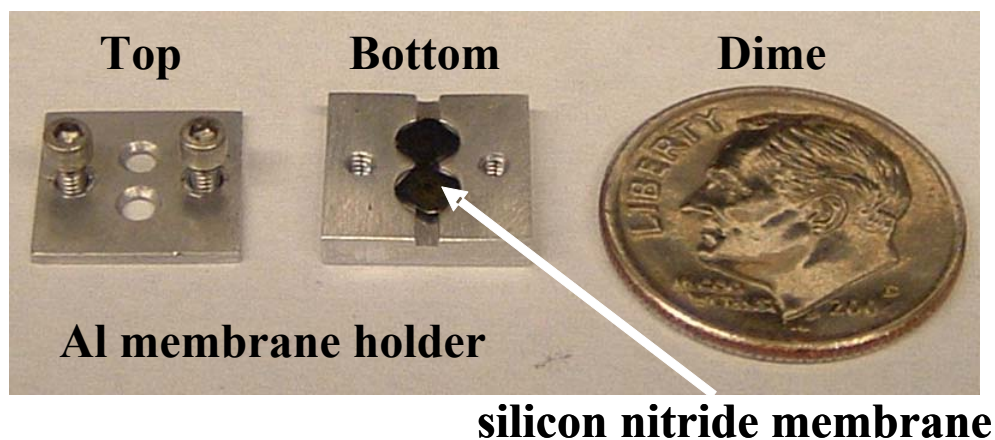


Figure 3.4. Silicon nitride membranes and specially designed holder used in the x-ray absorption experiments.  $V[TCNE]_{-2}$  films were deposited with the top removed from the holder bottom. Al protecting layers were deposited with the top in place.

At LBNL the glass tubes were placed in a nitrogen filled glove bag attached to the XAS sample chamber where they were broken and the holder placed into position. All data were collected in transmission with near circular polarization of fixed helicity in a magnetic field of  $\pm 1$  Tesla oriented along the beam direction. The samples were rotated so that the beam was incident at an angle of  $30^\circ$  from normal incidence as is common for thin magnetic films with in-plane anisotropy. The samples were at room temperature. The energy scales of the plotted data are “as measured”, i.e., no standard samples were run to provide a correction to make the energy scales absolute but peak positions indicate a  $< 1$  eV deviation from absolute.

The XAS and MCD spectra on the  $V[TCNE]_{-2}$  were collected at the Advanced Light Source (ALS) beamline 4.0.2. (BL4),<sup>49</sup> which is an undulator beamline that can produce circular polarization of opposite helicity. The degree of circular polarization,  $P_C$ , was



generally set to 0.9 rather than 1.0 (full circular), because at the higher energies (e.g. for the V L-edge) the intensity in the beam decreases rapidly as  $P_C$  increases above 0.9. The XAS spectra for the gas phase sample were collected at beamline 8.0.1. (BL8), which is an undulator beamline producing linear polarized x-rays. The undulators produce a peaked energy spectrum consisting of a fundamental and higher harmonics. At the V L-edge the 3rd harmonic was used while at the C and N K-edges the 1st harmonic was used.

The main parameters relating to the monochromator are the grating and the width of the entrance and exit slits. The grating that provides the best flux for the energy region of interest was selected for each experiment; generally one grating was used for the C and N K-edges while another was used for the V L-edge. The exit slit of the monochromator on BL8 was 50 microns, while at BL4 it was 40 microns. The energy resolution is 0.2 eV or better in both cases making these unique high-resolution studies possible.

The x-ray detector is a Si diode detector that measures photocurrent and is extremely linear over a very large dynamic range, allowing for excellent quantitative measurements. Incident intensity,  $I_0$ , is measured upstream of the sample which is a Au-coated mesh through which the x-ray beam passes at both beamlines. The photocurrent from these detectors is passed through Keithley 428 current amplifiers that are also very linear over a large dynamic range of input yielding an output voltage that is proportional to the input photocurrent.

The chamber pressure for the V[TCNE]<sub>2</sub> films was generally in the range of  $10^{-7}$  to  $10^{-9}$  Torr. The gas phase measurements of TCNE<sup>0</sup> were made by slowing the chamber pumping and allowing the pressure to rise to  $\sim 6 \times 10^{-3}$  Torr. The path length through the

gas phase sample was  $\sim 2$  m defined by a semitransparent Al film window at one end of the chamber and the Si diode at the other end of the chamber.

The XAS data presented are the sum of the + and – circularly polarized absorption data and the MCD is the difference. The intensity of each data set is plotted as the optical density,  $\mu t$ . This is obtained by normalizing the spectrum collected with the sample in place by  $I_0$  then normalizing the spectrum collected with no sample in place by  $I_0$ . The transmitted intensity,  $T$ , is then  $\frac{I_{sample}/I_0}{I_{no sample}/I_0}$  and  $\mu t = -\ln T$ . Spectra are then normalized

to between 0 below the absorption edge to 1 above the edge. This practice effectively isolates the resonant (main line) absorption from all other absorptions in the sample.

### **3.5 Organic Field Effect Transistor Fabrication and Testing**

Due to the oxygen and water sensitivity of the materials used in fabricating the organic field-effect transistors (OFET) used in this study all deposition, spin-coating, etc. steps were carried out in a Vacuum Atmospheres Co. Dri-Lab glove box atmosphere with an Ar or N<sub>2</sub> environment with less than 1 ppm O<sub>2</sub> and less than 1 ppm H<sub>2</sub>O content. In addition, very small particulate matter can wreak havoc on thin film devices. Particles as small as 0.5  $\mu m$  are nearly as thick as the entire layered structure of the devices fabricated in this work. Because of this the substrate cleaning facilities and glove box systems are located in a Class 1000 clean room to cut down on particulate contamination.

Microscope slides were cut into  $\sim 1 cm^2$  pieces to serve as the substrate for the OFETs. Typical surface roughness of these substrates was less than 5 nm. Due to the thin film structure of the devices it is imperative that all surface contaminants be removed from the substrates prior to deposition to prevent shorting of the device. This was accomplished

using a variant of an electronics industry standard cleaning procedure originally developed by Werner Kern of the Radio Corporation of America in 1965. The method used here consisted of ultrasonication of the substrates in 1)  $\text{K}_2\text{CO}_3$  solution (5 min), 2) Alconox detergent (10 min), 3) 1:1:5  $\text{H}_2\text{O}_2\text{:NH}_4\text{OH:H}_2\text{O}$  solution (10 min), 4) DI  $\text{H}_2\text{O}$  (10 min), 5) methanol (5 min), and 6) acetone (5 min). All steps were carried out at room temperature except step 3 which was carried out at 50°C. Each substrate was rinsed with the subsequent solution prior to the next step. Substrates were immediately introduced into the glove box for subsequent fabrication steps.

Aluminum gate electrodes were thermally deposited via a filament source using a tungsten boat. Typical gate electrode thickness was 100 nm. The bilayer gate dielectric was formed from silicon nitride,  $\text{Si}_3\text{N}_4$ , and PMMA.  $\text{Si}_3\text{N}_4$  was deposited via magnetron sputtering at a rate of  $\sim 0.02$  nm/s. The sputtering gases used were 99.998% pure Ar and 99.998% pure  $\text{N}_2$  in a ratio of 1:1 with a total sputtering pressure of 15-20 mTorr. The substrates were held at a constant temperature of approximately 17 °C on a rotating work holder to ensure uniform deposition. The second layer of the bilayer gate dielectric, PMMA, was spin coated in an  $\text{N}_2$  glove box atmosphere. The 5 wt% PMMA in chlorobenzene solution was pipetted onto the substrates until the entire surface was covered and allowed to stand for  $\sim 10$  s before spinning. The substrates were then spun at 3000-4000 rpm for 30s following a ramp to full speed over 5 seconds. Once coated the substrates were removed and placed on a hot plate at 120 °C for 2 minutes at atmospheric pressure to anneal the polymer layer and drive off excess solvent.

Once the bilayer gate dielectric was formed the substrates were placed in a deposition chamber for gold source/drain electrode deposition. Each substrate was masked with

aluminum wire to form a gap between electrodes. A thin layer,  $\sim 7.5$  nm, of aluminum, 99.99%, was deposited preceding the gold to prevent the gold from penetrating the soft PMMA layer and prevent diffusion of the gold through the dielectric materials. The gold contact pads were typically  $\sim 30$  nm thick. Depositions were carried out using filament sources and tungsten boats at a pressure of  $< 2 \times 10^{-6}$  Torr. A typical substrate with up to four devices is shown in Fig. 3.5. Each pair of gold contact pads constitutes one device. Active channel lengths (distance between source and drain contacts) varied from 25 to 40  $\mu\text{m}$  with channel widths (width of source/drain contacts) of 760  $\mu\text{m}$  and channel depths (source-drain electrode thickness) of 30 nm.

Electrical contact to the individual devices was made using pressed indium (In) contacts where a small “dot” of In metal is pressed onto the gold contact pads or gate electrode, an 80  $\mu\text{m}$  copper wire is then pressed into the In dot, and then another In dot is pressed onto the top of the copper wire to secure it in place. The substrates were then mounted onto a Quantum Design Physical Properties Measurement System (PPMS) sample measurement puck as shown in Fig. 3.6.

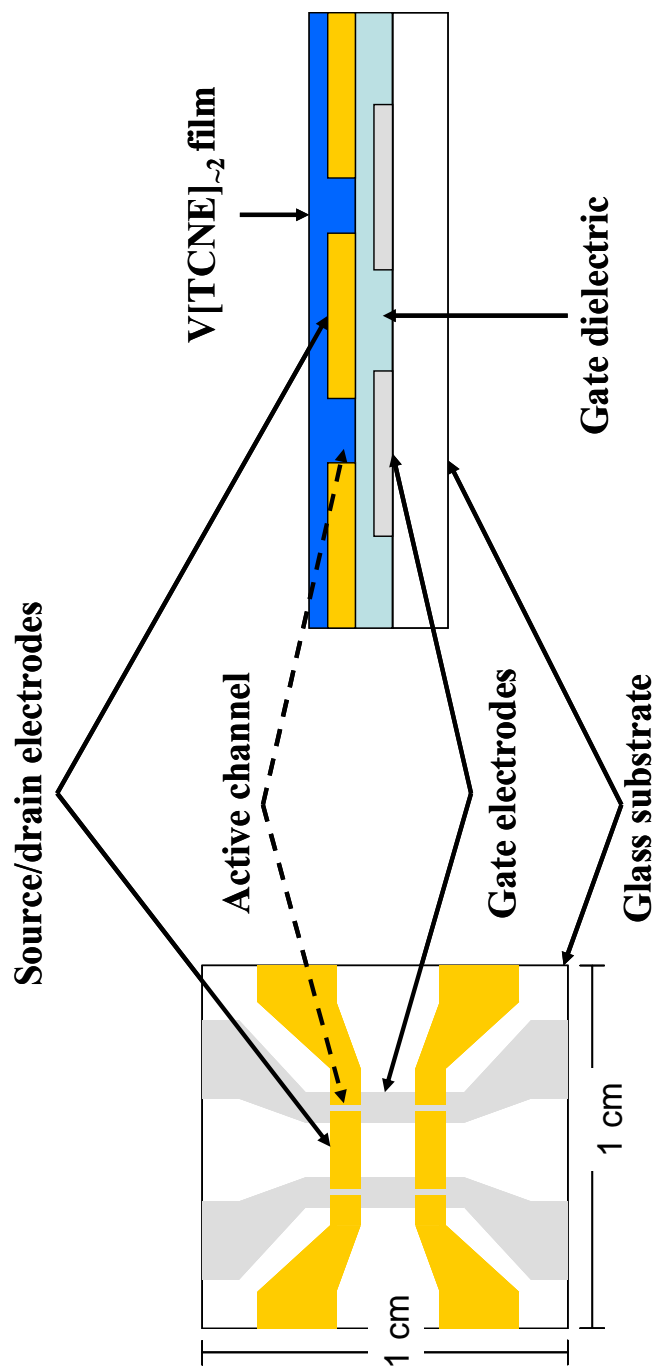


Figure 3.5. Typical OFET configuration: top view (left) and side view (right). Each substrate has up to four devices. Typical active channel lengths are 25 to 40  $\mu\text{m}$ , with channel widths of 760  $\mu\text{m}$  and channel depths of 30 nm. Al gate electrodes are 100 nm thick, gate dielectric thicknesses ranged from 300 – 500 nm, Au contacts are 30 nm thick, and the V[TCNE]<sub>2</sub> layers ranged in thickness from 200 – 500 nm.

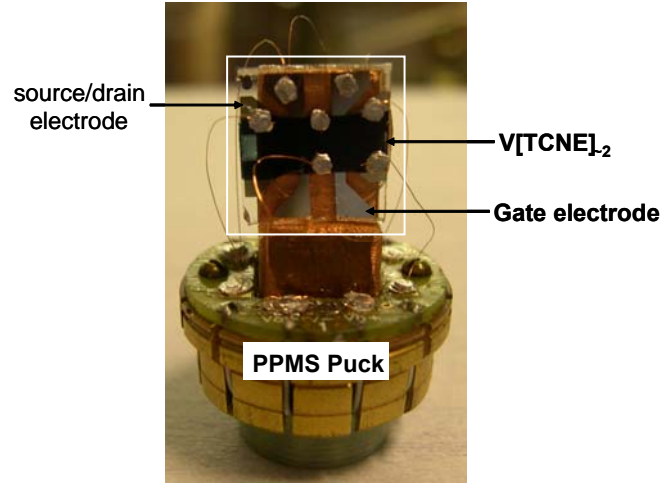


Figure 3.6. A typical OFET device wired to a PPMS puck. The substrate is outlined in the box.

The sample puck with substrate was then placed into the PPMS using a sealed transfer tool to prevent oxidation of the  $V[TCNE]_2$  prior to testing. The Physical Properties Measurement System is a variable magnetic field, variable temperature pre-wired chamber designed for automated use to make magnetoresistance and other common resistance measurements. The magnetic field can be controlled from 0 to 9 Tesla and the temperature can be controlled in the range of  $1.7 \leq T \leq 350$  K. Unfortunately, in this instance the automation of the PPMS could not be used due to the high resistance of the field-effect transistors studied. Instead the leads of the PPMS were mated with two Keithley 487 Picoammeter/Voltage sources controlled using LabView as shown in Fig. 3.7.

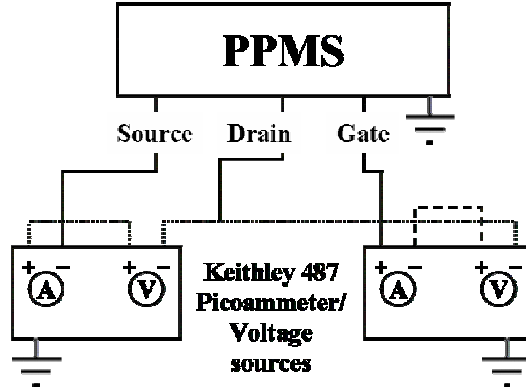


Figure 3.7. Wiring schematic for testing the  $V[TCNE]_2$  field-effect transistors. The Keithley picoammeter triaxial cable shields are grounded through the PPMS cable shield ground. The difference in the line types is not to indicate differences in the wire types used but only to indicate the connectivity of the setup.

The OFET devices were measured to collect either source-drain current ( $I_{sd}$ ) as a function of source-drain voltage ( $V_{sd}$ ), that is source-drain IV curves, at varying gate voltages; or to collect  $I_{sd}$  as a function of time with a constant  $V_{sd}$  while intermittently applying varying gate voltages. Typical plots of the raw data are shown in Fig. 3.8. IV curves were collected by first applying the maximum negative voltage, e.g. for a  $-5$  to  $+5$  V curve  $-5$  V was applied, for enough time to allow the device to equilibrate. Equilibration consisted of a steady decrease in  $I_{sd}$  over time; more will be discussed on this decrease in  $I_{sd}$  later. In cases where a gate voltage was applied the devices were allowed to run at  $V_{sd}$  with applied gate voltage for 1 minute prior to commencing data collection. For  $I_{sd}$  versus time curves the  $I_{sd}$  was also allowed to reach a steady decrease at applied  $V_{sd}$  before data collection commenced. Desired gate voltages were then applied at various time intervals.

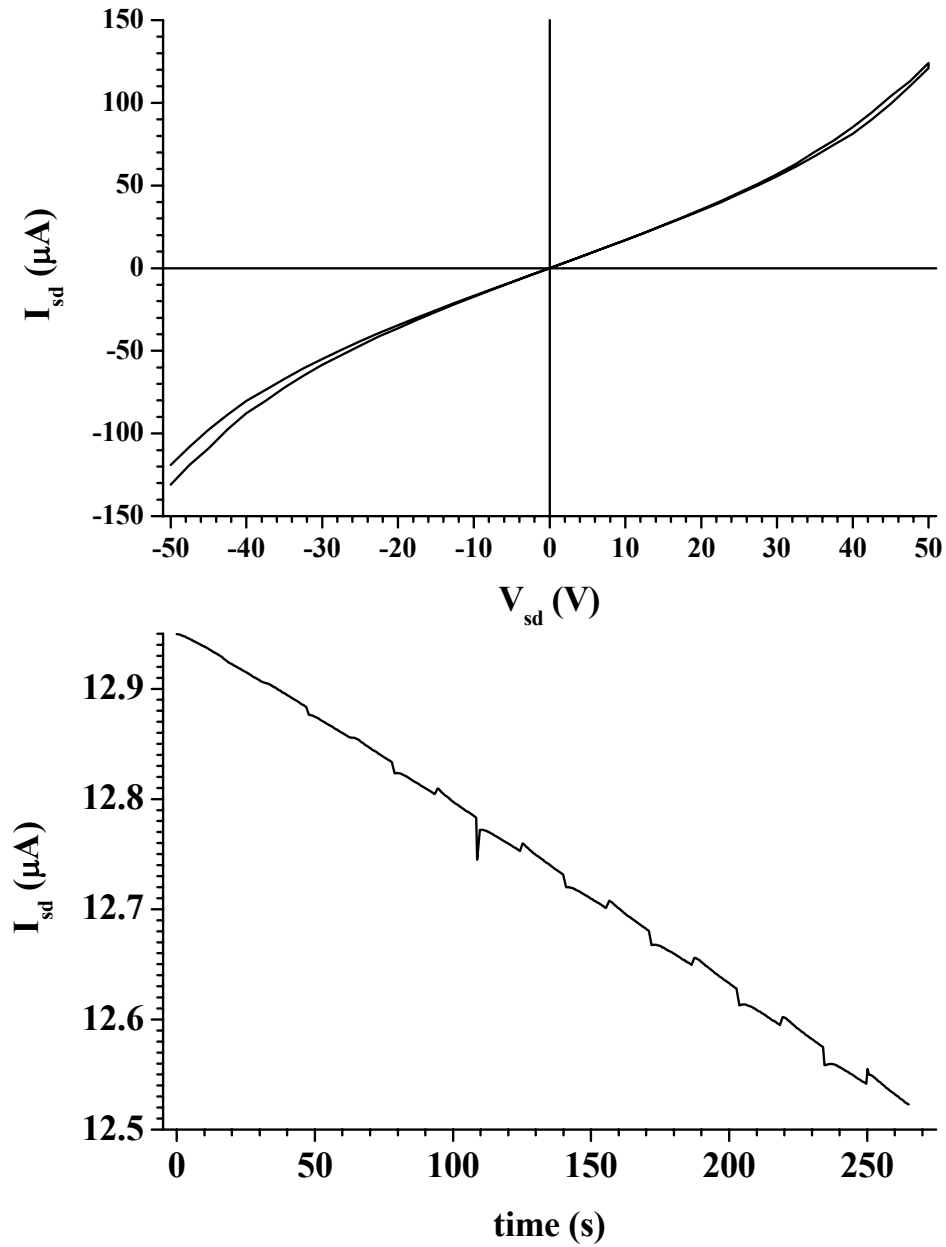


Figure 3.8. Example raw  $I_{sd}$  versus  $V_{sd}$  (top) and  $I_{sd}$  versus time (bottom) data. In the top plot the applied gate voltage is 0 V and the two curves are consecutive sweeps to determine the hysteresis. In the bottom plot  $V_{sd}$  was held constant at 5 V while the gate voltage was varied from 5 – 40 V at varying intervals which accounts for the observed drop in  $I_{sd}$ .



The IV curves consisted of two sweeps: from negative to positive voltage and back as shown in Fig. 3.8 with little hysteresis. In both cases the leakage current was recorded simultaneously with the source-drain current and will be shown where appropriate. Typical leakage currents were on the order of  $10^{-10} - 10^{-11}$  A.

In each measurement a nearly monotonic decrease in current with time was observed. In order to perform the analysis of the transistors this decreasing current profile had to be removed. To do this, data at zero applied gate voltages is collected between each interval in which a gate voltage is applied. This zero applied gate voltage data was then plotted and fitted with a straight line to determine the rate of the decrease. The slope of this line is then subtracted out of the entire data set to yield corrected data with a zero slope and then the absolute current is subtracted from this leaving only the change in source-drain current as a function of time. Subsequent calculations to determine the magnitude of the transistor effect, etc. were then carried out on this corrected data. Absolute currents could not be determined for the devices, but for the purposes of this work, the relative currents were sufficient to adequately describe the physical processes. A plot of the corrected data is shown in Fig. 3.9 along with the leakage to indicate the transistor effect is due to the field-effect on  $V[\text{TCNE}]_2$  and not due to current between the drain and gate electrodes. The potential origins of this linear decrease in current with applied voltage will be discussed later in section 5.1.

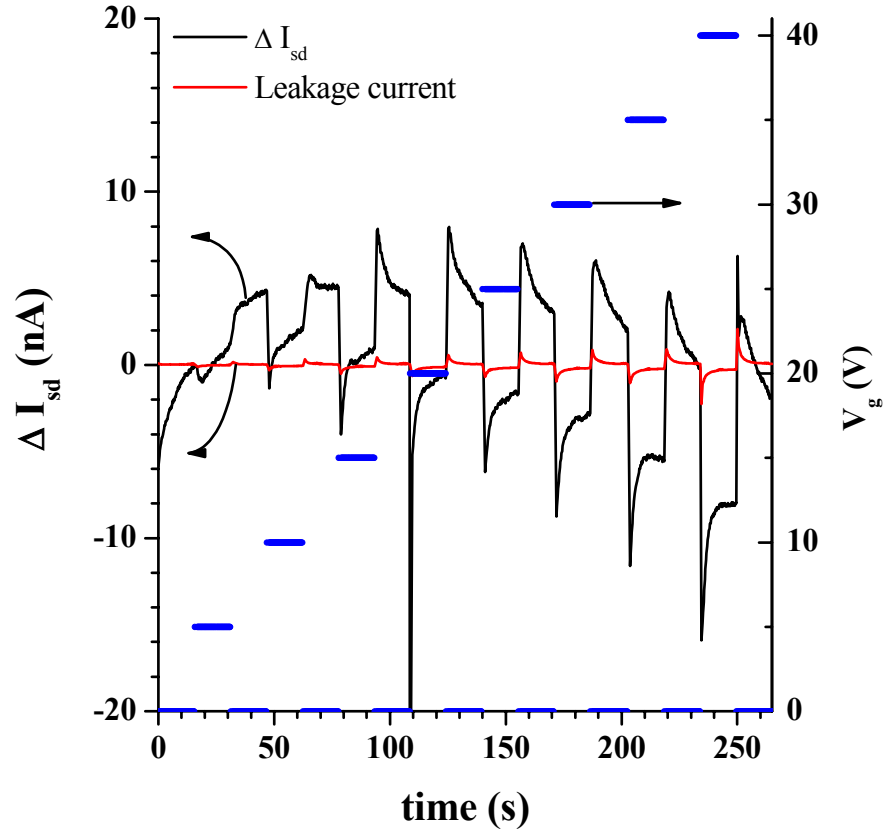


Figure 3.9. The change in source-drain current,  $\Delta I_{sd}$ , plotted as a function of time. The gate voltage is applied at different time intervals as indicated. Note the leakage current between the drain and gate electrodes is far less than the observed change in  $I_{sd}$  indicating  $\Delta I_{sd}$  is due largely to the field-effect.

## CHAPTER 4

### THE ELECTRONIC STRUCTURE OF $V[TCNE]_2$

#### 4.1 XAS and MCD Results

The first portion of this chapter is dedicated to the description of the vanadium L-edge absorption results including the associated MCD. Subsequent sections will deal with calculated fits of the XAS data using crystal field and charge transfer multiplet theory and the implication of the results there. From there the discussion will move to the organic portion of the system with a related side step to the gas phase  $TCNE^0$  XAS results in an attempt to relate the differences in the neutral spectrum to the reduced spectrum of  $[TCNE]^+$ . Finally, the discussion will turn to the interplay of the V and TCNE sub-lattices based on these findings.

##### 4.1.1 The Vanadium L-edge

A typical high-resolution vanadium L-edge XAS absorption spectrum for  $V[TCNE]_2$  is shown in Fig. 4.1. The two main features in the XAS spectrum, due to spin orbit coupling, are the  $L_3$  ( $2p_{3/2}$ ) edge and  $L_2$  ( $2p_{1/2}$ ) edge with a spin split energy of 6.2 eV, smaller than the 7.5 eV splitting energy of the  $2p$  level from x-ray photoelectron spectroscopy (XPS). This discrepancy has been shown to be a consequence of the strong interaction of the  $2p$  core-hole and the  $3d$  electrons in the final state.<sup>50</sup> The main peaks

are additionally split into two large features which arise from the  $t_{2g}$  and  $e_g$  orbitals arising from crystal field splitting of the vanadium  $3d$  orbitals in an octahedral environment. The octahedral environment of  $V[TCNE]_{-2}$  was first reported by Haskel, et al. using near edge x-ray absorption fine structure (NEXAFS) which showed the system possessed short range order with approximately six nitrogen atoms surrounding the vanadium centers in an approximately octahedral symmetry.<sup>51</sup> This will be discussed in more detail in later sections. In addition, an obvious multiplet structure in the  $L_3$  edge due to strong overlap of the  $2p$  core-holes and the  $3d$  valence electrons as well as strong  $3d$ - $3d$  electron correlations can be seen as well.

The continuum step in the data, i.e. the difference in the data which has been normalized to between 0 before the beginning of the absorption edge and 1 well beyond the absorption edge, is due to excitations of the core electron to a continuum of states. In this region the density of states becomes so high that the smooth continuum cross section is observed from  $\sim 530$  eV and higher in the vanadium L-edge. For the purpose of comparison to calculated spectra it is necessary to remove this continuum step or model these continuum states – an extraordinarily difficult task. Due to this difficulty we chose to remove the continuum step. This is accomplished using two arctan functions, one for each edge,  $L_3$  and  $L_2$ , of the form

$$I = H \left[ \frac{1}{2} + \frac{1}{\pi} \arctan \left( \frac{E - P}{\Gamma_L / 2} \right) \right] \quad (4.1)$$

where  $H$  is the height of the jump,  $P$  is the energy position of the inflection point of the jump,  $E$  is the independent energy variable, and  $\Gamma_L$  is the width of the jump.<sup>52</sup> This

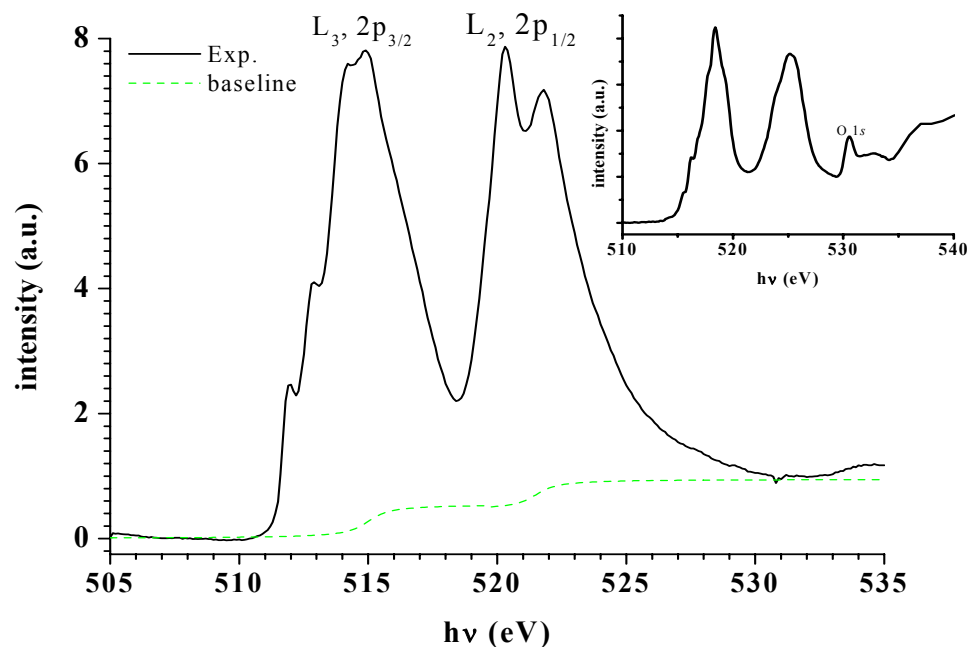


Figure 4.1. Vanadium  $L_3$  and  $L_2$  absorption edges. The spectrum was normalized between 0 intensity at the pre-edge and 1 far beyond the absorption edge. The baseline is drawn as shown using two arctan functions (one for each edge –  $L_3$  and  $L_2$ ) as described in the text. The inset shows an oxidized sample with the O  $1s$  absorption peak labeled.

assumes the shape of the step is determined by the lifetime of the core-hole where a square step is convoluted with a Lorentzian, which is appropriate given the width of the step and is typical for fitting continuum steps in transition metal ions.

The lack of oxygen, adsorbed or in the form of vanadium oxide, is indicated by the absence of the oxygen  $1s$  peak which normally appears at  $\sim 531$  eV, Fig. 4.1 inset. It should be noted that this is a key observation as there are many forms of vanadium oxides in which the vanadium centers have a variety of valences to include  $V^{2+}$ ,  $V^{3+}$ ,  $V^{4+}$ , and  $V^{5+}$ . The discussion henceforth will then focus on what is referred to as a “clean” film indicating that there are few oxides formed and the vast majority of the signal arises from

V in a TCNE rather than an oxygen environment. Previously reported chemical analysis via x-ray photoelectron spectroscopy (XPS) studies show the vanadium centers in  $V[TCNE]_{-2}$  are predominantly in the V(II) or  $V^{2+}$  configuration but have a significant contribution from higher valence states.<sup>15,59</sup> It should be noted that surface oxidation of the films was evident and could potentially have led to a significant proportion of signal for vanadium in the higher valence states. This point will be addressed in more detail later.

The magnetic circular dichroism (MCD) technique probes the element specific spin density of states. The signal is obtained from the difference between left (+) and right (−) circularly polarized x-rays, and a nonzero MCD signal will be observed only in systems displaying magnetism. The nonzero MCD signal for vanadium in  $V[TCNE]_{-2}$  is shown together with its associated XAS spectrum in Fig. 4.2 indicating the vanadium possesses a magnetic moment. There are two positive-going features in the MCD at the low energy side of the  $L_3$  edge at 511.8 and 512.6 eV each with an associated multiplet XAS peak. The next highest energy peak is associated with the  $t_{2g}$  peak of the XAS and the next with the  $e_g$  XAS peak. The  $L_2$  edge portion of the MCD signal has a similar structure to that of the  $L_3$  edge with a positive-going peak associated with the  $t_{2g}$  XAS peak and a negative-going peak associated with the  $e_g$  peak. There is also a broad negative-going feature centered at 517.1 eV between the two main peaks with intensity on the order of the other negative-going features and a low intensity feature centered at 524.6 eV on the high energy side of the  $L_2$  edge. Neither of these peaks has an immediately apparent associated XAS feature. The origin of these peaks in particular will be discussed in more detail in later sections.

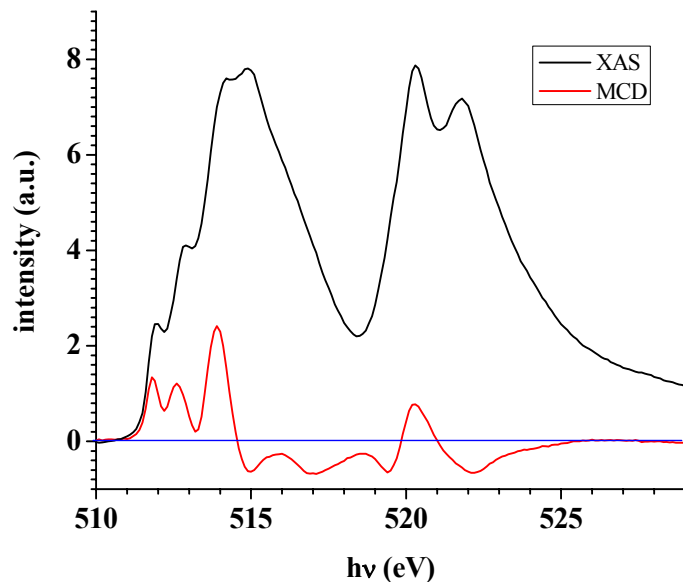


Figure 4.2. Experimental magnetic circular dichroism (MCD) signal with associated XAS for the vanadium L-edge in  $V[TCNE]_{-2}$ . The XAS spectrum has been normalized to between 0 (pre-edge) to 1 (well above absorption edge). The MCD spectra is as recorded with no normalization, background subtraction, or scaling.

#### 4.1.1.1 Crystal Field Multiplet Calculations

X-ray absorption of transition metal centers yields strongly interacting  $2p$  core-holes and  $3d$  valence electrons; it is therefore assumed the final states remain largely localized on the metal centers and can be treated using atomic multiplet theory. In addition, it has been shown that the multiplet effects in  $3d$  systems dominate all other interactions making this a prudent approach to modeling the experimental data.<sup>53</sup> The pure atomic multiplet approximation does a poor job of estimating the experimental XAS spectra of condensed phase materials because, while the  $2p$  states remain strongly localized on the metal centers, the  $3d$  valence states can in fact become part of an extended electronic

structure. A first approach in modeling this extended electronic structure is to consider the crystal field induced by the ligands via crystal field multiplet (CFM) theory. In this case, the nature of the ligands is not specified but the strength of the field they create surrounding the metal center is parameterized to fit the experimental spectrum. This strength of the crystal field,  $10Dq$ , is an important parameter in determining the transition between high-spin and low-spin states in  $d$ -configurations in which an additional electron may be added to the  $t_{2g}$  or the  $e_g$  orbitals. Fig. 4.3 depicts the effect on the  $d$ -orbitals under the influence of an octahedral crystal field and the splitting energy  $10Dq$ . The electron will, of course, go into the orbital that yields the lowest total energy state, e.g. if the pairing energy of placing another electron in a half-full  $t_{2g}$  orbital is greater than placing that electron in a higher energy  $e_g$  orbital it will choose the latter and vice versa. This is especially important in  $d^3$  and higher configurations. Here, considering the  $2p^6 3d^3 \rightarrow 2p^5 3d^4$  transition in x-ray absorption of  $V[TCNE]_2$ ,  $10Dq$  is an important parameter in describing the XAS spectrum.

Fig. 4.4 shows the results from CFM calculations which include the effects on the absorption spectrum of  $V^{2+}$  induced by a simulated cubic (octahedral) crystal field that mimics the field the surrounding  $[TCNE]^+$  ligands. In this case the crystal field strength is varied from  $-3.0$  eV to  $3.0$  eV. Negative crystal field strengths invert the order of the  $t_{2g}$  and  $e_g$  states, i.e.  $e_g$  states are lower in energy than  $t_{2g}$  states. The case of  $0.0$  eV corresponds to the pure atomic multiplet case in which there is no crystal field but  $2p$ - $3d$  (core-hole) and  $3d$ - $3d$  interactions are considered. The  $L_3$  and  $L_2$  edges display much different behavior which is indicative of the spectral weight transfer induced by the multiplet effects. The



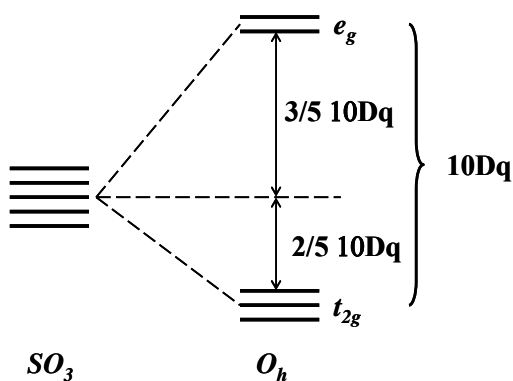


Figure 4.3. The crystal field splitting of the five  $d$ -orbitals under the influence of an octahedral crystal field. Left – the five degenerate  $d$ -orbitals in a spherical field. Right – the five orbitals split in energy due to the interaction with an octahedral field where the interaction is greater with the  $e_g$  orbitals, hence the higher energy. Note: the average energy of the orbitals does not change upon application of the crystal field.

$L_2$  edge spectra increasing from  $10Dq = 0.0$  eV to 3.0 eV clearly show the effect of the strength of the crystal field on the spectrum. The two peaks in this edge, the  $t_{2g}$  (lower energy) and the  $e_g$  (higher energy), are more clearly observed because the spectral weight transfer is much smaller in this edge than for the  $L_3$  edge. As the crystal field strength is increased the intensity of the peaks evolves from 3:2 intensity ratio (0.0 eV) where the core excited electron is more likely to populate the  $t_{2g}$  than the  $e_g$  to much more intense for  $t_{2g}$  than for  $e_g$  indicating that the pairing energy is lower than  $10Dq$  and it is more energetically favorable for the electron to populate the  $t_{2g}$  orbitals than the  $e_g$  orbitals. Reversing the direction of the crystal field (negative  $10Dq$  values) works to eliminate the distinction between the  $t_{2g}$  and  $e_g$  orbitals as can be seen in the figure. Given previous results indicating that the V centers are in a +2 valence state donating charge to the TCNE moieties, the negative values of crystal field splitting strength do not make

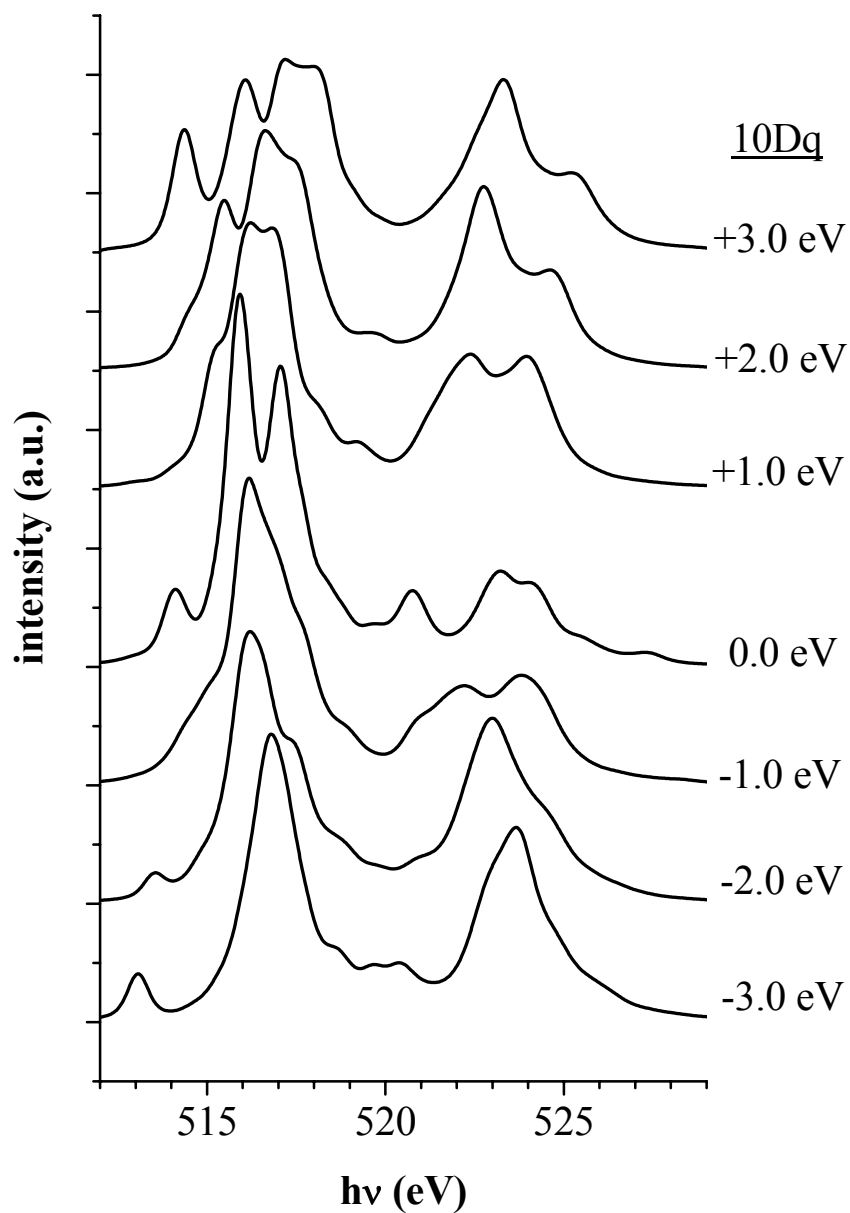


Figure 4.4. Calculated vanadium XAS spectra including the  $V^{2+}$   $L_3$  and  $L_2$  edges from crystal field multiplet theory. The crystal field splitting strength,  $10Dq$ , is varied from  $-3.0$  eV to  $3.0$  eV as shown on the right. In each case the calculations are done with a pure  $d^3$  configuration ( $V^{2+}$ ). The  $0.0$  eV case corresponds to the pure atomic multiplet case with no applied crystal field but still takes into account the  $2p$ - $3d$  core-hole potential and  $3d$ - $3d$  electron repulsion interactions.

physical sense since no reversal of the crystal field is assumed to take place in this case. Therefore, they will not be considered further as a possibility. Considering the  $L_3$  edge any trends are less conspicuous reflecting the strong effect multiplets have on the  $L_3$  edge. It appears that the multiplet feature at  $\sim 514$  eV for  $10Dq = 0.0$  eV appears to merge with the main feature as  $10Dq$  is increased but seems to reemerge at  $10Dq = 3.0$  eV. Most notably the features due to the transitions to the  $t_{2g}$  and  $e_g$  orbitals seem to be even in intensity and merge together again indicating an equal probability of populating these two orbitals, i.e. pairing energy  $\sim$  crystal field splitting strength.

This is a direct observation of the influence the multiplet structure has on the  $L_3$  to  $L_2$  branching ratio, the ratio of intensity of the  $L_3$  to  $L_2$  edge. In an ideal spectrum using the single-particle approach one would expect to observe four peaks with intensity ratios of 6:4:3:2 for  $L_3 t_{2g}$ ,  $L_3 e_g$ ,  $L_2 t_{2g}$  and  $L_2 e_g$  peaks, respectively. However, once the Slater-Condon parameters are introduced, as is the case with the multiplet approach, the effect is to reduce the intensity of the  $t_{2g}$  peaks and shift it to the  $e_g$  peaks and introduce pre-edge features because more transitions are allowed.<sup>54</sup> In addition, the multiplet effect is more pronounced for the  $L_3$  edge than the  $L_2$  edge where the single-particle approach remains a good approximation.

With this in mind a crystal field splitting strength of +2.4 eV gives the best qualitative fit to the experimental data as shown in Fig. 4.5. This is agreement with other reports on the vanadium L-edge spectrum in  $V[TCNE]_2$  modeled using CFM.<sup>55</sup> The crystal field strength value of 2.4 eV is approximately at the high-spin low-spin transition for centers with a  $3d^4$  configuration. This is evident by comparing the intensity of the two largest peaks within each absorption edge which are nearly equal in the  $L_3$  edge in both the

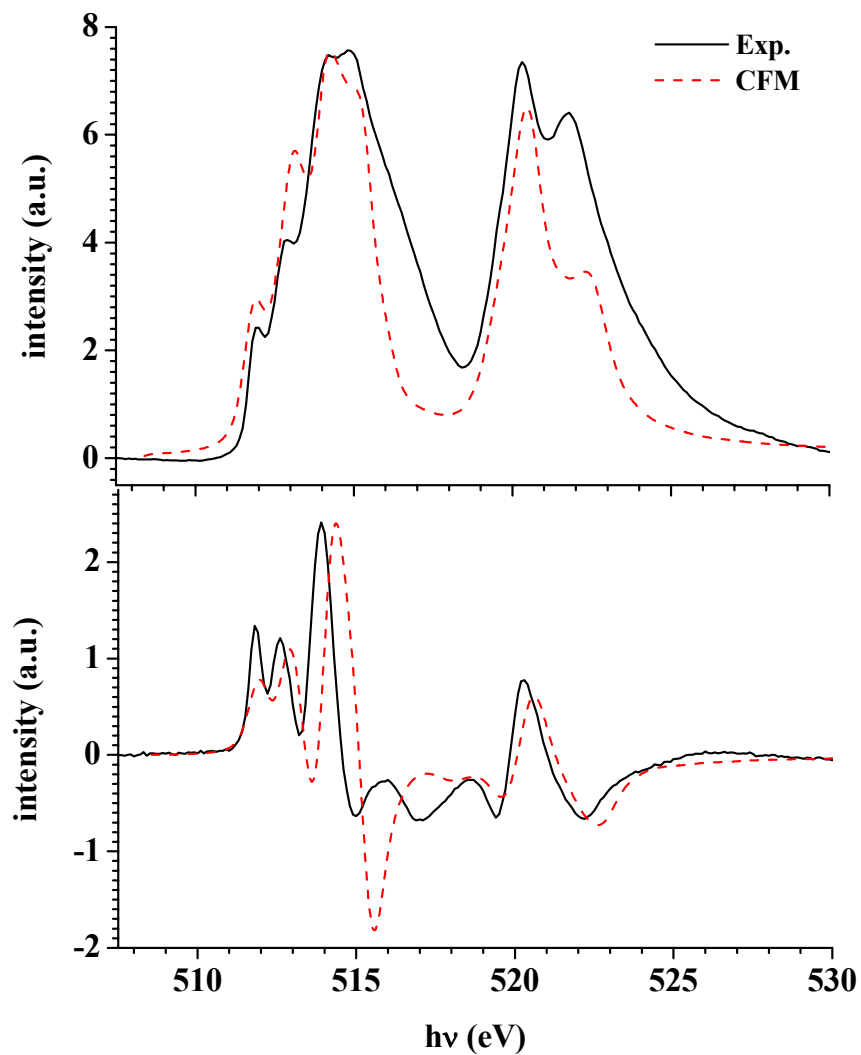


Figure 4.5. Comparison of the vanadium XAS (top) and MCD (bottom) experimental spectra and calculated spectra from crystal field multiplet (CFM) theory. The energy scales of the calculated spectra were adjusted by 0.45 eV and the intensity multiplied by a factor of 33 for comparison to the experimental data. The continuum step has been removed from the experimental XAS spectrum as described in the text. The MCD spectrum is plotted as recorded.

experimental and calculated spectra; however, the  $t_{2g}$  is largely favored in the  $L_2$  edge of the calculated spectrum and only slightly favored for the experimental spectrum. Another item of note is the “missing” intensity for the calculated spectrum on the high side of each absorption edge ( $\sim 517$  eV for  $L_3$  and  $\sim 524$  eV for  $L_2$ ), or rather the experimental spectrum has an excess intensity in these regions. This is the area normally associated with charge transfer satellites and will be discussed in more detail in the next and later sections as it may be a key result in describing the interactions between V and TCNE.

The MCD spectrum calculated via CFM theory is also shown in comparison to the experiment MCD spectrum in Fig. 4.5. Again, the calculated MCD spectrum qualitatively reproduces most of the features from the experimental spectrum with a noticeable energy shift of about 0.3 – 0.6 eV. An intriguing result is that the CFM calculation does not reproduce even qualitatively the feature associated with the excess intensity in the experimental XAS spectrum at 517.1 eV. While the CFM calculations do not account for this excess intensity and also do not show an associated MCD feature for it, the experimental MCD spectrum clearly indicates that this excess intensity does indeed have an associated polarization with it.

#### **4.1.1.2 Charge Transfer Multiplet Calculations**

In an attempt to find the source of the missing intensity observed in the experimental spectrum that cannot be accounted for using the crystal field multiplet model charge transfer multiplet (CTM) calculations were carried out. The CTM model uses configuration interactions in the ground and final states to model the XAS process. In this manner CTM calculations simulate the effects of the XAS absorption process on the

transition metal centers as if there were covalent interactions or strong hybridization effects present with the ligands leading to bonding and antibonding orbitals. The density of states of the antibonding orbitals is then probed by XAS and typically appears on the high energy side of the absorption edge where the excess intensity for the experimental XAS spectrum is observed.

The CTM model allows one to add more configurations to the ground state of the system,  $3d^3$  in the case of  $V[TCNE]_{-2}$ . These additional configurations come in the way ligand holes or charge transfer from the ligands to the metal centers. In the simplest case the ground state configuration of  $V[TCNE]_{-2}$  becomes  $3d^3 + 3d^4 \underline{L}$ , where  $\underline{L}$  is the ligand hole. For a typical transition metal oxide, the ligand hole is modeled as the result of moving an electron from the  $2p$  band of oxygen to the  $nd$  band of the transition metal, i.e. charge transfer from the ligand to the metal. In the case of  $V[TCNE]_{-2}$  the ligand hole picture may be slightly more complicated in that the result is not as simple as moving an electron from the  $2p$  band of the nitrogen to the  $3d$  band of the vanadium because of the molecular orbitals involved with the  $[TCNE]^-$  sub-lattice. This brings this discussion to a very important point: the CTM calculations make no distinction and require no knowledge or input concerning the type of ligand coordinated with the transition metal center. The calculation merely models the amount of decrease in  $d$ -character of the final states based upon the parameterization fitting of the experimental data. This point will be discussed further in later sections, but it is worth noting here to save the reader from confusion as to where the ligand hole originates as far as the calculations are concerned.

A CTM calculated spectrum using the ground state configuration  $3d^3 + 3d^4 \underline{L}$  and excited state configuration  $2p^5 3d^4 + 2p^5 3d^5 \underline{L}$  is shown compared to an experimental

spectrum in Fig. 4.6. The 10Dq value found in the CFM calculations, 2.4 eV, was used here. In addition, for this calculation, the charge transfer energy,  $\Delta$ , is set to 1.0 eV for optimization. The charge transfer energy is the energy difference between the two configurations in the ground state,  $3d^3$  and  $3d^4 \underline{L}$ . The final state charge transfer energy,  $\Delta'$ , is given formally as  $\Delta' = \Delta + U_{dd} - U_{pd}$ , where  $U_{pd}$  is the core-hole potential and  $U_{dd}$  is the  $3d$ - $3d$  electron correlation energy. The core-hole potential is typically 1 – 2 eV larger than the  $3d$ - $3d$  electron correlation energy, so with  $\Delta = 1.0$  eV the final state charge transfer energy is  $\sim 0$  eV and is set as such for the calculation. The final parameter that needs to be considered is the transfer integral,  $T$ , for the  $t_{2g}$  and  $e_g$  orbitals. The transfer integral describes the coupling between the localized states to the valence band. Given the symmetries of the  $t_{2g}$  and  $e_g$  orbitals it is expected that the transfer integral, or rather the ratio of their transfer integrals  $T_{e_g}/T_{t_{2g}}$ , will change based upon the nature of the interaction between the metal and the ligand. In the case of  $\sigma$ -bonding the transfer integral ratio would be expected to be larger given that the  $e_g$  orbitals are directed toward the ligands, but the opposite would be the case for  $\pi$ -bonding interactions where the  $t_{2g}$  orbitals would have the greatest interaction with the  $p$ -orbitals of the ligand. The former is typically the case for transition metals oxides and a ratio of  $\sim 2$  is typically used.<sup>56</sup> For V[TCNE]<sub>2</sub> the latter is expected to be the case and  $T_{e_g}/T_{t_{2g}}$  should be  $< 1$ . This turns out to be the case in calculating the spectrum in Fig. 4.6 as a  $T_{e_g}/T_{t_{2g}}$  ratio of 0.79 gives the best qualitative fit indicating charge transfer between the  $t_{2g}$  orbitals of vanadium and, for example, the  $p_z$  ( $t_{1u}$ ) orbitals of nitrogen. Once again, however, it should be noted that

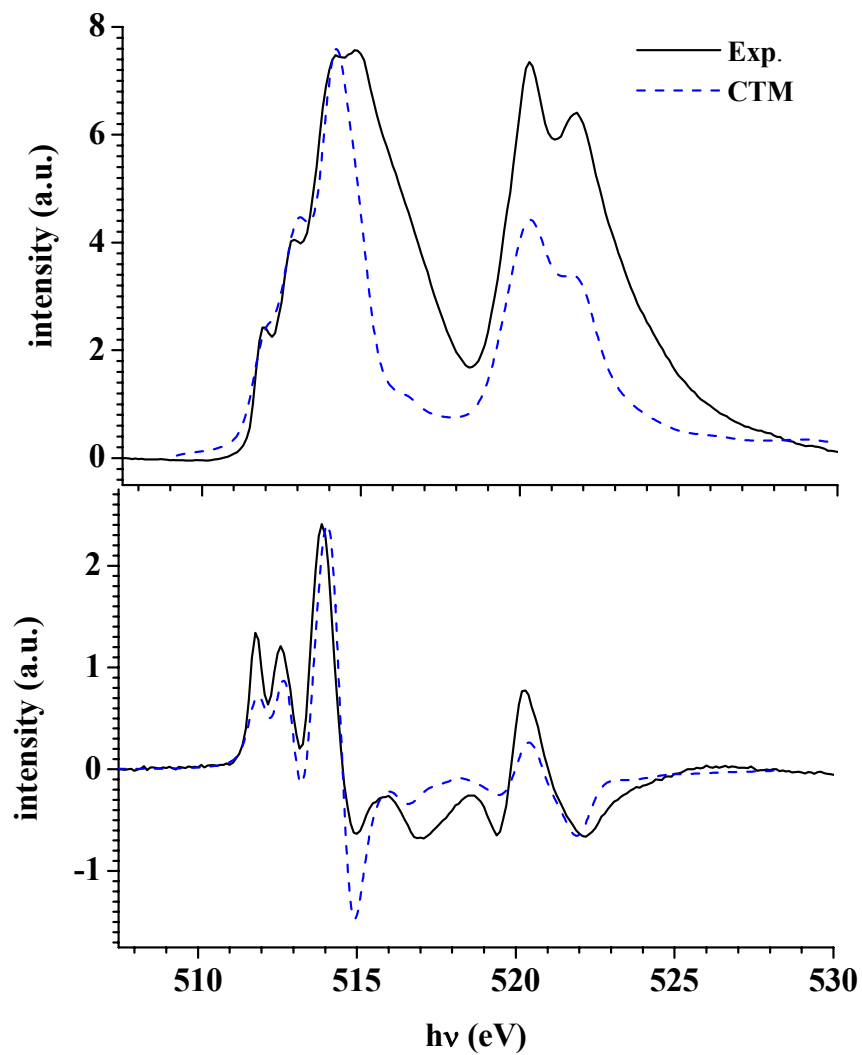


Figure 4.6. Comparison of the experimental XAS (top) and MCD (bottom) spectra with that calculated from charge transfer multiplet (CTM) theory. The continuum step has been removed from the experimental spectrum as described in the text. The energy scale of the calculated spectrum was adjusted by -1.8 eV and intensity scaled by 28 for comparison to the experimental data.



the interaction is most likely much more complicated than this because of the molecular orbital structure involved with the TCNE sub-lattice.

As can be seen from the figure, the CTM calculated provides a good qualitative fit at least for the low energy sides of the two absorption edges. Immediately apparent is the effect the charge transfer multiplet calculations have on narrowing the features of the spectrum. This narrowing is in fact a contraction of the multiplet structure of the spectrum, which is typically the case for smaller values of the charge transfer energy,  $\Delta$ . However, larger values of  $\Delta$  produce poorer quality fits of the experimental data and do not account for the excess intensity on the high energy side of the two absorption edges. Despite the less than perfect fit for the CTM XAS, the MCD spectrum does seem to qualitatively reproduce the broad MCD feature in the experimental MCD spectrum at 517.1 eV as shown in Fig. 4.6. This indicates some degree of decrease in the *d*-character of the vanadium spectrum with an associated polarization.

We note that the CTM calculation produces a poorer fit in comparison to the CFM calculation. Previous studies of CTM modeling of the vanadium L-edge spectrum report similar results and attribute the qualitative fit of the CTM model as hybridization between the V and TCNE sub-lattices. Due to the poorer fit of the CTM model versus the CFM model and the nature of the CTM theory calculations, we feel we cannot make this conclusion without clearer evidence of hybridization. The region of the excess intensity in the experimental spectrum may provide a clearer picture of the interaction between V and TCNE.

#### 4.1.1.3 Origin of the Excess Intensity in the Experimental XAS Spectrum

As calculated, neither the crystal field nor charge transfer multiplet theory calculations have managed to account for the excess intensity observed on the high energy side of the two experimental XAS absorption edges for the vanadium L-edge. This section details the exploration of various potential sources of this excess intensity. The first of these explorations deals with a broader look at the V[TCNE]<sub>2</sub> system.

The symmetry of the final states play an important part in the X-ray absorption process as described in the background section. The specific symmetries of the final states offer a look at how the interactions are modeled and may provide clues to the origin of the excess intensity in the experimental spectrum. We can resolve the final state symmetries of the XAS absorption spectra to determine the respective contributions. To accomplish this, the CFM spectrum, having the better fit of the two calculated spectra, will be used. From the results of the CFM calculation it was determined that there are three symmetries contributing to the final state absorption spectrum as shown in Fig. 4.7:  $A_1$ ,  $A_2$ , and  $T_1$ . As expected the largest contribution to the modeled final state absorption is from the  $T_1$  state which is consistent with the CTM calculations discussed earlier with interaction between the  $t_{2g}$  states of the vanadium and the  $t_{1u}$  states of nitrogen. However, as mentioned the interaction between the two is much more complicated than this simple picture and it is not immediately apparent that changing either the mix or the relative contributions of these three symmetry states will model the excess intensity in the experimental spectrum. In addition, it is not clear that changing the mix or the relative

contributions of these symmetries makes sense from a physical standpoint as the nature of the bonding and coordination would change if this were the case.

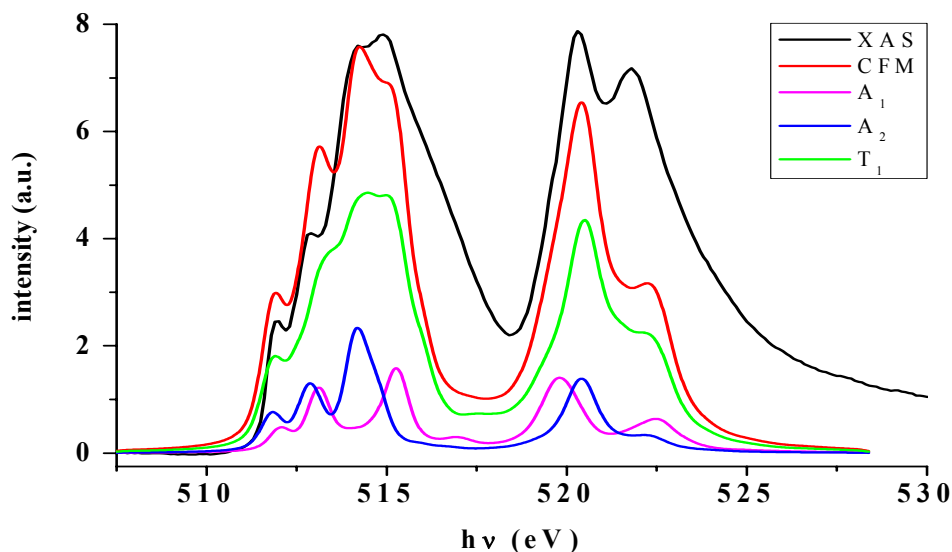


Figure 4.7. The experimental V L-edge spectrum with its associated CFM calculated spectrum and its three resolved symmetry states contributing intensity.  $A_1$ ,  $A_2$ , and  $T_1$  are symmetry representations in  $O_h$ .

As mentioned earlier  $V[TCNE]_{-2}$  has a slightly distorted octahedral coordination environment between the  $V^{2+}$  and  $[TCNE]^{-}$  with  $\sim 6$  nitrogen atoms surrounding the metal center. The calculations performed thus far have assumed perfect octahedral coordination. At this level of calculation is it not possible to mimic a “slightly distorted” octahedral environment, but it is possible to lower the symmetry of the system and perform the calculation to determine if the results give any clues as to the origin of the excess intensity. Fig. 4.8 shows the results of CFM calculations lowering the symmetry to  $D_{4h}$ , i.e. four N atoms coordinated to a V center in a plane at  $90^\circ$  angles to each other.

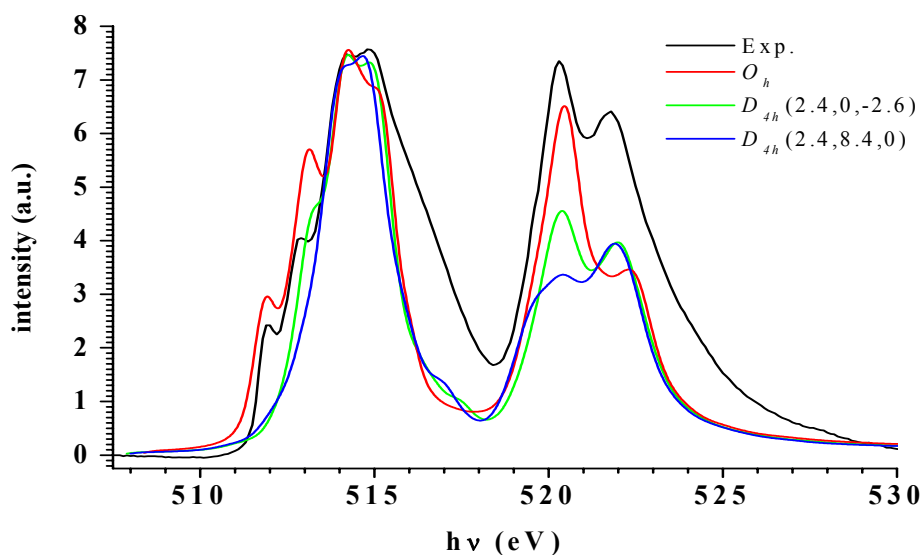


Figure 4.8. Crystal field multiplet calculations in  $D_{4h}$  symmetry compared to  $O_h$  symmetry and experiment. The three values in parentheses are the three crystal field operators in  $D_{4h}$  10Dq, Ds, and Dt.

Again, the calculated spectra fail to reproduce any of the excess intensity or enhance the fit of the experimental spectrum. The parameter space for this particular calculation is quite large in that there are three parameters (10Dq, Ds, and Dt) that can be adjusted to manipulate the fit. For example, a fit better than the ones shown can be realized with a 10Dq of  $-5.2$ , but as discussed earlier this does not agree with the physical characteristics of the system and charge transfer involved between the vanadium and the TCNE. Another indicator that the system is not in a lower symmetry state is the lack of a pre-edge feature due to  $1s$  to  $3d$  transitions which are symmetry forbidden in other  $V^{II}$  and  $V^{III}$  octahedral complexes but are partially allowed in square pyramidal ( $C_{4v}$ )  $V^{IV}$  complexes.<sup>57</sup>

Considering the charge transfer multiplet theory calculations two configurations are typically sufficient to adequately model a transition metal XAS spectrum such as with  $V^{2+}$ ; however, this is not always the case and more configurations may be required, especially in the case of higher formal valence states.<sup>58</sup> Fig. 4.9 shows the results from CTM calculations in which three configurations are used to model the vanadium XAS spectrum. One spectrum is calculated using the three configurations  $3d^3$ ,  $3d^4\bar{L}$  and  $3d^5\bar{L}^2$  in which the first configuration is  $V^{2+}$ , the second with one electron transferred from a ligand  $2p$  orbital to the V  $3d$  level (one ligand hole), and the final with 2 electrons transferred from the ligands to the V  $3d$  level (two ligand holes). The final states are the familiar  $2p^53d^4$ ,  $2p^53d^5\bar{L}$  and  $2p^53d^6\bar{L}^2$ , respectively. The second spectrum is calculated using the three configurations  $3d^2$ ,  $3d^3\bar{L}$  and  $3d^4\bar{L}^2$  with final states  $2p^53d^3$ ,  $2p^53d^4\bar{L}$  and  $2p^53d^5\bar{L}^2$ , respectively, with  $3d^2$  being  $V^{3+}$ . As is often the case with more than two configurations the multiplet structure of the spectrum is lost as features are contracted into the main peaks. In addition the calculated spectra still show no indication that more configurations will enhance the fit to the experimental spectrum in the region of the excess intensity. However, the  $V^{3+}$  spectrum is shifted to higher binding energies as expected and the overall fit is quite poor; however,  $V^{3+}$  calculated spectrum displays intensity in the energy region of the excess intensity observed in the experimental spectrum especially in the case of the  $L_2$  edge where the shape of the intensity is even compelling. While it is clear that additional configurations in the CTM calculation do not clearly point to the source of the excess intensity in the experimental spectrum, contributions from  $V^{3+}$  species still cannot be definitively ruled out.

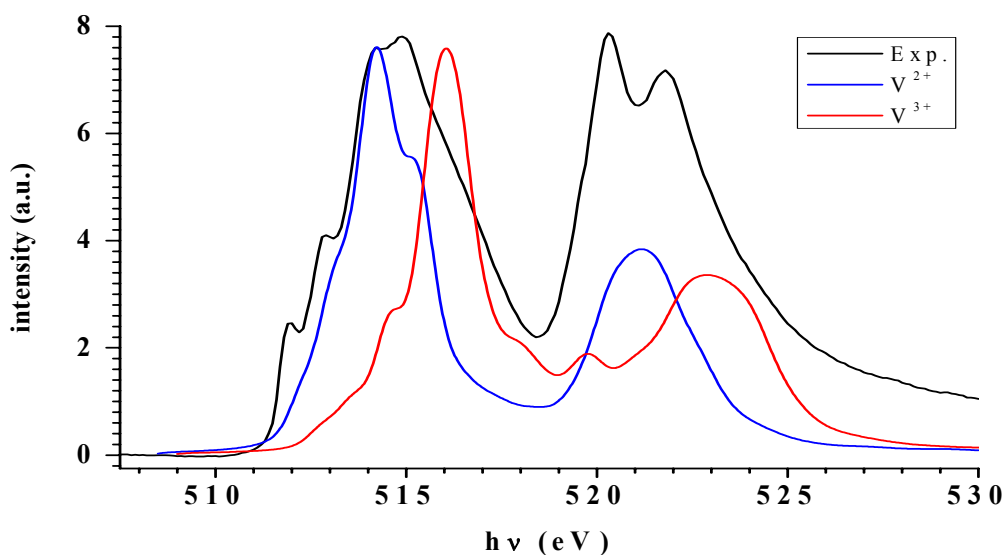


Figure 4.9. Charge transfer multiplet calculated spectra calculated using the three ground state configurations  $3d^3$ ,  $3d^4\bar{L}$  and  $3d^5\bar{L}^2$  (spectrum labeled  $V^{2+}$ ) and the three ground state configurations  $3d^2$ ,  $3d^3\bar{L}$  and  $3d^4\bar{L}^2$  (spectrum labeled  $V^{3+}$ ). The experimental spectrum is normalized between 0 (pre-edge) and 1 (well above the absorption edge). The intensities of the calculated charge transfer spectra have been scaled by a factor of 14.3 and the energy scales shifted by -1.5 for comparison to the experimental spectrum.

Reports that show that the vanadium is largely present as  $V^{2+}$  in  $V[TCNE]_{\sim 2}$ , but there is also a significant contribution from vanadium in higher valence states. Chemical analysis of the surface of  $V[TCNE]_{\sim 2}$  films show that the system is slightly TCNE rich with a N:V ratio of 9.04 to 1<sup>59</sup> indicating that there are 2.26 TCNE molecules per vanadium. If we assume every TCNE is singly charge this might indicate that higher valences of vanadium are achieved for some V atoms to accommodate charge transfer to the excess TCNE. On the other hand, this excess TCNE may be the result of neutral TCNE that is incorporated into the film but plays no part in charge transfer from the

vanadium. If this is the case then some vanadium centers might have lower valences. In this light, Fig. 4.10 shows a comparison of CFM calculations (CFM theory was used because it provides the better overall fit to the experimental data) for different valence states of vanadium. As can be seen from the figure the  $d^2$  ( $V^{3+}$ ) and  $d^4$  ( $V^{1+}$ ) configurations produce wildly different spectra than the  $d^3$  ( $V^{2+}$ ) configuration. The calculated spectra are also shifted from the  $d^3$  case as one would expect. The  $d^2$  configuration, having one less electron in the outer shell will have a higher binding energy as the core electrons are drawn in tighter around the nucleus. On the other hand the  $d^4$  configuration has one more electron and an accompanying lower binding energy. The  $d^4$  spectrum clearly has no intensity in the regions of the excess intensity of the experimental spectrum since it is shifted to lower binding energies and is not a likely candidate for the source of the excess intensity. The  $d^2$  spectrum, on the other hand, is shifted to higher binding energies which places some intensity in the region of the excess intensity observed in the experimental spectrum. It is clear from comparison to the  $d^3$  calculated spectrum that the fit to the experimental spectrum is not improved with the  $d^2$  configuration, but it cannot be ruled out that there is some contribution from  $V^{3+}$  to this excess intensity in the experimental spectrum.

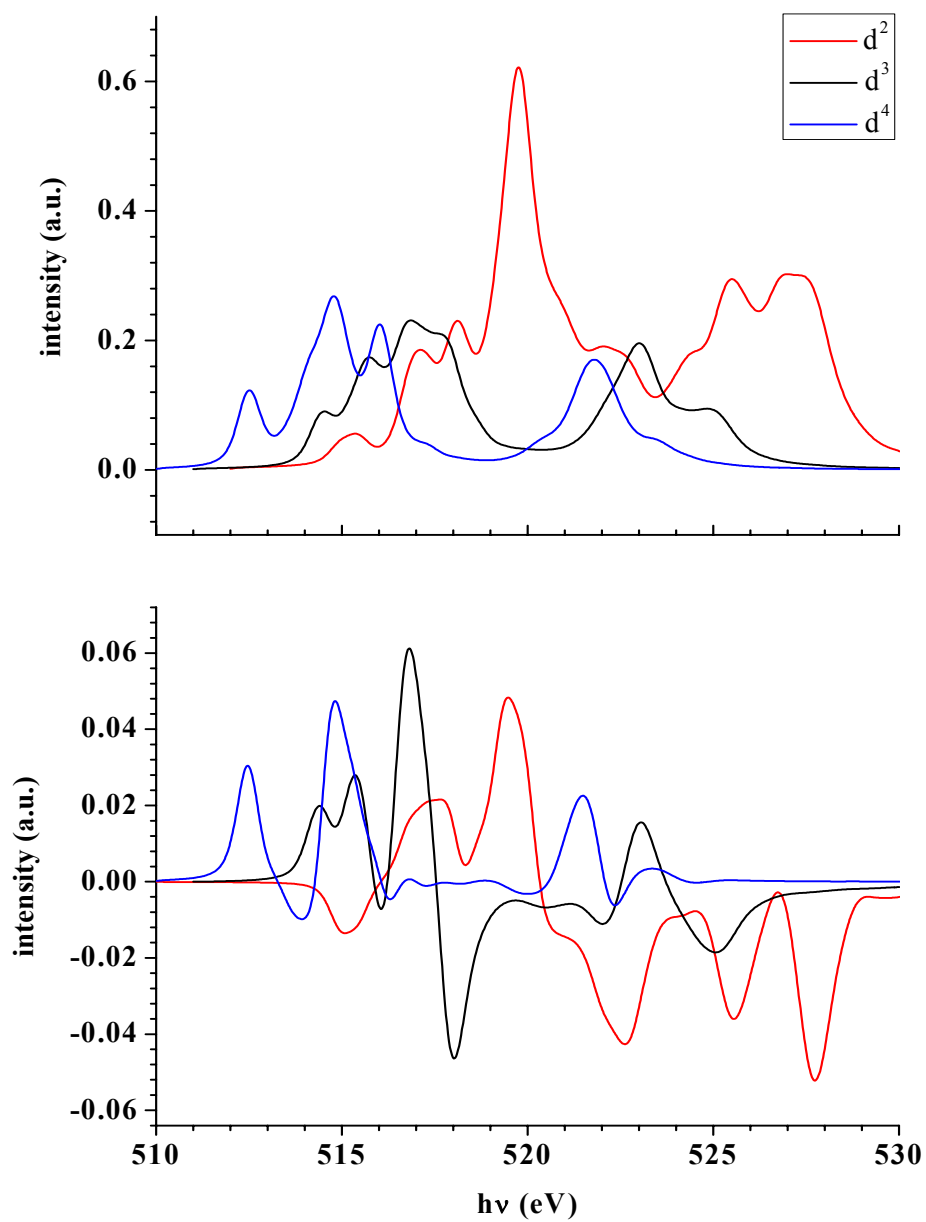


Figure 4.10. CFM calculated XAS (top panel) and MCD (bottom panel) spectra using the pure  $d^2$ ,  $d^3$ , and  $d^4$  configurations. Each calculation was accomplished with a crystal field splitting strength  $10Dq = 2.4$  eV.



To examine this further, a closer inspection of the nature of this missing intensity needs to be made. Fig. 4.11 shows a plot of the experimental data along with the CFM theory calculated spectra with two added Gaussian peaks in the energy regions of the missing intensity. As can be seen in the figure the new fit is greatly improved over the CFM theory calculated spectra with the addition of the two Gaussian peaks.

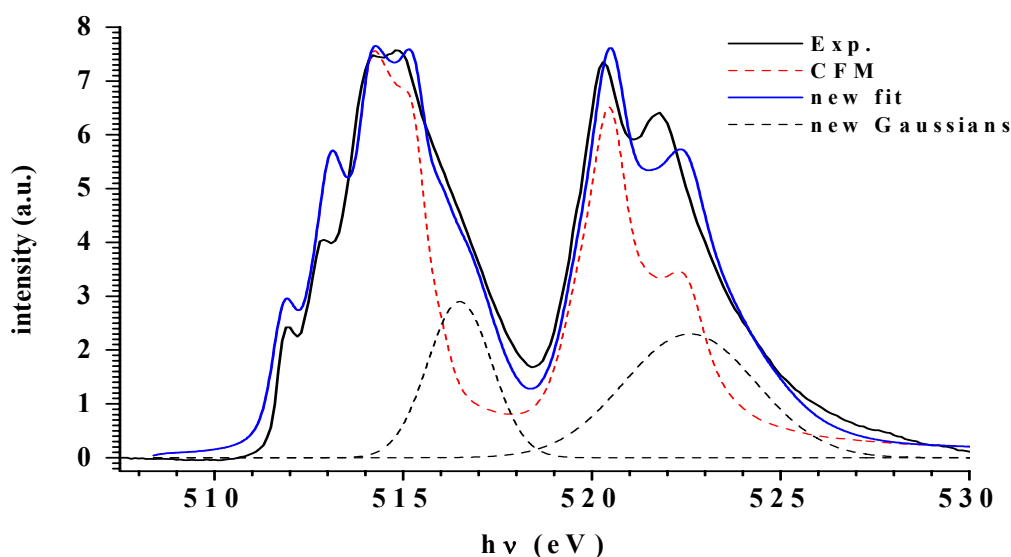


Figure 4.11. The experimental XAS spectrum fitted with the CFM theory calculated spectrum plus two Gaussian peaks located in the energy region of the excess intensity from the experimental spectrum.

The contribution these Gaussians make to the area of each edge is 19.8% for the  $L_3$  edge and 31.6% for the  $L_2$  edge. Using the earlier result for the chemical analysis of  $V[TCNE]_{\sim 2}$  CVD films the ratio of N to V is 9.04 or 2.26 TCNE to 1 V and assuming that each TCNE is singly negatively charged, i.e. accepts one electron from V, we find

that 26% of the vanadium atoms will be triply charged,  $V^{3+}$ , due to the excess TCNE. This is well within the range of the area generated by the excess intensity in the experimental spectrum. However, one can imagine that a 26% contribution from the  $V^{3+}$  spectrum in Fig. 4.11 would substantially alter the overall fit possibly even leading to a decrease in the quality of the fit on the low energy side of the absorption edges making it unlikely that the excess intensity can be attributed solely to contributions from  $V^{3+}$ . Nonetheless, it cannot be ruled out that absorption due to  $V^{3+}$  contributes to the excess intensity and should be considered.

It is apparent that the various multiplet calculation models cannot definitively reveal the origin of the excess intensity in the experimental XAS spectrum for vanadium. This is not entirely surprising given the assumptions of the multiplet approach and the nature of the  $V[TCNE]_{-2}$  system. The multiplet theories use a parameterization approach of solid state effects, i.e. physically meaningful parameters such as spin-orbital coupling constants, Slater integrals and crystal field parameters are extracted from the experimental data by adjusting the parameters until a qualitative fit is obtained. These models do not require *a priori* knowledge of the ligand but treat the ligand field as an effective electrostatic field. In this sense both the crystal field and charge transfer models are best suited for localized system in which both the initial and final states are constrained to the exciting atom. If the final state wave function is more delocalized the multiplet approach becomes less meaningful and a more appropriate approach such as multiple scattering theory should be employed.<sup>60</sup> This does, however, raise an interesting point in that the multiplet approach does indeed provide a good qualitative fit for the low energy side of both the  $L_3$  and  $L_2$  edges where the final state wave function is expected to

be strongly localized and where Coulombic interactions between electron in the  $3d$  shell are very strong. On the other hand, at higher energies the  $3d$  character of the final state wave function is less, Coulombic interactions are weaker, and the final state wave function is more delocalized and the multiplet models fail to produce a good qualitative fit to the experimental data.

Apart from conducting multiple scattering theory calculations, for example, the answer to the origin of the excess intensity in the experimental XAS spectrum may lie in comparison to other vanadium compounds. Probably the most common system is found with vanadium oxides which come in a number of different varieties and valences such as vanadium(II) oxide (VO), vanadium(III) oxide ( $V_2O_3$ ), vanadium(IV) oxide ( $VO_2$ ), and vanadium(V) oxide ( $V_2O_5$ ).  $V_2O_3$  in particular is an interesting system in that it displays a metal-insulator transition (MIT) which allows one to directly examine the electronic structure of the same material in both the insulating and metallic phase. Strong hybridization of the V  $3d$  and O  $2p$  levels in  $V_2O_3$  is evidenced by the appearance of an O  $2p$  XAS peak<sup>61</sup> and supported by soft x-ray emission results for other vanadium oxides.<sup>62</sup> In a purely ionic picture the O  $2p$  level would be fully occupied and, thus, one would not detect unoccupied states in the orbitals. Another observation is broadening of the vanadium XAS peak in  $V_2O_3$  for the metallic phase over the insulating phase.<sup>63</sup> The possible explanation for this observation is a decrease in the electron-phonon coupling in the insulating phase where the interatomic V-V distance in the ground state is close to that in the excited state and thus experiences less Franck-Condon broadening (narrower XAS peak) than the metallic state. In comparison to the  $V[TCNE]_{-2}$  system where the V-V distance is expected to be quite large due to the size of the TCNE moieties we would

expect to see a narrow peak following this logic. On the contrary, the vanadium peak is quite broad and thus electron-phonon coupling does not seem a plausible explanation. In addition, the separation in energy between the main peaks and this excess intensity is on the order of eV and not tenths of eV as we would expect if it were due to phonon coupling.

Other, possibly closer, related vanadium compounds are vanadium nitrides. Reported V-N distances in vanadium nitrides are identical to those reported by Haskell, et al. for V[TCNE]<sub>~2</sub>, which may indicate similar interactions between the V and N atoms in both compounds.<sup>51,64</sup> X-ray emission spectroscopy (XES) studies indicate strong hybridization between the V *3d* and N *2p* as evidenced by features located at the same energies below the Fermi level.<sup>65</sup> As with the vanadium oxides this is not unexpected as both tend to possess a rocksalt structure like NaCl in which each atom is octahedrally coordinated by the other, and for the vanadium this means it displays crystal field splitting behavior and the *e<sub>g</sub>* orbitals overlap strongly with the ligands. In XPS of vanadium nitrides the V *2p* spectra typically have broad satellite structures to the high binding energy side which are attributed to nitrogen vacancies because as the nitrogen content decreases the satellite structure intensity increases.<sup>66</sup> This increase in intensity of these satellite structures is due to poor screening of the core-hole. Fuggle, et al. provide a detailed treatment of poorly screened versus well screened core-holes.<sup>67</sup> Poorly screened core-holes features arise in XPS spectra from empty screening orbitals located above the Fermi level that are strongly coupled to the delocalized electrons of the system. After the core electron is photoexcited to the continuum these empty screening levels are lowered in energy due to the core-hole potential. This increases the probability that these

levels will be populated by remaining electrons and because they are not coupled to delocalized states the core electrons are poorly screened. These poorly screened states show up at higher energies in the XPS spectrum; whereas, well screened state typically show as the main line absorption. A similar mechanism can occur in XAS where the core electron is captured in unoccupied valence orbitals. If these unoccupied valence orbitals are strongly coupled to delocalized states the core electron excited into them then becomes delocalized and the result is poorly screened states. Considering the  $V[TCNE]_{-2}$  system there is a large intensity on the high energy side of the main absorption line ( $L_3$  and  $L_2$ ) which could very well be due to poorly screened states.

Another possibility is that this results from direct probing of antibonding states from hybridization between the V and N atoms.  $\sigma$ -type bonding between  $d_{z^2}$ -like states and  $sp$  orbitals from the N would form deeply bound states and correspondingly high energy antibonding states and are an unlikely candidate as the source of the unoccupied states leading to the excess intensity. However,  $\pi$ -type interactions between the  $d_{xy}$ -like states of V and  $\pi^*$  states of N would be a likelier candidate to form antibonding states in the energy region in question. Further examination of this issue is needed to confirm the source of this excess intensity.

#### **4.1.2 The Carbon and Nitrogen K-Edges**

Gas phase neutral tetracyanoethylene ( $TCNE^0$ ) XAS spectra were collected to examine the unperturbed electronic structure of the TCNE molecule prior to incorporation into the  $V[TCNE]_{-2}$  films. In this manner, the two are compared to observe changes in the electronic structure to provide clues as to the interaction of the TCNE with the vanadium and the nature of magnetism and charge transport in  $V[TCNE]_{-2}$ .

#### 4.1.2.1 Gas Phase TCNE<sup>0</sup>

The carbon and nitrogen K-edge absorption results for gas phase TCNE<sup>0</sup> are shown in Fig. 4.12. To the best of our knowledge this is the first report of XAS for gas phase TCNE. In each edge there are three main features observed with similar energy spacings. This is a key observation in that it indicates that despite the localized nature of XAS we are probing the molecular or delocalized electronic structure of the TCNE molecule. In effect we are accessing the molecular orbitals in TCNE from different sites across the molecule which could be very useful in determining the interplay of the TCNE with the V in the condensed phase films.

This result is very similar to previous reports of electron energy loss spectroscopy (EELS) spectra for *trans*-dicyanoethylene where the authors also indicate the final states belong more to the molecular orbital structure than to one localized on any one absorbing site.<sup>68</sup> EELS and XAS are complimentary techniques for viewing element specific inner shell excitations. The former inducing core excitations with incident electrons and the latter with incident x-rays. Both techniques provide information of the unoccupied electronic structure above the Fermi level. The nitrogen edge observed here also compares well to NEXAFS conducted on thin films of TCNE by Tengstedt, et al. (the carbon edge was not reported in this case).<sup>69</sup>

In comparison to *trans*-dicyanoethylene the absolute energy level will be lowered by the addition of two more electron withdrawing cyano groups to form tetracyanoethylene due to inductive effects.<sup>70</sup> However, theoretical calculations of vertical valence excitation energies and the LUMO and LUMO<sup>+1</sup> valence orbitals of TCNE indicate similar unoccupied orbitals lie above the Fermi energy level with roughly the same

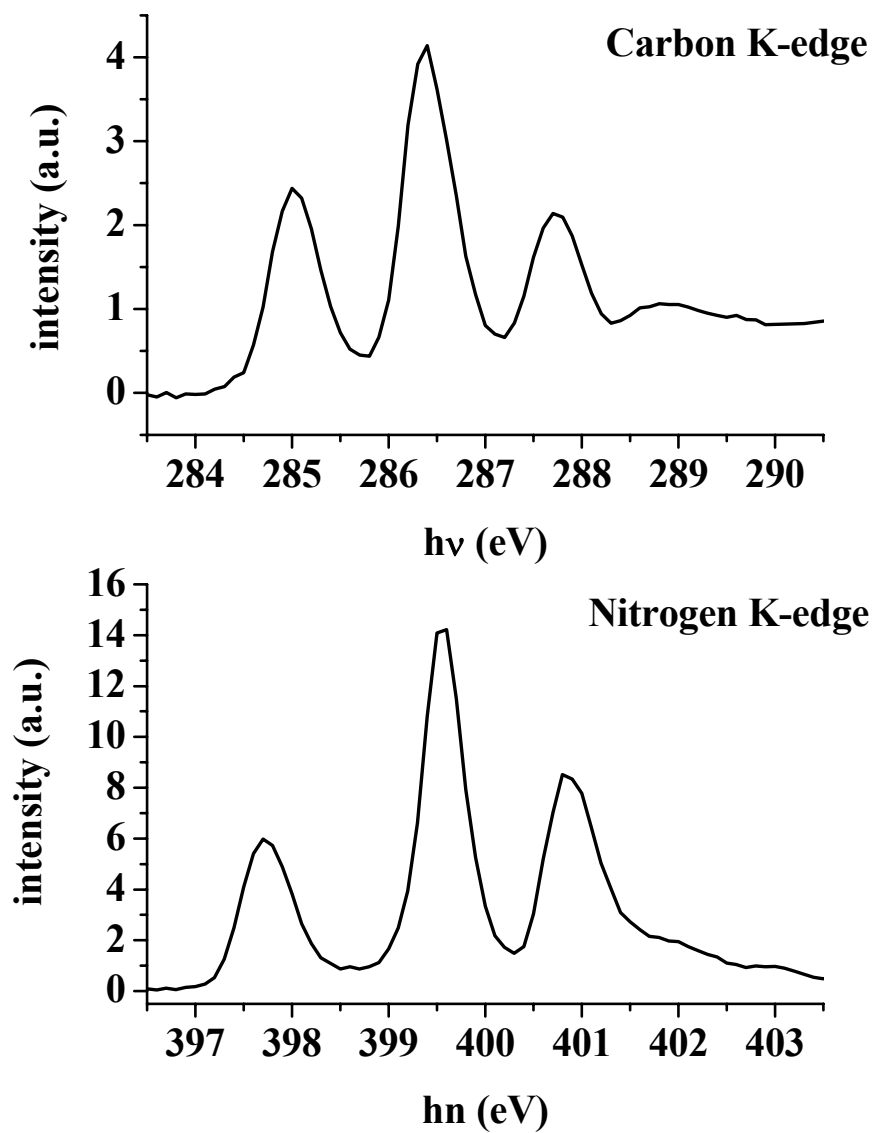


Figure 4.12. Carbon (top) and nitrogen (bottom) K-edge x-ray absorption results. Both spectra are presented as-recorded, i.e. no normalization or background subtractions have been accomplished.

relative energy ordering.<sup>71,72</sup> Indeed, molecular orbital calculations for vertical valence excitation energies and molecular orbital calculations do not establish a definitive comparison of the core excitations of the two molecules as a full description of the oscillator strengths of the various symmetry allowed transitions would need to be determined. Nonetheless, we will make peak assignments based on the available data from the EELS spectroscopy of *trans*-dicyanoethylene and the calculations for TCNE. Following the report of Hubin-Franskin, et al., the peak located at 285.0 eV in the carbon edge is assigned to a transition from the ethylenic (central) carbons to the  $\pi^*_{\text{C}=\text{C}}$  antibonding orbital which is centered mainly on the  $sp^2$  carbons and slightly delocalized onto the  $\text{C}\equiv\text{N}$  groups. The second peak at 286.4 eV is assigned to the transition from the nitrile ( $sp$ ) carbons to the in-plane  $\pi^*_{\text{C}\equiv\text{N}}$  molecular orbital. The highest energy peak at 287.7 eV is assigned to the transition between the  $sp$  carbons and an antibonding orbital which is partly delocalized over the entire molecule but has its largest charge density centered on the  $\text{C}\equiv\text{N}$  groups. These assignments also follow intuitive arguments that the  $sp$  carbons, being bonded to the more electronegative N atoms, would have higher photon energies than the  $sp^2$  carbons because the electron density is drawn away leaving the core electrons drawn in to the nucleus similar to that observed in XPS studies.<sup>73</sup>

The nitrogen atoms provide a clearer case as there is only one type of nitrogen atom in TCNE<sup>0</sup>. The lowest energy peak of the nitrogen edge at 397.7 eV is assigned to the transition between N atoms and the same antibonding molecular orbital ( $\pi^*_{\text{C}=\text{C}}$ ) that results in the lowest energy peak in the carbon edge. The second, most intense peak at 399.6 eV is assigned to the transition between N and the in-plane  $\pi^*_{\text{C}\equiv\text{N}}$  molecular



orbital. Finally, the highest energy peak at 400.8 eV is assigned to the transition between N and the out-of-plane  $\pi^*_{\text{C}\equiv\text{N}}$  molecular orbital.

XAS is largely a local probe of atomic electronic structure, but the evidence presented here clearly supports the use of XAS as a probe of molecular orbital structure as well. These similarities, not only in the number and spacing of the peaks in the C and N edges but also in the peak assignments, indicate that we are probing the molecular electronic structure of TCNE from slightly different core electron sites. A similar observation has also been made for other cyano containing compounds in which the authors note that a building-block approach typically associated with the localized probe picture is insufficient to interpret their data but rather a more delocalized picture is necessary and supported with semiempirical calculations.<sup>74</sup> This is a key observation in that it indicates the accessibility of the molecular orbitals from any given site on the molecule. In the  $\text{V}[\text{TCNE}]_{\sim 2}$  the nitrogen atoms are coordinated directly to the vanadium atoms but this result indicates that that picture may not be suitable and interactions between the vanadium and TCNE molecular orbitals may be more appropriate.

#### **4.1.2.2 $\text{V}[\text{TCNE}]_{\sim 2}$ Films**

In comparison to the TCNE, the carbon and nitrogen K-edge spectra for the condensed phase  $\text{V}[\text{TCNE}]_{\sim 2}$  films are shown in Fig. 4.13 along with the  $\text{TCNE}^0$  spectra. The three main features observed in  $\text{TCNE}^0$  in each edge persist in the  $\text{V}[\text{TCNE}]_{\sim 2}$  films albeit broadened by condensed state effects induced by strong intermolecular interactions which leads to increased delocalization of the final states such as previously described.<sup>75,76</sup> This indicates that the molecular orbital structure of the TCNE remains largely intact after incorporation in  $\text{V}[\text{TCNE}]_{\sim 2}$ , which is consistent with the spin density

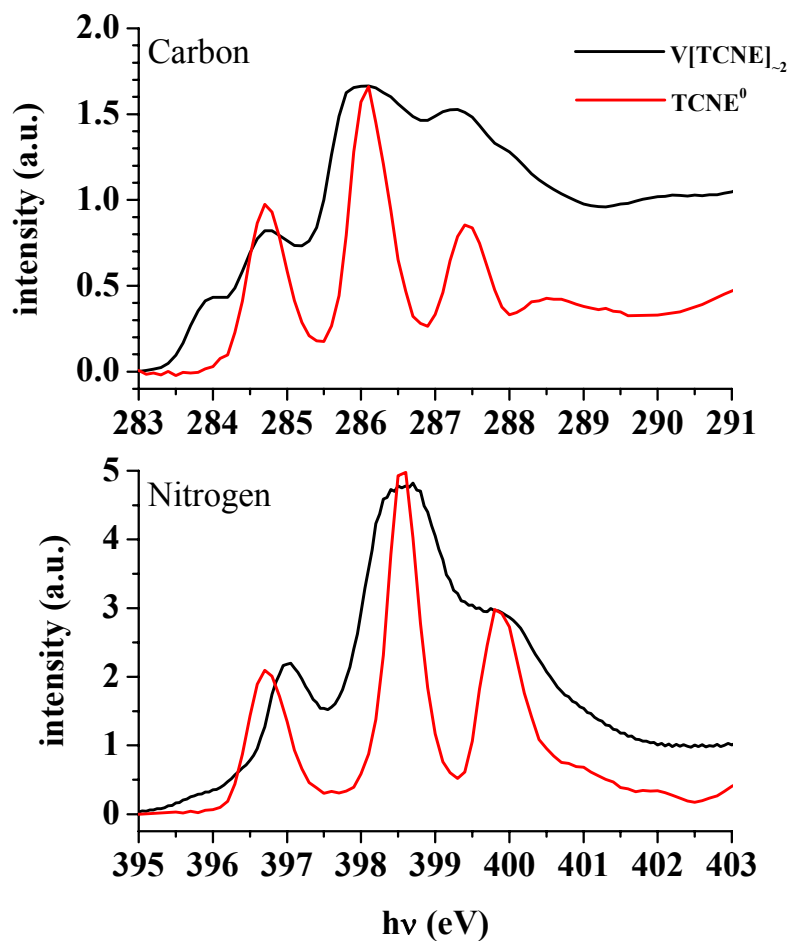


Figure 4.13. Comparison of the V[TCNE]<sub>-2</sub> condensed films carbon (top) and nitrogen (bottom) K-edge x-ray absorption spectra with the TCNE<sup>0</sup> spectra. The V[TCNE]<sub>-2</sub> spectra have both been normalized to between 0 (below the absorption edge) and 1 (well above absorption edge). The TCNE<sup>0</sup> spectra are as-recorded, i.e. no normalization or background subtractions have been conducted.

studies of [TCNE]<sup>•-</sup> that show the molecular orbital structure of the LUMO is largely maintained upon population with the single electron.<sup>77</sup> Thus, we assume the main features arise from the same transitions in V[TCNE]<sub>-2</sub> films as in the gas phase TCNE<sup>0</sup>. In the C K-edge spectrum what appears to be splitting of the lowest energy peak is observed with a new peak at 284.0 eV and a slight shift to lower energies in the other three features with peak positions of 284.7, 286.1, and 287.3 eV, a shift between 0.3 and 0.4 eV. A new, small feature below the lowest energy nitrogen peak is also observed at approximately 395.8 eV and a shift in energies of the other three features with new positions of 397.0, 398.6, and 400.0 eV, a shift between 0.7 and 1.0 eV. The shift in energy is expected as previous reports have indicated that the valence, and presumably higher, states of TCNE are shifted down as an electron is added to the  $\pi^*$  orbital to form [TCNE]<sup>•-</sup>.<sup>78</sup>

It is tempting to attribute the new peak in the carbon and nitrogen spectra to new states created from hybridization of the TCNE with the V centers. Such an interaction should be accompanied by a considerable rearrangement in the molecular orbital structure of TCNE in going from the neutral to the reduced form.<sup>79</sup> This is clearly not the case here as the TCNE molecular orbital structure remains largely intact in the condensed phase film. The relatively small spacing between the new peak and the former lowest energy peak suggests that it may be due to differential screening of the  $sp$  and  $sp^2$  carbon sites. The EELS spectrum of the *trans*-dicyanoethylene mentioned earlier reveals two low energy features separated by 0.82 eV that are attributed to excitation to the same molecular orbital but that originate from two different carbons. The high resolution data obtained in this study would allow us to resolve such a splitting of these two peaks for the

condensed phase films that are split by 0.7 eV. This effect has been demonstrated previously and attributed to XPS binding energy splittings due to the different chemical environments in the carbon atoms in acrylonitrile and propionitrile. Features for absorbing atoms in poorly screened chemical environments, i.e. those that have electron density withdrawn, appear at higher photon energies than those with more electron rich environments or are well screened appear at lower photon energies. Fig. 4.14 shows the LUMO and LUMO<sup>+1</sup> electronic density contours for TCNE calculated by second-order Møller-Plesset perturbation theory (MP2). It appears that in the now partially occupied orbital of [TCNE]<sup>•-</sup> (former LUMO) the charge density from the additional electron is concentrated around the *sp*<sup>2</sup> carbon atoms but also has significant charge density on the *sp* carbons as well making this mechanism an unlikely candidate to induce such a large splitting of the lowest energy peak in the XAS spectrum of carbon. In addition, there is also a new low intensity feature below the lowest energy peak in the nitrogen spectrum as well which can not be explained by similar screening effects.

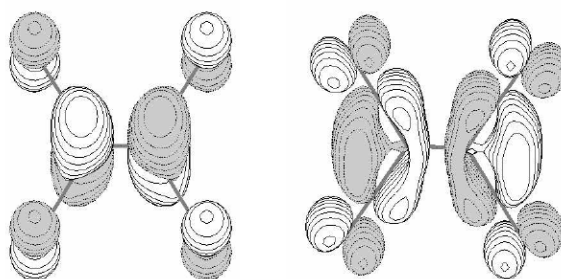


Figure 4.14. The LUMO (left) and LUMO<sup>+1</sup> (right) electronic density contours for TCNE. Spin density calculations for [TCNE]<sup>•-</sup> indicate the partially occupied orbital (former LUMO) retains much of the general shape and electron density distribution as the LUMO shown here. Figure reprinted with permission.(Reprinted from Ref. 72 with permission)

We propose that the new features are due to spin splitting of the singly occupied molecular orbital (SOMO). Oprea, et al. performed calculations for the spin density of isolated  $[\text{TCNE}]^{\bullet-}$  and reported spin density values consistent with those found experimentally. Further their calculations reveal an energy difference between the  $\alpha$  (positive) and  $\beta$  (negative) spin densities in the HOMO, SOMO, and the new LUMO, formerly  $\text{LUMO}^{+1}$ . In the  $\text{V}[\text{TCNE}]_{\sim 2}$  the  $[\text{TCNE}]^{\bullet-}$  are surrounded by  $\text{V}^{2+}$  centers having a rather large spin moment which leads to obvious magnetic ordering in the condensed phase. It is then reasonable to assume that there is some degree of magnetic exchange between the  $[\text{TCNE}]^{\bullet-}$  and  $\text{V}^{2+}$  in the system. Magnetic exchange gives rise to an energy splitting of the up and down spin orbitals, and thus, we hypothesize the splitting of the lowest energy XAS peaks is representative of the energy differences due to spin splitting of the SOMO in  $[\text{TCNE}]^{\bullet-}$ .

Another discrepancy of note is the difference in the energy spacing between the two lowest energy peaks in the N K-edge. In the  $\text{TCNE}^0$  the two lowest energy peaks are separated by 1.2 eV, but in  $\text{V}[\text{TCNE}]_{\sim 2}$  the two lowest energy peaks are separated by only 0.7 eV. Since the nitrogen atoms are those that are directly coordinated to the vanadium atom in the condensed phase films these differences may be attributed to that fact. Any back bonding occurring in the  $\text{V}[\text{TCNE}]_{\sim 2}$ , charge transfer from the nitrogen atoms to the vanadium atoms via  $\text{N } 2p - \text{V } 3d$  interaction, would lead to a lower charge density on the nitrogen atoms and hence more tightly bound core electrons. However, such an occurrence would lead to a shift in the entire spectrum to higher energies and not merely a change in the spacing of the two lowest energy peaks. On the other hand, one could also view strong  $\text{N } 2p - \text{V } 3d$  interactions from the standpoint of increasing the

charge density surrounding the N atoms from the V 3d electrons. In this case the N would become more screened and the unoccupied states would show up at lower photon energies. Again, if this were the case the entire spectrum should shift to lower energies which is clearly not the case. Occupied valence band spectra of V[TCNE]<sub>~2</sub> show a similar discrepancy in spacing of the three main features with the lowest binding energy feature (analogous to the lowest unoccupied state probed here) well separated from the highest intensity peak. The discrepancy may arise from deeply bound occupied states that are reflected in the unoccupied valence states observed in XAS. This would then suggest that these bound states are disrupted in the condensed films and the unoccupied states observed in the XAS spectrum are more reflective of the valence orbital structure rather than bound states. The situation is unclear, however, due to the disordered nature of the V[TCNE]<sub>~2</sub> and the origin of the unoccupied valence states.

We can now examine the MCD spectra. Fig. 4.15 shows the MCD and XAS spectra for both carbon and nitrogen K-edges in V[TCNE]<sub>~2</sub>. The carbon spectrum shows a large, negative-going MCD feature at 285.1 eV which coincides with the XAS feature at 284.7 eV which was assigned to the transition between the  $sp^2$  carbon atoms and the  $\pi^*_{C=C}$  orbital. There is also a positive-going feature coincident with the new XAS peak at ~284 eV that was attributed to spin splitting of the SOMO. The opposite polarization of these two lowest energy peaks is consistent with a spin splitting picture in that the unoccupied states would have polarizations commensurate with the occupied SOMO. In an ideal spin split SOMO the spin-up orbital would be completely full and the spin-down would be completely empty, which is clearly not the case here as both orbitals are not entirely full as evidenced by the appearance of XAS features. This could be the result of

incomplete charge transfer to the TCNE or the result of the greater portion of the charge density residing on the more electronegative N atoms. However, a more likely scenario is ground state excitation from the spin-up orbitals to the spin-down and higher orbitals or excitation as the result of the XAS process itself. This process is reflected in photoinduced absorption phenomena that occur in the visible in V[TCNE]<sub>2</sub> films.<sup>80</sup>

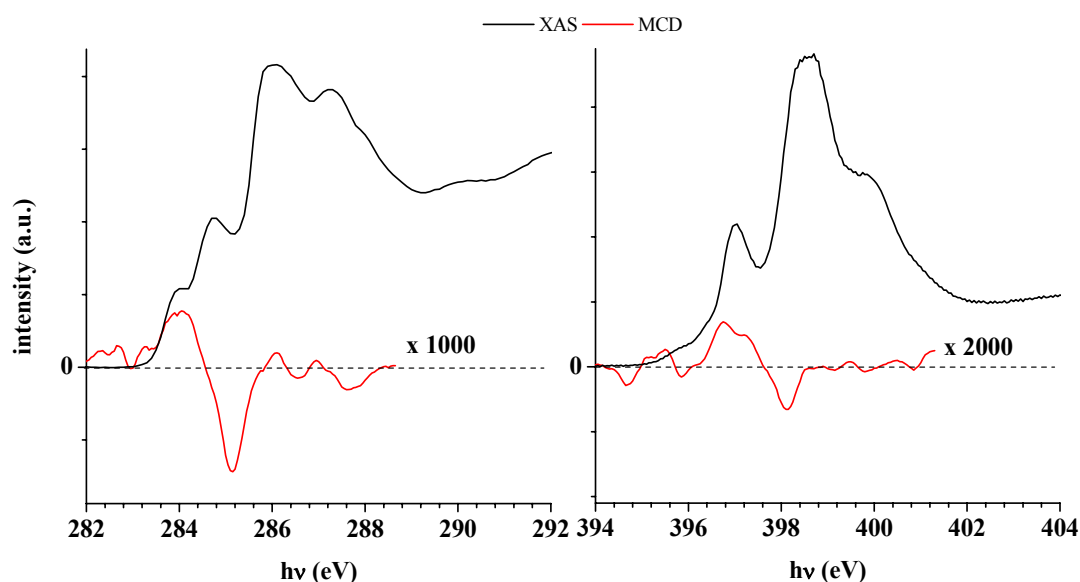


Figure 4.15. Magnetic circular dichroism (MCD) spectra for carbon (left panel) and nitrogen (right panel) collected from V[TCNE]<sub>2</sub> condensed phase CVD films. Both spectra have been normalized to between 0 (pre-edge) and 1 (well above absorption edge).

For the nitrogen MCD spectrum there appears a large negative-going feature at 398.1 eV associated with the largest XAS feature attributed to the transition between the N and the in-plane  $\pi^*_{\text{C}\equiv\text{N}}$  orbital. There is also a broad positive-going feature centered at ~397 eV associated with the lowest energy XAS feature assigned to the N to  $\pi^*_{\text{C}=\text{C}}$  transition.

Unfortunately, the signal to noise ratio in the N MCD spectrum is too low to determine if there is an associated MCD signal for the new low energy feature at  $\sim 396$  eV. Without a strong MCD signal for the lowest energy feature to compare to the next highest energy feature it is difficult to confirm splitting of the SOMO in the case of the nitrogen spectrum. However, we would not expect to see a large MCD feature in the absence of a strong XAS feature. To reconcile this low intensity we remind ourselves that there are two distinct nitrogen atoms in the system: those that are coordinated to vanadium and those that are uncoordinated. These different environments make the electronic structure immediately surrounding the nitrogen as probed via XAS complex and difficult to interpret.

The following section collects the results from the previous sections describing the results of the XAS and MCD spectroscopies to develop a model for the interactions between the vanadium and TCNE sub-lattices in an attempt to explain the origin of the magnetic interactions in  $V[TCNE]_{-2}$ .

## **4.2 Putting it All Together**

The similarities in carbon and nitrogen XAS spectra in the gas phase  $TCNE^0$  spectra signify that the unoccupied states above the Fermi level are comparable or arise from similar final states. The explanation for this is that the XAS is probing not the local atomic electronic structure but more the global molecular electronic structure as mentioned in the previous section but from different sites across the molecule. This can be viewed as a building block approach to probing the molecular orbital structure as the XAS is still a highly localized spectroscopy method. In this case we are probing the various lobes of the molecular orbital that are localized on different portions of the



molecule. What is important to note is that the electronic structure remains largely intact in going from the gas phase  $\text{TCNE}^0$  to the condensed phase  $[\text{TCNE}]^{\sim-}$  of  $\text{V}[\text{TCNE}]_{\sim 2}$ . This suggests that whatever the origin of these unoccupied states they play a large role in the unoccupied valence structure of  $\text{V}[\text{TCNE}]_{\sim 2}$ .

Concerning the vanadium spectrum, the origin of the excess intensity on the high energy side of the two absorption edges is not entirely clear. It is likely that the origin of this excess intensity arises from multiple sources such as higher valence states of vanadium, charge transfer states, and poorly screened states. The most intriguing candidates are higher valences of vanadium consistent with the XPS data and poorly screened states consistent with hybridization of the V and TCNE. On the other hand, the lower energy features may hold the key to the nature of the interactions between the V and TCNE sub-lattices.

For the  $\text{V}[\text{TCNE}]_{\sim 2}$  the unoccupied structure observed from the XAS data is consistent with the results of the occupied valence states of  $\text{V}[\text{TCNE}]_{\sim 2}$ . de Jong, et al. reported the results of photoemission spectroscopy (PES) on  $\text{V}[\text{TCNE}]_{\sim 2}$  as shown in Fig. 4.16 where the PES for TCNE, rubidium doped TCNE and  $\text{V}[\text{TCNE}]_{\sim 2}$  are shown. The PES technique probes the occupied states of a material but is not element specific. The TCNE PES spectrum mirrors that of the N and C XAS spectra conducted in this study again indicating that the XAS is probing the molecular orbital structure rather than localized atomic orbitals. In the Rb doped TCNE case there are two new features at lower binding energies that de Jong, et al. have attributed to the destabilized HOMO (3.5 eV) and the singly occupied molecular orbital (SOMO) or the former LUMO (1.5 eV). In the  $\text{V}[\text{TCNE}]_{\sim 2}$  case the PES is now also going to probe the occupied V 3d states

which are attributed to the peak at  $\sim 1$  eV; whereas, the destabilized HOMO remains at 3.5 eV but now the SOMO is reported to be at 2.5 eV. The feature at  $\sim 6$  eV indicates a rigorous rearrangement of the bonding states probably due to hybridization of the V and TCNE and consistent with the excess intensity in the experimental vanadium XAS spectrum as unoccupied states.

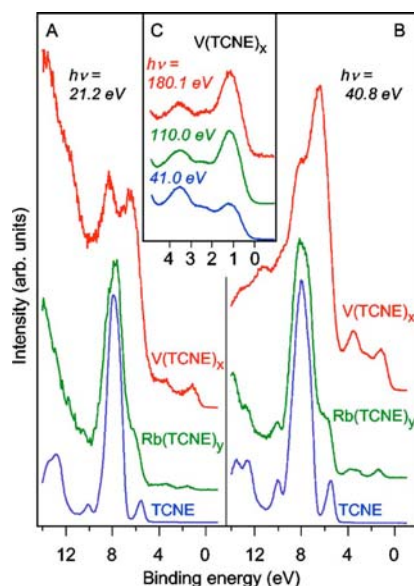


Figure 4.16. Valence band photoemission spectra of condensed phase TCNE, Rb-doped TCNE, and  $V[TCNE]_{-2}$  films. Panel A – spectra with incident  $h\nu = 21.2$  eV, Panel B – incident  $h\nu = 40.8$  eV, and Panel C – low binding energy spectra of  $V[TCNE]_{-2}$  recorded at various incident radiation energies. (Reprinted Figure with permission from Ref. [55]. Copyright (2007) by the American Physical Society.) See text for discussion.

The picture developed from the results of this study indicates that the interpretation is more complex than that described above. Fig. 4.17 shows a plot of the three absorption edges studied in this work with their energy scales adjusted so that their lowest energy features are aligned. In this case the nitrogen spectrum has been fit using a nonlinear

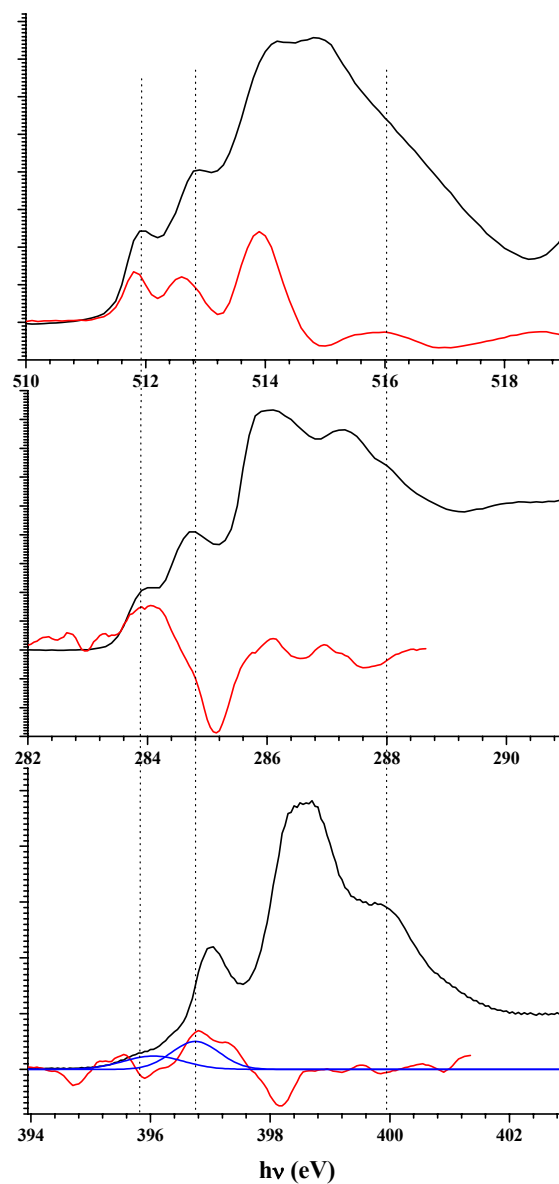


Figure 4.17. The three absorption edges studied in this work. The energy scales have been adjusted so the lowest two features in each edge are aligned. The nitrogen plot (bottom plot) shows the results of peak fitting the nitrogen spectrum (only the two lowest energy fitting peaks are shown for clarity) indicating the new low energy feature is actually two new features; the energy scale is then adjusted so these two features align with the two lowest energy features in vanadium and carbon.

least squares fitting routine and the results reveal that the new feature on the low energy side of the nitrogen spectrum is actually two features that have the same energy splitting as the two lowest energy features in the vanadium and carbon spectra. This remarkable alignment of the two lowest energy features in each spectrum suggests a degree of energy alignment between empty  $d$  states of vanadium and empty  $\pi^*$  states of TCNE. The magnitude of the exchange splitting as suggested by the separation of the spin split peaks in the carbon and nitrogen spectra is rather large, 0.7 eV, roughly an order of magnitude larger than that expected for  $V[TCNE]_{\sim 2}$  as calculated previously.<sup>14</sup>

It is possible that the V multiplet splitting determines the exchange splitting in TCNE. It has been shown that the multiplet structure in transition metal compounds is highly sensitive to the type of ligand present in the complex and that the shape of the metal center spectra is closely related to the type of metal-ligand interaction.<sup>81</sup> In fact this model proposes that the type of interaction is more important than the molecular symmetry or the number of  $d$ -electrons in the final state. This might seem to imply that, for example, the CFM calculations reported earlier in this work only coincidentally model the low energy side of the  $L_3$  edge. However, a report of various Fe-complexes revealed that a molecular orbital approach and the crystal field multiplet theory approach are not mutually exclusive. In this report it was found that the multiplet approach does indeed provide a superior model of the spectrum and extended Hückel molecular orbital (EHMO) calculations revealed that the lower lying features possess admixtures of the metal  $3d$  states in the case of the ligands and strong  $\pi^*$  states character for the metal spectra.<sup>82</sup> While detailed theoretical calculations have yet to be accomplished for the  $V[TCNE]_{\sim 2}$  system the experimental results suggest that vanadium multiplet states are

strongly interacting or hybridized with the  $[\text{TCNE}]^{\bullet-}$   $\pi^*$  states or more specifically the  $\pi^*_{\text{C}=\text{C}}$  states. This interaction may also play a part in directing the size of the exchange energy between the vanadium and the TCNE.

Closer inspection of the XAS and MCD reveals the nature of the interactions between the vanadium and TCNE in this system. This model is based on the spin delocalization or superexchange model as described in Ref. 83. The models are a form of configuration interaction in which the differences arise from which energy levels are admixed with the ground state wave function. The spin delocalization model for intramolecular exchange is described by virtual excitation from the POMO to the HOMO on one site followed by a virtual excitation from POMO on a neighboring site to the original HOMO. Superexchange is described by virtual excitation from the HOMO to the POMO on one site followed by a virtual excitation from the POMO on a neighboring site to the LUMO on the original site. In each case ferro- or antiferromagnetic coupling can result. In the case of antiferromagnetic coupling, if equal numbers of spins are aligned antiparallel to each other then there is no net magnetic moment, while unequal numbers of spins would lead to ferrimagnetic ordering and a net magnetic moment. In other instances, these interactions can be described in terms of a spin polarization effect where regions of the same or opposite spin densities overlap giving rise to magnetic ordering.<sup>84</sup> This mechanism is known as the McConnell mechanism I in which he proposed the model based on the concept of theoretical  $\pi$  stacking of conjugated systems. If, when stacked, regions of opposite spin density are overlapped ferromagnetic ordering can result. This mechanism was confirmed in diphenylcarbene systems<sup>85</sup> and later applied to

metallocenium TCNE systems.<sup>86</sup> This mechanism is more often applied to systems composed of intermolecular interactions as opposed to intramolecular interactions.

If we now consider the  $V[TCNE]_{\sim 2}$  system and the peak assignments for the XAS spectra that were made and compare those to the MCD features, the  $V[TCNE]_{\sim 2}$  system can be modeled using the spin delocalization or the superexchange effect. The two lowest energy features in the carbon spectrum are both attributed to the  $\pi^*_{C=C}$  MO with the difference in energy being due to spin pairing energy. Similarly, the two lowest energy nitrogen features are attributed to the same MO. From alignment of features we are assuming that the two lowest energy features in vanadium are also probing the same MO, which also implies some degree of hybridization as discussed earlier. If we then consider the MCD features and reconcile them between the different sites of the system we observe that the  $sp^2$  carbons (central portion of the  $\pi^*_{C=C}$  with largest charge density) have both a positive and negative MCD signal associated with them consistent with the spin splitting picture. The feature in the N spectrum at  $\sim 397$  eV is attributed to the free N atoms, i.e. not coordinated with the V atoms, (greater number of unoccupied states which accounts for the relatively high intensity) and has a positive MCD signal, while the two lowest energy features are attributed to the N atoms coordinated with the V atoms (few unoccupied states because of the additional electrons from the V which accounts for the low intensity) which has an MCD signal too small to assign an orientation either way. Both the lowest energy multiplet features in V have a positive MCD signal. Beginning with the V atoms, they have a positive MCD signal and are strongly interacting with N atoms of the TCNE but with no discernible MCD signal. In this case we will treat this region as a whole and assign a positive polarization to it. The  $sp$  carbons have no XAS

feature in this region and thus no associated MCD feature. Finally, the  $sp^2$  carbons have both a positive MCD and negative MCD signal with the latter being the majority of states, so we assign the central portion of the molecule with an overall negative polarization. With these assignments, we observe opposite spin alignment between the central portion of the TCNE and the V atoms hybridized with the N atoms. The schematic shown in Fig. 4.18 depicts the proposed spin polarization interaction in the  $V[TCNE]_{\sim 2}$  system. In this proposed mechanism the central portion of the TCNE experiences antiferromagnetic coupling via either a spin delocalization or superexchange mechanism with the N-V portion of the system via the  $sp$  carbons. The exact nature of the exchange is not clear from the experimental evidence presented here, but would require theoretical modeling of the system to determine the exact configuration interactions involved amongst these portions of the system that lead to the antiferromagnetic coupling in this system. Presumably the magnitudes of opposite polarization are different giving rise to overall ferrimagnetic ordering and a net magnetic moment. This model supports, in part, the concept of the spin polarized sub-bands in the fully spin polarized half-semiconductor model. While the majority of the TCNE molecule has an opposite polarization to that of the vanadium atoms, the picture is more complex due to the disordered nature of the system.

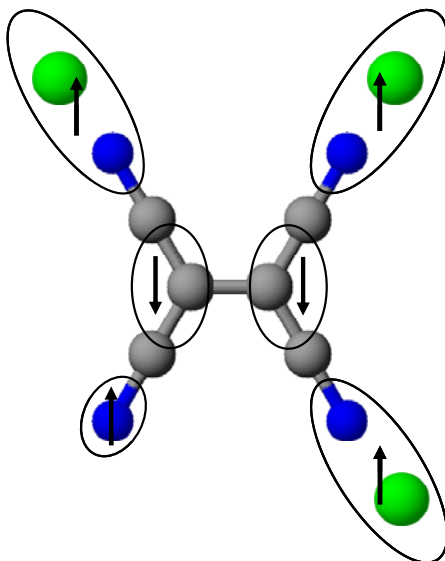


Figure 4.18. Schematic depiction of the proposed spin polarization interaction in  $V[TCNE]_2$  between the central lobe of the  $\pi^*_{C=C}$  orbital, the outer lobe over the N and V atoms. The two central  $sp^2$  C atoms both display negative polarizations while the hybridized N and V atoms display a positive polarization. The uncoordinated N atoms display positive polarization. C – gray, N – blue, and V – green



## CHAPTER 5

### FIELD EFFECTS IN V[TCNE]<sub>~2</sub>

#### 5.1 Field Effects in V[TCNE]<sub>~2</sub>

There were a number of challenges in designing and fabricating a working OFET device based on V[TCNE]<sub>~2</sub>. A common method of fabricating OFET devices is to use highly doped silicon wafers to act as the substrate and gate electrode. This is then coated with a thermally grown silicon oxide layer to serve as the gate dielectric material. Unfortunately, the unpatterned gate electrode tends to lead to large leakage currents which led to the patterned design used in this study (Fig. 3.5). The high conductivity,  $\sim 10^{-2}$  S/cm, of the V[TCNE]<sub>~2</sub> also turned out to be an issue causing large leakage currents through the gate material. In OFET devices using other organic species it has been found that patterning not only the gate electrode but also the organic film drastically reduces the leakage currents realized in the devices.<sup>87</sup> Because of the nature of the CVD deposition of V[TCNE]<sub>~2</sub>, patterning very small areas was not feasible but the films were patterned into smaller areas and then the film around each device was removed via light mechanical scraping to disconnect the portion of film directly over the active channel from the rest of the deposited film. This reduced the overly large leakage currents down to something more workable.

The first order of business once this was accomplished was convince ourselves that we are indeed observing a field-effect in the V[TCNE]<sub>~2</sub> OFET devices. As shown in §3.5 in Fig 3.9 the now reduced leakage current in these devices is typically on the order of 50 to 100 times less than the measured source-drain current,  $I_{sd}$ , usually taking on values of 10 – 100 picoamps which is a common benchmark for OFET devices in concluding that leakage current is sufficiently low and the change in  $I_{sd}$  is due to field-effects.<sup>88</sup> Overly large leakage currents lead to misidentification of field-effects in these devices, but “medium” leakage current also reduce device performance by increasing power dissipation and lower switching speeds. These currents are small enough as to not cause drastic reduction in performance. All the data presented henceforth was collected on devices that displayed a sufficiently small leakage current as discussed above.

Fig. 5.1 shows the percent change in  $I_{sd}$  as a function of gate voltage. The effect is quite small but is real nonetheless given the nearly linear increase with increasing gate voltage. The expected magnitude of the percent change in current with applied gate voltage can be estimated based on the percent change the number of induced charges makes in the active channel relative to the number of repeat units of V[TCNE]<sub>~2</sub>. If it is assumed the capacitor is the size of the active channel, 760  $\mu\text{m}$  by 30  $\mu\text{m}$  and that the flux through each layer of the bilayer capacitor is the same, then with the dielectric constants of 3.9 (PMMA) and 7.5 ( $\text{Si}_3\text{N}_4$ ) we calculate a capacitance of the bilayer of  $2.4 \times 10^{-12}$  F which leads to  $Q = 7.4 \times 10^7$  charges in the V[TCNE]<sub>~2</sub> active channel for an applied gate voltage of 5 V assuming  $Q = CV$ . By estimating the size of the volume of V[TCNE]<sub>~2</sub> repeat unit to be roughly 1  $\text{nm}^3$  or  $1 \times 10^{-27}$   $\text{m}^3$  we can calculate the number of charge carriers in the active channel per V[TCNE]<sub>~2</sub> repeat unit and estimate the

change in current based on the change in the number of charge carriers. Table 5.1 lists the estimated percent change in the source-drain current expected for different gate voltages. In comparing the results plotted in Fig. 5.1 with the estimated change in current listed in Table 5.1 we can see that the observed change in current is very consistent with the number of charges induced in the active channel with the application of a gate voltage compared to the number of unit cells of  $V[TCNE]_{\sim 2}$ .

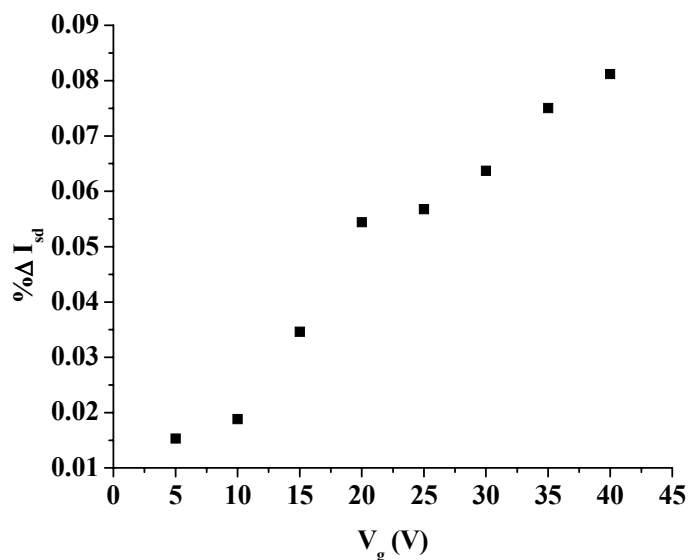


Figure 5.1. The percent change in  $I_{sd}$  as a function of the applied gate voltage,  $V_g$ . In this case the source-drain voltage,  $V_{sd}$ , was held constant at 5V and the gate voltage was returned to 0V between each measurement.

The next concern is the type of effect observed. Under the application of a positive gate voltage negative charge carriers are accumulated in the active channel. For an n-channel material this effectively n-dopes the material and the current increases. The

same is true for a p-channel conductor under the application of a negative gate voltage inducing the accumulation of positive charge carriers in the active channel. In this case the application of a positive gate voltage causes a *decrease* in the source-drain current and suggests that V[TCNE]<sub>~2</sub> is p-channel conductor (higher hole mobility and concentration) which is inconsistent with the charge transport model of Prigodin, et al. where V[TCNE]<sub>~2</sub> is viewed as an n-channel conductor (higher electron mobility) where electrons hop between [TCNE]<sup>•-</sup> moieties. However, application of a negative gate voltage induces no change in the source-drain current contrary to what would be expected for a p-channel conductor.

Gate voltage V <sub>g</sub> (V)	Estimated percent change in current
5	0.011
10	0.022
15	0.033
20	0.043
25	0.054
30	0.065
35	0.076
40	0.087

Table 5.1. The estimated percent change in current for given applied gate voltages.

In addition to this anomalous behavior under the application of a positive gate voltage, the IV characteristics for these V[TCNE]<sub>~2</sub> devices are atypical for OFETs. A plot of I<sub>sd</sub> as a function of the source-drain voltage, V<sub>sd</sub>, is shown in Fig. 5.2 with varying applied gate voltages. The shape of these curves suggests that under the measurement conditions the device is still in the linear regime as shown in Fig. 2.14 and has not yet

reached saturation. In the linear regime the charge density across the active channel is uniform. The beginning of the saturation regime in OFET devices is reached at the point where  $V_{sd}$  is equal to the difference between the gate and threshold voltages ( $V_g - V_{th}$ ) or where the charge density decreases linearly between the source and drain contacts. In this regime a depletion of charge carriers is created in the region near the drain contact and the charge density is pinched off or goes to zero at the boundary between the active channel and the drain contact. The electric field is highest at the drain contact and thus charge carriers are depleted faster than they are transported through the active layer. Even higher source drain voltages will worsen the situation and enlarge the depletion zone until no increase in current is observed for increased  $V_{sd}$ . In the case of the V[TCNE]<sub>2</sub> OFET devices a source-drain voltage of  $\pm 125V$  fails to reach the saturation region even at relatively small gate voltages. Again, this suggests that the threshold voltage for the V[TCNE]<sub>2</sub> is substantial. Unfortunately, as shown in the figure this source-drain voltage induces very high currents in the device,  $\sim 1mA$ , which is extremely high for these types of devices and joule heating becomes an issue which complicates interpretation of the data and irreparably damages the devices.

To examine this more closely we must first reacquaint ourselves with the operation of a transistor. For effective OFET operation two things must occur: 1) charges consistent with the type of conductor must be injected into the active channel and 2) these charges must be mobile. As discussed in the background section the origin of the threshold voltage is low mobility of charge carriers due to charge traps in the organic layer or low charge mobility. Enough carriers must be injected into the active channel to first fill up all of the charge traps before conduction can occur.

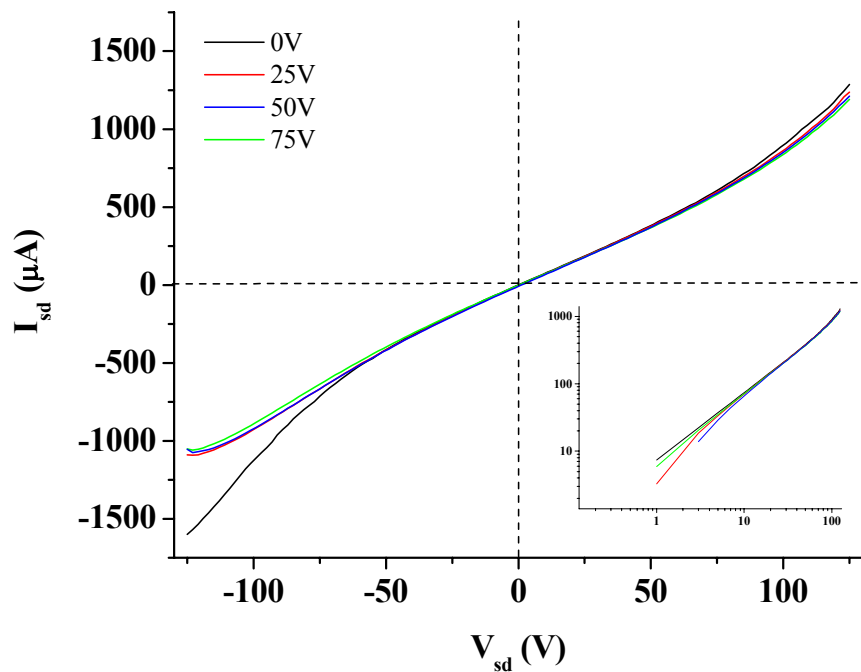


Figure 5.2. IV traces for a typical V[TCNE]<sub>-2</sub> OFET device over a -125V to +125V range with different gate voltages. Inset: the same plot on a log-log scale.

Working on the assumption that V[TCNE]<sub>-2</sub> is an n-channel conductor as implied in the fully-spin polarized model of a half-semiconductor where electrons are transported through the material via hopping between  $\pi^* + U_c$  sub-bands, which is consistent with the significant dark current of V[TCNE]<sub>-2</sub>. Dark currents in field-effect devices have the effect to require the application of a gate voltage just to obtain flatband condition, that is the condition equivalent to when there are no charge carriers present in the active channel and the semiconductor energy band is flat. That is a mismatch between the LUMO of the organic and the metal contacts is such that charge transfer occurs resulting in a dipole and band bending in the organic and the gate voltage must be applied to returned to a flat-

band. This suggests that  $V[TCNE]_{-2}$  is significantly doped with mobile charge carriers before a gate voltage is applied. Under the application of a gate voltage even more charge carriers are injected that fill the  $\pi^* + U_c$  levels effectively decreasing mobility by decreasing the number of sites the electrons have to hop between. This proposed mechanism explains the decrease in current under the application of a positive gate voltage. On the other hand, the application of a negative gate voltage has no effect on the current flowing through these devices.

While this is inconsistent with the operation of a typical n-channel OFET, the concept is not inconsistent with a junction FET (JFET). JFETs operate in a “normally open” configuration meaning the channel is populated with charge carriers and a current flows upon source-drain biasing under a zero applied gate voltage. Application of a nonzero gate voltage acts to squeeze the active channel and reduce the current. The field-effect devices demonstrated here may provide an alternative architecture to standard JFET devices which are simpler in design.

The final discussion point is the constant decrease in current over time in the  $V[TCNE]_{-2}$  devices. As mentioned earlier,  $V[TCNE]_{-2}$  is very oxygen sensitive and even though device measurements were conducted in vacuum small amounts of oxygen can have a profound effect on the operation of these devices. Given the nature of the components in  $V[TCNE]_{-2}$ : TCNE with its rich chemistry makes a good reducing and oxidizing agent, and vanadium which is a highly reductive element, it would not be surprising to find varying degrees of electrochemistry occurring during device operation giving rise to significant rearrangements in the electronic structure and, hence, charge transport. In addition to itself, reactions with the contacts, although unlikely with gold,

and the PMMA are possible also significantly disrupting the charge transport pathways. Another possibility includes structural rearrangements from the stress of passing a current through the material causing shorting and breaking of current pathways effectively reducing the cross sectional area of the conducting channel. While this is all only conjecture, these are very real possibilities and will be examined more closely in the future.



## CHAPTER 6

### CONCLUSIONS

#### 6.1 Summary and Conclusions

##### 6.1.1 Electronic Structure of $V[TCNE]_{-2}$

The electronic structure of  $V[TCNE]_{-2}$  is complex to say the least; however, it also offers a window into the interactions of organic-based magnetic materials. The role of the organic component in these types of systems has been an interesting but yet answered question. While the results presented here may not be indicative of all types of organic-based systems, they do provide insight into the general complexity of these types of systems and the points that must be considered when pursuing next generation materials.

Nonetheless, the results here support a picture of spin delocalization or superexchange of the TCNE partially occupied molecular orbital mediating the magnetic interaction it has with the vanadium giving rise to bulk magnetic ordering of the material. The remarkable similarities in the carbon and nitrogen XAS spectra reveal the value of using XAS to provide a building block approach to probing the unoccupied molecular orbital structure of TCNE. In addition, the lack of substantial changes reveals the robustness of this orbital structure when TCNE is reduced and incorporated into condensed phase films with vanadium. This robustness may play a part in the

intramolecular exchange leading to antiferromagnetic coupling between different portions of the system to effectively mediate the magnetic interaction with the vanadium centers. The vanadium XAS spectrum further emphasizes the complexity of the  $\text{V}[\text{TCNE}]_{-2}$  system. While the spectrum can be modeled using standard atomic multiplet approaches a significant portion of the spectrum is not reproduced well. Comparison to XPS spectra and model systems such as vanadium oxides and vanadium nitrides leads us to conclude the  $\text{V}[\text{TCNE}]_{-2}$  is a mixed valence system with significant hybridization between the V and TCNE which are not modeled well using the current atomic multiplet theories.

Both of these conclusions suggest the current theory of charge transport and magnetic ordering in these materials may be up for reexamination. Hybridization of the vanadium and TCNE valence orbitals muddle the picture of electron transport via hopping amongst the TCNE  $\pi^* + U_c$  sub-bands. While the carrier activation model adequately describes the charge transport in these materials, and this picture does not change that, an accurate description of the mechanism must take into account these hybridized interactions. In addition, the fully spin-polarized half-semiconductor model also does well to model the magnetoresistance response in  $\text{V}[\text{TCNE}]_{-2}$ , but an adequate description of the ferrimagnetic ordering in  $\text{V}[\text{TCNE}]_{-2}$  is not quite as simple as purely oppositely polarized sub-bands. In short, it would be sufficient to say that while this work answers some very important questions and puts forth some very intriguing evidence regarding the electronic and magnetic structure,  $\text{V}[\text{TCNE}]_{-2}$  is an extraordinarily complex beast that will require even further study to fully elucidate its true nature.

### 6.1.2 Field Effects in V[TCNE]<sub>~2</sub>

For the first time we presented field effects of V[TCNE]<sub>~2</sub>. While a challenging task and displaying only very small changes in current on the order of  $10^{-1} - 10^{-2}$  percent, the results provided some invaluable insight into the charge transport properties of V[TCNE]<sub>~2</sub>. The devices behaved in a manner inconsistent with typical n-channel semiconductor field-effect devices as the current decreases with the application of a gate voltage and also inconsistent with a p-channel device as the current does not change with the application of a gate voltage. The inconsistency is explained on the assumption that V[TCNE]<sub>~2</sub> is an n-channel material, conducts electrons, in that the application of a positive gate voltage injects electrons into the active channel saturating the conduction pathway. This saturation leads to poor conduction and concomitant decrease in current due to filling of the available states for the electrons to hop into. With fewer states available the charge carrier mobility decreases as does the current. The implications of this effect in V[TCNE]<sub>~2</sub> suggest that these devices may be useful as normally open transistors in which a gate voltage is applied to block current flow rather than encourage it. Possibilities include use as amplifiers such as is the case of junction FETs.

### 6.1.3 Outlook and Further Research

One obvious addition to this work is more sophisticated theoretical modeling of the V[TCNE]<sub>~2</sub> system. There are two main aims in this respect: 1) a clearer picture of the hybridization between the vanadium and TCNE and 2) justification of the spin polarization model of mediation of the magnetic interaction between TCNE and vanadium. The experimental evidence of hybridization of V and TCNE lies in an ill defined region of the V XAS spectrum in that there are no specific tell-tale features

directly implying empty antibonding orbitals. Controlled modeling of the interaction between the two moieties can provide supporting evidence to this assignment. While the MCD evidence clearly indicates regions of different polarizations in the TCNE molecule, it fails to answer the why or how this intramolecular polarization comes about. Again, controlled modeling can provide supporting evidence to answer these questions.

Experimentally speaking a prudent next step is to examine the electronic and magnetic structure of other organic-based magnetic materials to develop a more generalized model of these types of systems. Other systems including vanadium tetracyanoquinodimethane ( $\text{V}[\text{TCNQ}]_{\sim 2}$ ), vanadium tetracyanopyrazine ( $\text{V}[\text{TCNP}]_{\sim 2}$ ), and vanadium tetracyanobenzene ( $\text{V}[\text{TCNB}]_{\sim 2}$ ) are ideal candidates for comparing and contrasting the role of the organic species in the electronic and magnetic structure. Substituting other transition metals for vanadium such as manganese produce systems with far lower ordering temperatures and studies similar to those accomplished may elucidate the differences. Finally, mixed metal systems such as  $\text{V}_x\text{Co}_{1-x}[\text{TCNE}]_{\sim 2}$  systems have been shown to increase the coercivity of the system but also reduce the ordering temperature, so a comparison there may also well answer questions as to why.

This work provided a look at the field-effect in  $\text{V}[\text{TCNE}]_{\sim 2}$  with respect to the conductivity, and a similar study can be conducted to examine the effects with respect to the magnetism. Electron paramagnetic resonance (EPR) studies of these field-effect devices can measure the effects on the magnetic properties under the application of an electric field.

Finally, the constant decrease in current in the field-effect devices may have masked certain effects preventing a complete understanding of the mechanisms involved in their

operation and charge transport in  $V[TCNE]_{\sim 2}$  in general. It would be wise to understand this phenomenon, especially if  $V[TCNE]_{\sim 2}$  is to be a viable material for commercial purposes. As mentioned earlier degradation is a big culprit in many of these types of devices and identifying the mechanism of degradation in  $V[TCNE]_{\sim 2}$  is paramount to eliminating or at least severely curtailing it.

**APPENDIX A**  
**V(II) TERM SYMBOLS**

The following details the procedures for determining the term symbols for the various configurations used in the ligand field and charge transfer multiplet calculations for the vanadium centers. Identifying the term symbols is required to determine the symmetries of the allowed transitions. While there are a number of different configurations used in performing the calculations, this appendix only details the procedure for determining the term symbols for the  $3d^3$  configuration; however, the same procedures are used to determine the term symbols for all the configurations used in the calculations. The possible term symbols for pure  $d^n$  configurations can be found in references such as Ref. 89, but the term symbols for mixed configurations such as  $2p^5 3d^n$  must be determined using the procedures outlined here.

In this case of pure  $d^3$  such as is the case for the initial state for  $V^{2+}$  in  $V[TCNE]_{-2}$  there are three electrons that can be arranged in 10 different  $d$  spin orbitals. The total number of ways the three electrons can be arranged in the 10 orbitals is given by

$$\frac{G!}{N!(G-N!)}$$

where  $G$  is the number of spin orbitals (e.g. 10) and  $N$  is the number of electrons (e.g. 3). In this case there are 120 different ways the three electrons can be arranged in the 10 different spin orbitals of the 3d electronic level. To determine these 120 different configurations of the three electrons we must first determine the possible  $m_l$  and  $m_s$  values. In the case of  $d^3$  where  $l = 2$ ,  $m_l$  can take on the values  $-2, -1, 0, 1, 2$  and  $s = 1/2$ .  $m_s$  can take on the values  $+1/2, -1/2$ . Table A.1 lists the 10 possible combinations of these two values along with an assignment number used to keep track of the various combinations of the three electrons.

<u>Assignment</u>	<u><math>m_l</math></u>	<u><math>m_s</math></u>
1	2	1/2
2	1	1/2
3	0	1/2
4	-1	1/2
5	-2	1/2
6	2	-1/2
7	1	-1/2
8	0	-1/2
9	-1	-1/2
10	-2	-1/2

Table A.1. Assignments for the various combinations of  $m_l$  and  $m_s$ . The first column gives an arbitrary assignment number for keeping track of the different  $m_l$  and  $m_s$  only and has no other meaning.

Using the assignment number we can then find the 120 different combinations of the three electrons in the 10 spin orbitals. For example, putting one electron with spin  $\frac{1}{2}$  in the orbital with  $m_l=2$  and one electron with spin  $\frac{1}{2}$  in the orbital with  $m_l=-2$  and one electron with spin  $-\frac{1}{2}$  in the orbital with  $m_l=-2$  gives the three assignment numbers of 1, 5, and 10, respectively, or an overall assignment number of 1510. We then add the  $m_{li}$  and the  $m_{si}$  of the three electrons to obtain  $M_L$  and  $M_S$ , respectively. In the example above we get  $M_L = 2 + (-2) + (-2) = -2$  and  $M_S = \frac{1}{2} + \frac{1}{2} + (-\frac{1}{2}) = \frac{1}{2}$ . Table A.2 lists the 120 different ways to place the three electrons in the 10 spin orbitals by assignment number where  $M_S$  is given as a decimal instead of fraction, i.e.  $1.5 = 3/2$ .



Assn. #	$M_L$	$M_S$	Assn. #	$M_L$	$M_S$	Assn. #	$M_L$	$M_S$	Assn. #	$M_L$	$M_S$
123	3	1.5	234	0	1.5	345	-3	1.5	456	-1	0.5
124	2	1.5	235	-1	1.5	346	1	0.5	457	-2	0.5
125	1	1.5	236	3	0.5	347	0	0.5	458	-3	0.5
126	5	0.5	237	2	0.5	348	-1	0.5	459	-4	0.5
127	4	0.5	238	1	0.5	349	-2	0.5	4510	-5	0.5
128	3	0.5	239	0	0.5	3410	-3	0.5	467	2	-0.5
129	2	0.5	2310	-1	0.5	356	0	0.5	468	1	-0.5
1210	1	0.5	245	-2	1.5	357	-1	0.5	469	0	-0.5
134	1	1.5	246	2	0.5	358	-2	0.5	4610	-1	-0.5
135	0	1.5	247	1	0.5	359	-3	0.5	478	0	-0.5
136	4	0.5	248	0	0.5	3510	-4	0.5	479	-1	-0.5
137	3	0.5	249	-1	0.5	367	3	-0.5	4710	-2	-0.5
138	2	0.5	2410	-2	0.5	368	2	-0.5	489	-2	-0.5
139	1	0.5	256	1	0.5	369	1	-0.5	4810	-3	-0.5
1310	0	0.5	257	0	0.5	3610	0	-0.5	4910	-4	-0.5
145	-1	1.5	258	-1	0.5	378	1	-0.5			
146	3	0.5	259	-2	0.5	379	0	-0.5	567	1	-0.5
147	2	0.5	2510	-3	0.5	3710	-1	-0.5	568	0	-0.5
148	1	0.5	267	4	-0.5	389	-1	-0.5	569	-1	-0.5
149	0	0.5	268	3	-0.5	3810	-2	-0.5	5610	-2	-0.5
1410	-1	0.5	269	2	-0.5	3910	-3	-0.5	578	-1	-0.5
156	2	0.5	2610	1	-0.5				579	-2	-0.5
157	1	0.5	278	2	-0.5	678	3	-1.5	5710	-3	-0.5
158	0	0.5	279	1	-0.5	679	2	-1.5	589	-3	-0.5
159	-1	0.5	2710	0	-0.5	6710	1	-1.5	5810	-4	-0.5
1510	-2	0.5	289	0	-0.5	689	1	-1.5	5910	-5	-0.5
167	5	-0.5	2810	-1	-0.5	6810	0	-1.5			
168	4	-0.5	2910	-2	-0.5	6910	-1	-1.5			
169	3	-0.5									
1610	2	-0.5	8910	-3	-1.5						
178	3	-0.5									
179	2	-0.5	789	0	-1.5						
1710	1	-0.5	7810	-1	-1.5						
189	1	-0.5	7910	-2	-1.5						
1810	0	-0.5									
1910	-1	-0.5									

Table A.2. The 120 different possible combinations for three electrons distributed in 10 spin orbitals.

The next step is to tabulate the different  $M_L-M_S$  combinations and count the number of each pair as shown in Table A.3. For example, there are 8 ways to put the three electrons in the 10 orbitals which yield the same  $M_L = 0, M_S = \frac{1}{2}$  combination.

$M_L-M_S$ Comb.	#	$M_L-M_S$ Comb.	#	$M_L-M_S$ Comb.	#	$M_L-M_S$ Comb.	#
6, -3/2	0	0, 1/2	8	3, -1/2	4	-3, 3/2	1
6, -1/2	0	0, 3/2	2	3, 1/2	4	-4, -3/2	0
6, 1/2	0	-1, -3/2	2	3, 3/2	1	-4, -1/2	2
6, 3/2	0	-1, -1/2	8	2, -3/2	1	-4, 1/2	2
5, -3/2	0	-1, 1/2	8	2, -1/2	6	-4, 3/2	0
5, -1/2	1	-1, 3/2	2	2, 1/2	6	-5, -3/2	0
5, 1/2	1	-2, -3/2	1	2, 3/2	1	-5, -1/2	1
5, 3/2	0	-2, -1/2	6	1, -3/2	2	-5, 1/2	1
4, -3/2	0	-2, 1/2	6	1, -1/2	8	-5, 3/2	0
4, -1/2	2	-2, 3/2	1	1, 1/2	8	-6, -3/2	0
4, 1/2	2	-3, -3/2	1	1, 3/2	2	-6, -1/2	0
4, 3/2	0	-3, -1/2	4	0, -3/2	2	-6, 1/2	0
3, -3/2	1	-3, 1/2	4	0, -1/2	8	-6, 3/2	0

Table A.3. The possible  $M_L - M_S$  combinations possible for the three d electrons. The third column lists the total number of combinations that yield the given  $M_L - M_S$  combination.

It is then convenient to put these  $M_L-M_S$  combination in another table as shown in Table A.4. We can then determine the term symbols for the  $3d^3$  configuration. This is accomplished by looking at Table A.4 to determine the possible values of  $L$  and  $S$ . The largest value of  $M_L$  is 5 with  $M_S = -\frac{1}{2}$  or  $\frac{1}{2}$ , so there must be a state with  $L = 5$  and  $S = \frac{1}{2}$ . The general form of the term symbol is

$$^{2S+1}L_J$$

where  $J = |L - S|, |L - S| + 1, \dots, L + S$  so the possible terms symbols are  ${}^2H_{\frac{1}{2}}$  and  ${}^2H_{\frac{3}{2}}$ . The pairing of  $M_L = 5$  with  $M_S = -\frac{1}{2}$  or  $\frac{1}{2}$  indicates there is one microstate in the columns  $M_S = -\frac{1}{2}$  and  $M_S = \frac{1}{2}$  for each  $M_L$  between  $-5$  and  $5$  for a total of 22 microstates, which agrees with the degeneracy of  $2J+1$  for each  $J$  in LS coupling. If we remove each of these microstates from the table we are left with the largest value of  $M_L = 4$  with  $M_S = -\frac{1}{2}$  or  $\frac{1}{2}$  as shown in Table A.5.

	$M_S = -3/2$	$-1/2$	$1/2$	$3/2$
$M_L = 6$	0	0	0	0
5	0	1	1	0
4	0	2	2	0
3	1	4	4	1
2	1	6	6	1
1	2	8	8	2
0	2	8	8	2
-1	2	8	8	2
-2	1	6	6	1
-3	1	4	4	1
-4	0	2	2	0
-5	0	1	1	0
-6	0	0	0	0

Table A.4. A convenient way to put the results of Table A.3 in order and to keep track of the different combinations of  $M_L$  and  $M_S$  for the purpose of determining the term symbols.

This indicates there must be a state with  $L = 4$  and  $S = \frac{1}{2}$  which yields the terms  ${}^2G_{\frac{1}{2}}$  and  ${}^2G_{\frac{3}{2}}$ . Another 18 states can then be removed from Table A.5 in a similar manner. If we continue on with the same logic until the table is empty we end up with the following terms for the  $3d^3$  configuration

${}^2\text{H}_{11/2}, {}^2\text{H}_{9/2}$
${}^2\text{G}_{9/2}, {}^2\text{G}_{7/2}$
${}^4\text{F}_{9/2}, {}^4\text{F}_{7/2}, {}^4\text{F}_{5/2}, {}^4\text{F}_{3/2}$
${}^2\text{F}_{7/2}, {}^2\text{F}_{5/2}$
${}^2\text{D}_{5/2}, {}^2\text{D}_{3/2}$ (two terms each)
${}^4\text{P}_{5/2}, {}^4\text{P}_{3/2}, {}^4\text{P}_{1/2}$
${}^2\text{P}_{3/2}, {}^2\text{P}_{1/2}$

which, with their respective degeneracies, gives a total of 120 states as we would expect.

	$M_S = -3/2$	$-1/2$	$1/2$	$3/2$
$M_L = 6$	0	0	0	0
5	0	0	0	0
4	0	1	1	0
3	1	3	3	1
2	1	5	5	1
1	2	7	7	2
0	2	7	7	2
-1	2	7	7	2
-2	1	5	5	1
-3	1	3	3	1
-4	0	1	1	0
-5	0	0	0	0
-6	0	0	0	0

Table A.5. Table A.4 after removing the 22 microstates associated with  $M_L = 5$  leaving the largest  $M_L = 4$ .

For the final state  $2p^5 3d^4$  we follow a similar path in finding the terms for each of  $2p^5$  and  $3d^4$ , except to find the terms for  $2p^5 3d^4$  we will need to vector multiply the terms to find the  $L$ 's and the  $S$ 's for the final state terms. The terms for the  $2p^5$  configuration are quite easy in that they are exactly the same as  $2p^1$ . In this case  $L = 1$  and  $S = 1/2$ . So the possible terms are  ${}^2\text{P}_{1/2}$  and  ${}^2\text{P}_{3/2}$  giving us the 6 possible states for 1 (or 5) electrons in 6  $2p$  spin orbitals. The  $3d^4$  configuration requires a little more work, but if the steps are followed for finding the terms for a  $3d^3$  configuration the following terms are obtained

$^1S_0$ (2 terms)
$^1D_2$ (2 terms)
$^5D_0, ^5D_1, ^5D_2, ^5D_3, ^5D_4$
$^3D_1, ^3D_2, ^3D_3$
$^3P_0, ^3P_1, ^3P_2$ (2 terms each)
$^3F_2, ^3F_3, ^3F_4$ (2 terms each)
$^1F_3$
$^1G_4$ (2 terms)
$^3G_3, ^3G_4, ^3G_5$
$^3H_4, ^3H_5, ^3H_6$
$^1I_6$

which yields 210 possible states as we would expect given that  $\frac{10!}{4!(10-4)!} = 210$ . Now

that we know the terms for the  $2p^5$  and the  $3d^4$  configuration individually to figure out the terms for the  $2p^5 3d^4$  configuration we must vector multiply the terms from the individual configurations. This is accomplished by first vector multiplying the  $S$ 's and then the  $L$ 's and then determining the resultant terms symbols. In this case we need not worry about the  $J$  values. The values obtained from vector multiplying the  $S$ 's results in values according to the following

$$|s_1 - s_2| \leq S \leq s_1 + s_2$$

and similarly for vector multiplying the  $L$ 's

$$|l_1 - l_2| \leq L \leq l_1 + l_2$$

For example, multiplying  $^2P \otimes ^3F$  gives  $S = 1/2$  and  $3/2$  and  $L = 2, 3$ , and  $4$  for which we obtain the term symbols  $^2D, ^4D, ^2F, ^4F, ^2G$ , and  $^4G$ . The term symbols with respective  $J$  values obtained for the  $2p^5 3d^4$  configuration are then

$^2S_{1/2}$ (2 terms each)	$^4S_{3/2}$ (2 terms each)	
$^2P_{1/2,3/2}$ (7 terms each)	$^4P_{1/2,3/2,5/2}$ (4 terms each)	$^6P_{3/2,5/2,7/2}$
$^2D_{3/2,5/2}$ (8 terms each)	$^4D_{1/2,3/2,5/2,7/2}$ (6 terms each)	$^6D_{1/2,3/2,5/2,7/2,9/2}$
$^2F_{5/2,7/2}$ (9 terms each)	$^4F_{3/2,5/2,7/2,9/2}$ (5 terms each)	$^6F_{1/2,3/2,5/2,7/2,9/2,11/2}$
$^2G_{7/2,9/2}$ (7 terms each)	$^4G_{5/2,7/2,9/2,11/2}$ (4 terms each)	
$^2H_{9/2,11/2}$ (5 terms each)	$^4H_{7/2,9/2,11/2,13/2}$ (2 terms each)	
$^2I_{11/2,13/2}$ (2 terms each)	$^4I_{9/2,11/2,13/2,15/2}$	
$^2J_{13/2,15/2}$		

It is then these term symbols and their relative energies that are used in calculating the various transitions between the ground and excited states to determine the multiplet structure for x-ray absorption of  $V^{n+}$ .

## BIBLIOGRAPHY

- [1] C. Seife, et al., *Science* **309**, 78 (2005)
- [2] J.M. Manriquez, G.T. Yee, R.S. McLean, A.J. Epstein, and J.S. Miller, *Science* **252**, 1415 (1991)
- [3] S.A. Wolf, D.D. Awschalom, R.A. Buhrman, J.M. Daughton, S. von Molnár, M.L. Roukes, A.Y. Chtchelkanova, D.M. Treger, *Science* **294**, 1488 (2001)
- [4] Data from ISI Web of Knowledge
- [5] F. Ebisawa, T. Kurokawa, S. Nara, *J. Appl. Phys.* **54**, 3255 (1983); K. Kudo, M. Yamashina, T. Moriizumi, *Jpn. J. Appl. Phys.* **23**, 130 (1984), and A. Tsumura, H. Koezuka, T. Ando, *Appl. Phys. Lett.* **49**, 1210 (1986)
- [6] R. Rotzoll, S. Mohapatra, V. Olariu, R. Wenz, M. Grigas, K. Dimmler, O. Shchekin, A. Dodabalapur, *Appl. Phys. Lett.* **88**, 123502 (2006); P.F. Baude, D.A. Ender, M.A. Haase, T.W. Kelley, D.V. Muyres, S.D. Theiss, *Appl. Phys. Lett.*, **82**, 3964 (2003)
- [7] H. Sirringhaus, T. Kawase, R.H. Friend, *MRS Bull.* **26**, 539 (2001); G.H. Gelinck, H.E.A. Huitema, E. van Veenendaal, E. Cantatore, L. Schrijnemakers, J. van der Putten, T.C.T. Geuns, M. Beenhakkers, J.B. Giesbers, B.H. Huisman, E.J. Meijer, E.M. Benito, F.J. Touwslager, A.W. Marsman, B.J.E. van Rens, D.M. de Leeuw, *Nature Mater.* **3**, 106 (2004)
- [8] J.-W. Yoo, R. Shima Edelstein, D.M. Lincoln, N.P. Raju, C. Xia, K.I. Pokhodnya, J.S. Miller, A.J. Epstein, *Phys. Rev. Lett.* **97**, 247205 (2006)
- [9] J.S. Miller and A.J. Epstein, *MRS Bulletin* **25**, 21 (2000)
- [10] G.-Q. Bian, T. Kuroda-Sowa, H. Konaka, M. Hatano, M. Maekawa, M. Munakata, H. Miyasaka, M. Yamashita, *Inorg. Chem.* **43**, 4790 (2004)
- [11] J.S. Miller, A.J. Epstein, *Mat. Res. Soc. Symp. Proc.* **413**, 321 (1996)

- [12] J.S. Miller, A.J. Epstein, *J. Am. Chem. Soc.* **109**, 3850 (1987)
- [13] M. Kinoshita, *Phil. Trans. R. Soc. Lond. A* **357**, 2855 (1999)
- [14] A.J. Epstein and J.S. Miller, *Mol. Cryst. Liq. Cryst.* **233**, 171 (1993)
- [15] K.I. Pokhodnya, A.J. Epstein, and J.S. Miller *Adv. Mater.* **12**, 410 (2000)
- [16] N.P. Raju, T. Savrin, V.N. Prigodin, K.I. Pokhodnya, J.S. Miller, and A.J. Epstein, *J. Appl. Phys.* **93**, 6799 (2003)
- [17] V.N. Prigodin, N.P. Raju, K.I. Pokhodnya, J.S. Miller, and A.J. Epstein, *Adv. Mater.* **14**, 1230 (2002)
- [18] Unpublished data provided by Dr. N.P. Raju.
- [19] J.H. Davies, *J. Phys. C: Solid State Phys.* **17**, 3031 (1984)
- [20] V.N. Prigodin, N.P. Raju, K.I. Pokhodnya, J.S. Miller, A.J. Epstein, *Synth. Met.* **135-136**, 87 (2003)
- [21] F. de Groot, J. Vogel in *Neutron and X-ray Spectroscopy*, F. Hippert, E. Geissler, J.L. Hodeau, E. Lelièvre-Berna, J.-R. Regnard, eds., Springer (2006)
- [22] B.T. Thole, P. Carra, F. Sette, G. van der Laan, *Phys. Rev. Lett.* **68**, 1943 (1992)
- [23] P. Carra, B.T. Thole, M. Altarelli, X. Wang, *Phys. Rev. Lett.* **70**, 694 (1993)
- [24] F. Baudelet in *Neutron and X-ray Spectroscopy*, F. Hippert, E. Geissler, J.L. Hodeau, E. Lelièvre-Berna, J.-R. Regnard, eds., Springer (2006)
- [25] M. Sacchi, J. Vogel in *Magnetism and Synchrotron Radiation*, E. Beaurepaire, F. Scheurer, G. Krill, J.-P. Kappler, eds., Springer (2001)
- [26] J.J. Rehr, A.L. Ankudinov, *J. Elec. Spec. Rel. Phenom.* **114-116**, 1115 (2001); C.R. Natoli, M. Benfatto, S. Della Longa, K. Hatada, *J. Synchrotron Rad.* **10**, 26 (2003); T. Mukoyama, *Spectro. Acta B* **59**, 1107 (2004)
- [27] F. De Groot, *Chem. Rev.* **101**, 1779 (2001)
- [28] F.M.F de Groot, J.C. Fuggle, B.T. Thole, and G.A. Sawatzky, *Phys. Rev. B* **42**, 5459 (1990)



- [29] O. Gunnarsson, K. Schönhammer, *Phys. Rev. B* **28**, 4315 (1983); A. Fujimori, F. Minami, *Phys. Rev. B* **30**, 957 (1984); G.A. Sawatzky, J.W. Allen, *Phys. Rev. Lett.* **53**, 2339 (1984)
- [30] F.M.F de Groot, J.C. Fuggle, B.T. Thole, and G.A. Sawatzky, *Phys. Rev. B* **41**, 928 (1990)
- [31] R. Schroeder, L.A. Majewski, M. Grell, *Appl. Phys. Lett.* **84**, 1004 (2004)
- [32] L. A. Majewski, R. Schroeder, M. Grell *Appl. Phys. Lett.* **85**, 3620 (2004)
- [33] F. Xue, Y. Su, K. Varahramyan, *IEEE Trans. Elect. Dev.* **52**, 1982 (2005)
- [34] K.S. Lee, T.J. Smith, K.C. Dickey, J.E. Yoo, K.J. Stevenson, Y.-L. Loo, *Adv. Func. Mater.* **16**, 2409 (2006)
- [35] S. Uemura, A. Komukai, R. Sakaida, T. Kawai, M. Yoshida, S. Hoshino, T. Kodzasa, T. Kamata, *Synth. Met.* **153**, 405 (2005)
- [36] L. Fu, X. Li, Y. Liu, Z. Liu, L. Cao, D. Wei, Y. Wang, G. Yu, W. Hu, B. Han, *J. Phys. Chem.* **111**, 8098 (2007)
- [37] J. Veres, S. Ogeir, G. Lloyd, D. de Leeuw, *Chem. Mater.* **16**, 4543 (2004)
- [38] J. Zaumseil, H. Sirringhaus, *Chem. Rev.* **107**, 1296 (2007)
- [39] S. Scheinert . G Paasch in *Physics of Organic Semiconductors*, W. Brutting, ed., Wiley-VCH (2005)
- [40] E.J. Meijer, D.M. de Leeuw, S. Setayesh, E. van Veeneedaal, B.-H. Huisman, P.W.M. Blom, J.C. Hummelen, U. Scherf, T.M. Klapwijk, *Nature Mater.* **2**, 678 (2003)
- [41] H. Nishizawa, Y. Majima, *Jpn. J. Appl. Phys.* **45**, L27 (2006)
- [42] L.-L. Chua, J. Zaumseil, J.-F. Chang, E.C.-W. Ou, P.K.-H. Ho, H. Sirringhaus, R.H. Friend, *Nature* **434**, 194 (2005)
- [43] C.R. Newman, C.D. Frisbie, D.A. da Silva Filho, J.-L. Brédas, P.C. Ewbank, K.R. Mann, *Chem. Mater.* **16**, 4436 (2004)
- [44] A. Facchetti, M.-H. Yoon, T.J. Marks, *Adv. Mater.* **17**, 1705 (2005)

- [45] J.S. Miller, *Angew. Chem. Int. Ed.* **45**, 2508 (2006)
- [46] X. Liu, J.E. Ellis, T.D. Miller, P. Ghalasi, J.S. Miller, *Inorg. Synth.* **34**, 96 (2004)
- [47] M.V. Barybin, M.K. Pomije, J.E. Ellis, *Inorg. Chim. Act.* **269**, 58 (1998)
- [48] R. Shima Edelstein, J.-W. Yoo, N. P. Raju, J. D. Bergeson, K. I. Pokhodnya, J. S. Miller, A. J. Epstein *Mater. Res. Soc. Symp. Proc.*, **871E**, I7.3.1 (2005)
- [49] More information about the beamlines and equipment used to collect the XAS spectra at the Advanced Light Source at Lawrence Berkeley National Laboratory can be found at [http://www-als.lbl.gov/als/als\\_users\\_bl/bl\\_table.html](http://www-als.lbl.gov/als/als_users_bl/bl_table.html).
- [50] J. Zaanen, G. Sawatzky, J. Fink, W. Speier, J.C. Fuggle, *Phys. Rev. B* **32**, 4905 (1985)
- [51] D. Haskel, Z. Islam, J. Lang, C. Kmety, G. Srajer, K.I. Pokhodnya, A.J. Epstein, J.S. Miller, et al. *Phys. Rev. B* **70**, 054422 (2004)
- [52] J. Stöhr, *NEXAFS Spectroscopy*. Springer-Verlag, (1992)
- [53] F.M.F. de Groot, *Physica B* **208 & 209**, 15 (1995)
- [54] F. de Groot, *Coord. Chem. Rev.* **249**, 31 (2005)
- [55] M.P. de Jong, C. Tengstedt, A. Kanciurzevska, E. Carlegrim, W.R. Salaneck, M. Fahlman, *Phys. Rev. B* **75**, 064407 (2007)
- [56] F.M.F. de Groot, J. Electron Spectrosc. Relat. Phenom. **67**, 529 (1994)
- [57] R. Garde, F. Villain, M. Verdaguer, *J. Am. Chem. Soc.* **124**, 10531 (2002)
- [58] P. Mahadevan, D.D. Sarma, *Phys. Rev. B* **61**, 7402 (2000)
- [59] Unpublished XPS data collected by Dr. Ruthie Shima Edelstein. These results are very close to those in Pokhodnya, et al. *Adv. Mater.* **12**, 410 (2000) which indicates an 8.77:1 N to V ratio.
- [60] P. Saintavit, D. Cabaret, V. Biois in *Neutron and X-ray Spectroscopy*, F. Hippert, E. Geissler, J.L. Hodeau, E. Lelièvre-Berna, J.-R. Regnard, eds., Springer (2006)

- [61] R. Zimmermann, R. Claessen, F. Reinert, P. Steiner, S. Hüfner, *J. Phys. Condens. Matter* **10**, 5697 (1998)
- [62] O.Y. Khyzhun, T. Strunskus, W. Grünert, C. Wöll, *J. Electr. Spectrosc. Rel. Phenom.* **149**, 45 (2005)
- [63] O. Müller, J.P. Urbach, E. Goering, T. Weber, R. Barth, H. Schuler, M. Klemm, S. Horn, *Phys. Rev. B* **56**, 15056 (1997)
- [64] F. Kubel, W. Lengauer, K. Yvon, K. Knorr, A. Junod, *Phys. Rev. B* **38**, 12908 (1988)
- [65] J.-M. Mariot, C.F. Hague, W. Lengauer, J. Redinger, P. Weinberger, E. Beauprez, *Physica Scripta* **41**, 584 (1990)
- [66] R. Sanjinés, C. Weimer, P. Hones, F. Lévy, *J. Appl. Phys.* **83**, 1396 (1998)
- [67] J.C. Fuggle, M. Campagna, Z. Zolnierok, R. Lässer, A. Platau, *Phys. Rev. Lett.* **45**, 1597 (1980)
- [68] M.-J. Hubin-Franskin, H. Aouni, D. Duflot, F. Motte-Tollet, C. Hannay, L.F. Ferreira, and G. Tourillon, *J. Chem. Phys.* **106**, 35 (1997)
- [69] C. Tengstedt, M. Unge, M.P. de Jong, S. Stafström, W.R. Salaneck, M. Fahlman, *Phys. Rev. B* **69**, 165208 (2004)
- [70] K.N. Houk, L. Munchausen, *J. Am. Chem. Soc.* **98**, 937 (1976)
- [71] I. García-Cuesta, A.M.J. Sánchez de Merás, H. Koch, *J. Chem. Phys.* **118**, 8216 (2003)
- [72] C. I. Oprea, A. Damian, M.A. Gîrțu, *J. Optoelectr. Adv. Mater.* **8**, 191 (2006)
- [73] A. Naves de Brito, S. Svensson, H. Ågren, J. Delhalle, *J. Electro, Spectrosc. Rel. Phenom.* **63**, 239 (1993)
- [74] M. Bässler, R. Fink, C. Buchberger, P. Väterlein, M. Jung, E. Umbach, *Langmuir* **16**, 6674 (2000)
- [75] N. Rana, N.S. Sodhi, C. E. Brion *J. Electr. Spectrosc. Relat. Phenom.* **36**, 187 (1985)

- [76] Y. Zubavichus, M. Zharnikov, A. Schaporenko, M. Grunze, *J. Electr. Spectrosc. Relat. Phenom.* **134**, 25 (2004)
- [77] A. Zheludev, A. Grand, E. Ressouche, J. Schweizer, B.G. Morin, A.J. Epstein, D.A. Dixon, J.S. Miller, *J. Am. Chem. Soc.* **116**, 7243 (1994)
- [78] D.A. Dixon, J.S. Miller, *J. Am. Chem. Soc.* **109**, 3656 (1987)
- [79] C. Tengstedt, M.P. de Jong, A. Kanciurzevska, E. Carlegrim, M. Fahlman, *Phys. Rev. Lett.* **96**, 057209 (2006)
- [80] J.-W. Yoo, R. Shima Edelstein, D.M. Lincoln, N.P. Raju, C.Xia, K.I. Pokhodnya, J.S. Miller, and A.J. Epstein, *Phys. Rev. Lett.* **97**, 247205 (2006)
- [81] A.P. Hitchcock, A.T. Wen, E. Rühl, *Chem. Phys.* **147**, 51 (1990)
- [82] A.T. Wen, E. Rühl, A.P. Hitchcock, *Organometallics* **11**, 2559 (1992)
- [83] J.S. Miller, A.J. Epstein, *Angew. Chem. Int. Ed. Engl.* **33**, 385 (1994)
- [84] C. Kollmar, O. Kahn, *Acc. Chem. Res.* **26**, 259 (1993)
- [85] A. Izuoka, S. Murata, T. Sugawara, H. Iwamura, *J. Am. Chem. Soc.* **107**, 1786 (1985)
- [86] C. Kollmar, O. Kahn, *J. Chem. Phys.* **96**, 2988 (1992)
- [87] J.A. Merlo, C.R. Newman, C.P. Gerlach, T.W. Kelley, D.V. Muyres, S.E. Fritz, M.F. Toney, C. D. Frisbie, *J. Am. Chem. Soc.* **127**, 3997 (2005)
- [88] For typical examples see: T. Yasuda, K. Fujita, H. Nakashima, T. Tsutsui, *Jpn. J. Appl. Phys.* **42**, 6614 (2003) and C.R. Newman, R.J. Chesterfield, M.J. Panzer, C.D. Frisbie, *J. Appl. Phys.* **98**, 084506 (2005)
- [89] F.A. Cotton, *Chemical Applications of Group Theory*. John Wiley & Sons (1990)